SOLID STATE PHYSICS, VOL. 51

Displacement Damage in Irradiated Metals and Semiconductors

R. S. AVERBACK

Department of Materials Science and Engineering, University of Illinois at Urbana–Champaign, Urbana, Illinois

T. DIAZ DE LA RUBIA

Chemistry and Materials Science Directorate, Lawrence Livermore National Laboratory, Livermore, California

I. Introduction

Forty years have now passed since Seitz and Koehler published their seminal article in this series on the displacement of atoms during particle irradiation.[1] At that time little was known with certainty either about the way energetic particles interacted with solids or about the properties of the defects that were created. Research on radiation effects in materials was just beginning, motivated strongly by Wigner's realization that the intense flux of neutrons in reactor cores would have deleterious effects on the properties of the graphite moderators and the uranium fuel.[2] Research in this area was additionally motivated by the opportunity afforded by radiation experiments for fundamental studies on the properties of defects in crystals, as new particle accelerators and nuclear reactors made it possible for the first time to produce point defects in a controllable fashion. Although many of the pressing issues raised by Seitz and Koehler are now resolved, much of the motivation for this research has remained the same. The nuclear industry still faces serious challenges in predicting the behavior of reactor components exposed to prolonged neutron irradiation and the degradation of materials to be used for radioactive waste containment. The rapid growth in the use of ion implantation and ion beam processing of materials in the semiconductor industry, moreover, has added additional technological impetus to this research. At the same time particle irradiation continues to be a powerful means for investigating the fundamental aspects of defects in solids. In addition to using irradiation for studies of point defects, although now in more complex materials, heavy ion irradiations are being employed as a controllable method to drive systems far from equilibrium, making possible fundamental studies on the formation and properties of metastable materials. It is these newer perspectives that this current article addresses. Unlike the Seitz and Koehler article, which emphasized the displacements of single atoms, the current article focuses on displacement processes in energetic cascades. Of interest here are the fundamental mechanisms of producing atomic rearrangements and point defects in cascades, the configurations of defects in their primary state of damage, and the fates of these defects as they migrate away from their nascent locations.

1. Primary Interactions Between Energetic Particles and Solids

When energetic particles penetrate solids, they lose their energy through a series of elastic two-body nuclear collisions with target atoms and through

[1] F. Seitz and J. S. Koehler, *Solid State Physics*, Vol. 2, ed. F. Seitz and D. Turnbull, Academic Press, New York (1956), p. 307.
[2] F. Seitz, *Phys. Today* **5**, 6 (1952).

excitation of the electronic system. It is the elastic collisions that are of primary interest for damage creation in metals and most semiconductors, since they lead to the production of Frenkel pairs, which are vacancies and self-interstitial atoms, and to rearrangements of atoms on their lattice sites. Electronic excitations, on the other hand, have rather little direct effect on damage production in these materials. Mostly, the electrons act as a viscous medium through which the atoms pass and thus are important only as a source of energy dissipation. In other situations, the electronic system can play a more fundamental role in the displacement process, as is well documented for alkali halides, ionic glasses, and polymers.[3] New research on the effects of GeV particle and cluster irradiation, moreover, shows damage creation by electronic excitation in all classes of materials.[4]

The atomic displacement process begins with the creation of a primary knock on atom (PKA), which is any target atom struck by the irradiation particle. The terminology PKA derives from considerations of neutron bombardment, where the PKA is created either in an elastic collision with a neutron or in a nuclear reaction. For ion irradiation, either the incident ion, itself, or the target atoms it hits can be considered the PKA, as will be clarified later. Many PKAs recoil with energies far in excess of lattice bonding energies, and these leave their lattice sites and often displace additional atoms in secondary recoil events. Higher-order generations of recoils are produced similarly, resulting in a cascade of collision events. Since the cross sections for atomic collisions increase rapidly with decreasing energy, the distances between successive collisions become progressively shorter. For recoil energies below a few hundreds of electron volts, the mean free paths between collisions causing displacements are reduced to a few atomic distances. As a consequence, localized regions of lattice become highly disturbed, containing high concentrations of defects and large excesses of energy. Shortly after the creation of a PKA, less than ≈ 0.2 ps, the energies of the recoil atoms fall below the threshold energy for additional displacement events, signaling the end of the ballistic phase of the cascade. All atoms in the cascade at this time, however, have been set into motion, creating the conditions of a local thermal spike. The spike persists for only some additional picoseconds before the heat dissipates to the surrounding lattice, but during this time additional atomic rearrangements can take place by thermally activated motion and even plastic deformation. At the end of the event, the remnants of the cascade, termed the *primary state of damage*, are characterized by large supersaturations of Frenkel pairs, dis-

[3] F.W. Clinard and L. W. Hobbs, in *Physics of Radiation Effects in Crystals*, ed. R. A. Johnson and A. N. Orlov, Elsevier, Amsterdam (1986), p. 386.

[4] See, e.g., *MRS Bull.* **20**, (1995).

location loops, redistribution of stresses, and extensive mixing of atoms on lattice sites.

Much of the picture of the atomic displacement process in solids just outlined was realized at the time of the Seitz–Koehler article in 1956. What has evolved since has been the fleshing out of the details of these processes so that realistic predictions of materials response to irradiation can be made available to design engineers. For later comparison with what is now known, two views of displacement processes in energetic cascades around the mid-1950s are presented in Figs. 1 and 2. The first is due to Brinkman (1954), who estimated that the mean free path between displacement events was on the order of one atomic distance. As a consequence, he pictured the damage state as a local depleted zone surrounded by a mantle of interstitial atoms.[5] The second derives from Seeger (1958), who imagined a large number of processes as depicted in the figure.[6] Evidence for many of them is presented in this article. The primary focus of the current article, therefore, is to present our current picture of energetic displacement cascades. The discussion is limited, however, to simple metals and semiconductors. The far greater understanding of displacement processes in metals, moreover, will be reflected in the unbalanced treatment of these two types of materials. Only a small attempt is made to illustrate the significance of this work for current problems of radiation effects, owing to their diverse

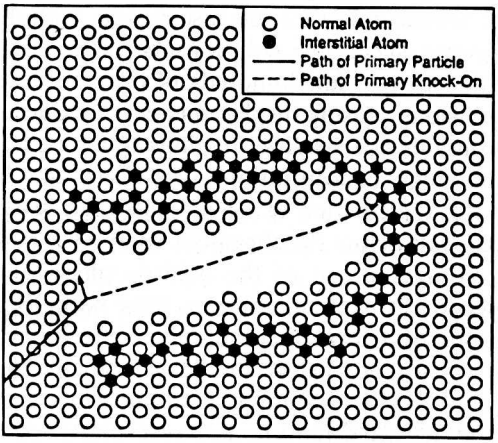

FIG. 1. Schematic illustration of an energetic displacement cascade as envisioned by J. A. Brinkman in 1954. (After Ref. 5.)

[5] J. A. Brinkman, *J. Appl. Phys.* **25**, 961 (1954); *Am. J. Phys.* **24**, 246 (1956).

[6] A. Seeger, *Proc. 2nd UN Int. Conf. on Peaceful Uses of Atomic Energy*, Geneva, (1958), Vol. 6, United Nations, New York, p. 20.

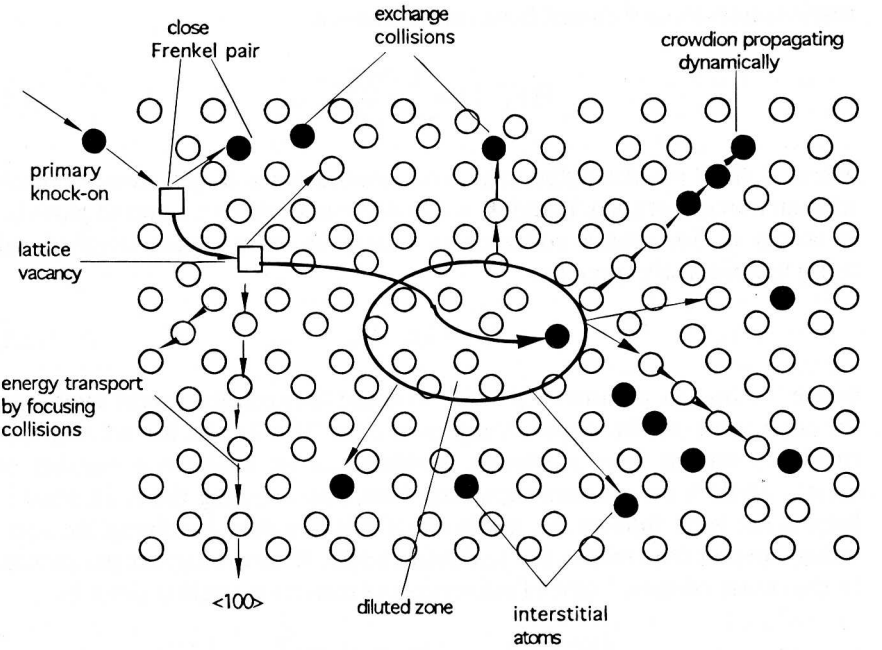

FIG. 2. Atomic displacement processes in energetic displacement cascade envisioned by A. Seeger in 1958. (After Ref. 6.)

nature. In the first sections we briefly review the theory of atomic collisions and the stopping of ions in solids, needed for later discussions. Two tracks are then followed: one examining the progress that has been achieved by experimental means, and the other through computer simulations. Where possible the two methods are compared, but unfortunately, these instances are rare. One point should be made from the outset—that although much is now known about the fundamental aspects of displacement processes in solids, several questions remain, and experimental facts sometimes seem to challenge accepted beliefs. At present we can only remark on these situations.

2. BACKGROUND INFORMATION

a. *Primary Recoil Spectrum*

The primary state of damage produced in a material is markedly different during irradiations with electrons, light or heavy ions, or neutrons, simply because these different particles create PKAs with widely different energies. The distribution of recoil energies for a specific irradiation, or the primary

recoil spectrum, is obtained from the expression

$$P(E_1, T) = \frac{1}{\sigma} \frac{d\sigma(E, T)}{dT}, \tag{2.1}$$

where $d\sigma(E, T)$ is the differential cross section for a target atom to recoil with an energy between T and $T + dT$ when exposed to a beam of particles of energy E. For atomic collisions in solids, the cross section is calculated using the classical expression

$$d\sigma = 2\pi p \, dp, \tag{2.2}$$

where the impact parameter p is the distance between the target atom and the asymptote of the approaching projectile. The details for solving this two-body central force scattering problem can be found in a number of texts[7] and does not warrant repetition here, but outlining the main steps is helpful for what follows. At the heart of this problem is solving the scattering integral that relates the scattering angle, θ, to the impact parameter. In the center-of-mass frame of reference, the scattering angle is given by

$$\theta = \pi - 2 \int_0^{1/\rho} \left\{ \frac{1}{p^2} \left[1 - \frac{V(u)}{E_1} \frac{m_1 + m_2}{m_2} \right] - u^2 \right\}^{-1/2} du \tag{2.3}$$

where $V(u)$ is the interatomic potential, $u = 1/r$, and r is the distance separating the collision partners. E_1 is the initial projectile energy in the laboratory frame of reference, and ρ is the value of r at the distance of closest approach. It is given by

$$\frac{V(\rho)}{1 - p^2/\rho^2} = \frac{m_2 E_1}{m_1 + m_2} = E_{cm}, \tag{2.4}$$

where E_{cm} is the kinetic energy in the center-of-mass system. By solving Eq. (2.3), using the appropriate interatomic potential, the impact parameter can be expressed in terms of the scattering angle,

$$p = p(\theta, E_1). \tag{2.5}$$

Equation (2.5) provides the basis for calculating the trajectories of energetic particles as they penetrate targets. Accordingly, much effort has gone

[7] J. F. Ziegler, J. P. Biersack, and U. Littmark, *The Stopping and Range of Ions in Matter*, Pergamon Press, New York (1985).

into both developing potentials for this purpose that are accurate yet tractable, and finding shortcuts for solving the scattering integral in Eq. (2.3). For calculations of primary recoil spectra and defect production, the relationship between scattering angle and recoil energy is also required. It is obtained through the conservation laws for energy and momentum and is given by

$$T = \frac{4m_1m_2}{(m_1 + m_2)^2} E_1 \sin^2 \frac{\theta}{2} = T_{\max} \sin^2 \frac{\theta}{2}, \tag{2.6}$$

where $T_{\max}$ is the maximum possible recoil energy. What remains is to solve the scattering integral in Eq. (2.3) under the appropriate two-body force model.

Before examining solutions to the scattering integral, it should be noted that an immediate consequence of Eq. (2.6) is that the maximum energy transfer for irradiations with small masses, $m_1 \ll m_2$, is simply $4(m_1/m_2)E_1$, so that light particles transfer only a small fraction of their energy to heavy target atoms. For electrons, energies greater than some hundreds of keV are required to displace a single target atom from its lattice site (a relativistic correction is required for electrons, $T_{\max} = 2m_e/m_2(E_1/m_ec^2 + 2)E_1$). A practical consequence of this concerns damage production in transmission electron microscopes (TEM), which now operate in the energy regime where displacements just become possible. In Al, the critical energy for displacements is $\approx$250 keV, whereas for Au it is $\approx$2.0 MeV. This same principle explains why MeV electrons are employed to produce isolated Frenkel pairs for studies of point defects in solids. Complete tables for threshold electron energies required to displace atoms, and electron-atom cross sections, can be found in the literature.[8] For the same reasons, maximum recoil energies in materials subjected to a neutron flux will be much lower than the neutron energy. For a fission spectrum, the average neutron energy is $\approx$1.0 MeV, which means that the highest recoil energies in a structural material such as Fe are $\approx$60 keV.

For irradiations with charged particles, the interatomic potential in Eq. (2.3) can be expressed in the form

$$V(r) = \frac{Z_1Z_2e^2}{r} \chi(r/a) \tag{2.7}$$

[8] J. W. Corbett, in *Solid State Physics*, ed. F. Seitz and D. Turnbull, Suppl. 7, Academic Press, New York (1966).

where $\chi(r/a)$ is a screening function and a is the screening length. The scattering integral, however, must be solved numerically for any realistic screening functions. It is therefore instructive first to consider the primary recoil spectra for particles interacting through either Coulomb or hard-sphere potentials, as they represent limiting forms of $V(r)$ and can be solved exactly.

The Coulomb potential is given by

$$V(r) = \frac{Z_1 Z_2 e^2}{r}. \tag{2.8}$$

for which Eq. (2.3) has the closed-form solution

$$p = \frac{m_1 + m_2}{2m_2 E_1} Z_1 Z_2 e^2 \cot \frac{\theta}{2}, \tag{2.9}$$

or, using Eq. (2.6)

$$d\sigma = \frac{\pi m_1 Z_1^2 Z_2^2 e^4}{m_2 E_1} \frac{dT}{T^2}. \tag{2.10}$$

Equation (2.10) thus provides the primary recoil spectrum for Coulomb scattering. Of particular note in Eq. (2.10) is the strong $1/T^2$ weighting of recoils toward low energies. The average recoil energy therefore increases only logarithmically with projectile energy, that is,

$$\langle T \rangle = T_{\min} \ln \frac{T_{\max}}{T_{\min}}, \tag{2.11}$$

where $T_{\min}$ is the threshold energy for creating displacements, ≈ 20 eV. For 1-MeV proton irradiation of a metal such as Cu, $\langle T \rangle \approx 200$ eV.

At the opposite extreme is the hard-sphere potential, which is characterized by a step function in the interaction energy when the particles reach their point of closest approach. The impact parameter is simply related to the scattering angle and the hard-sphere radius, ρ_0, by the expression

$$p = \rho_0 \cos \frac{\theta}{2}, \tag{2.12}$$

so that

$$d\sigma = \pi \rho_0^2 \sin \frac{\theta}{2} \cos \frac{\theta}{2} d\theta. \tag{2.13a}$$

Again, using Eq. (2.6), we obtain

$$d\sigma = \pi\rho_0^2 \frac{dT}{T_{max}}. \tag{2.13b}$$

In contrast to Coulomb scattering, the primary recoil spectrum for the hard-sphere interaction is independent of recoil energy, making recoils of all energies up to T_{max} equally probable. The average recoil energy, therefore, is $T_{max}/2$. For 1-MeV neutron irradiation of Cu, $\langle T \rangle = 30$ keV, which is far different from the example of 1-MeV proton irradiation, even though the maximum recoil energies are the same. It should be realized that the hard-sphere radius is Eq. (2.12) does not refer to the atomic radius of an atom in the solid. For ion irradiation, ρ_0 is usually defined for any interaction potential by the distance of closest approach when $p = 0$. For the screened Coulomb interaction, ρ_0 increases with the atomic numbers of the projectile and target and decreases with projectile energy.

For more realistic interatomic potentials, numerical methods must be used to solve Eq. (2.3). Lindhard has shown, however, that in many cases the "magic formula"

$$\frac{\theta^2}{4} = -\frac{3}{16E_r^2} p \frac{d}{dp}[V^2(p)p^{2/3}] \tag{2.14}$$

provides a satisfactory approximation to the scattering integral. For Thomas–Fermi screening, Lindhard *et al.* employed Eq. (2.14) to obtain the relation[9]

$$\frac{d\sigma}{dt} = -\frac{\pi a^2}{2} \frac{f(t^{1/2})}{t^{3/2}}, \tag{2.15}$$

where

$$t = \varepsilon^2 \frac{T}{T_m}, \tag{2.15a}$$

$$\varepsilon = \frac{a_L E_{cm}}{Z_1 Z_2 e^2} \tag{2.15b}$$

$$a_L = \frac{0.8853 a_0}{(Z_1^{2/3} + Z_2^{2/3})^{1/2}}, \tag{2.15c}$$

and a_0 is the Bohr radius ($= 0.0529$ nm).

[9] J. Lindhard, V. Nielsen, and M. Scarff, *Mat. Fys. Medd. Dan. Vid Selsk*, **36**(10), (1968).

The scattering function, $f(t^{1/2})$ is a universal function, with the three-fold set of collision parameters in the cross section combined into the single parameter, t.† Primary recoil spectra calculated using Eq. (2.15) are shown in Fig. 3 for 1-MeV ion bombardments of Ni. Total cross sections for producing recoils with energies greater than the displacement energy (≈ 25 eV) are listed in the inset. The weighting of recoils towards low energies observed in the figure is characteristic of charged particle irradiation. As shown in the inset, total cross sections vary by four orders of magnitude between 1-MeV Xe and 1-MeV protons. The mean free path $\lambda (= 1/N_0 \sigma$, where N_0 is the atomic density) between collisions greater than 25 eV for the Xe projectiles is on the order of the lattice spacing, whereas for protons it is ≈ 2 μm; hence Xe travels through materials leaving behind dense trails of defects, while protons create a sparse distribution of them.

More accurate interatomic potentials based on quantum mechanical ab initio methods like density functional theory[10] are also available, although these methods are computationally too intensive for practical application in statistical models or computer simulations. They are valuable, however, for

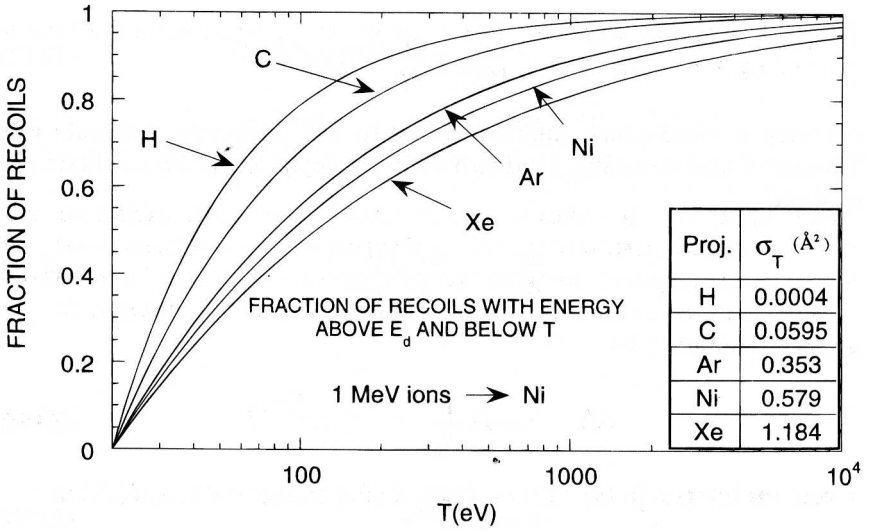

FIG. 3. Integral primary recoil spectra, $P(E, T)$, for ion irradiation of Ni with various 1-MeV ions. The inset lists the total cross sections for recoils with $T > 25$ eV.

† The function $f(t^{1/2})$ can be found in Ref. [7].

[10] See, e.g., R. O. Jones, and O. Gunnarsson, *Rev. Mod. Phys.* **61**, 689 (1989).

setting calibration points for constructing empirical potentials. In this manner, Ziegler *et al.* have compiled the results of calculations based on the local density approximation (LDA) for many ion–target combinations and cast the results into a universal form, which they refer to as the *universal potential.* This widely employed pair potential is given by,[7]

$$\phi(x) = 0.1818\, e^{-3.2x} + 0.5099\, e^{-0.9423x} + 0.2802\, e^{-0.4029x} + 0.02817\, e^{-0.2016x} \tag{2.16}$$

where $x = r/a_U$ and the universal screening length is given by

$$a_U = \frac{0.8854 a_0}{Z_1^{0.23} + Z_2^{0.23}}. \tag{2.16a}$$

The standard deviation of the fit of the universal Ziegler *et al.* repulsive potential to LDA potentials for all ion–target combinations is 18% for energies over 2 eV.[7]

b. *Stopping Powers*

Energy loss of a moving particle in a target can be expressed in the form of a stopping power, dE/dx:

$$\frac{dE}{dx} = \left(\frac{dE}{dx}\right)_n + \left(\frac{dE}{dx}\right)_{el} + \left(\frac{dE}{dx}\right)_Q, \tag{2.17}$$

where n, el, and Q indicate nuclear (elastic), electronic excitation, and nuclear reaction, respectively. Losses through nuclear reactions occur only at very high projectile energies, typically >1 MeV/amu, and are not discussed here. The nuclear energy loss of an ion traveling a distance Δx in a sample is obtained by

$$\Delta E = N_0\, \Delta x \int_{T_{\min}}^{T_m} T \frac{d\sigma(E, T)}{dT}\, dT, \tag{2.18}$$

where the integral in Eq. (2.18) is the stopping cross section, $S_n(E)$. Thus

$$S_n(E) = -\frac{1}{N_0}\frac{dE}{dx}. \tag{2.19}$$

The stopping power can be formulated as a universal function,

$$s_n(\varepsilon) = \frac{d\varepsilon}{d\rho} = \frac{1}{\varepsilon}\int_0^{\varepsilon} f(t^{1/2})\, dt^{1/2}, \tag{2.20}$$

where $S_n(\varepsilon)$ is the reduced stopping power; ε, which was defined in Eq. (2.14b), is the reduced energy; and ρ is the reduced length,

$$\rho = LN_0 4\pi a_L^2 \frac{m_1 m_2}{(m_1 + m_2)^2}, \tag{2.21}$$

where L is a measure of length in the laboratory frame. The stopping cross section is given in practical units by

$$S_n(E) = \frac{\pi a_L^2 T_m}{\varepsilon} s_n(\varepsilon). \tag{2.22}$$

The stopping power is plotted in Fig. 4 in reduced units.

The electronic stopping power has different forms at high and low energies. At high energies, Bethe[11]–Bloche[12] theory is applicable (but see Ref. 7 for details), whereas at low energies, models of Firsov[13] and Lindhard and Scharff[14] become appropriate. For most problems concerning displacement processes, the stopping in the low-energy regime is of primary interest, for

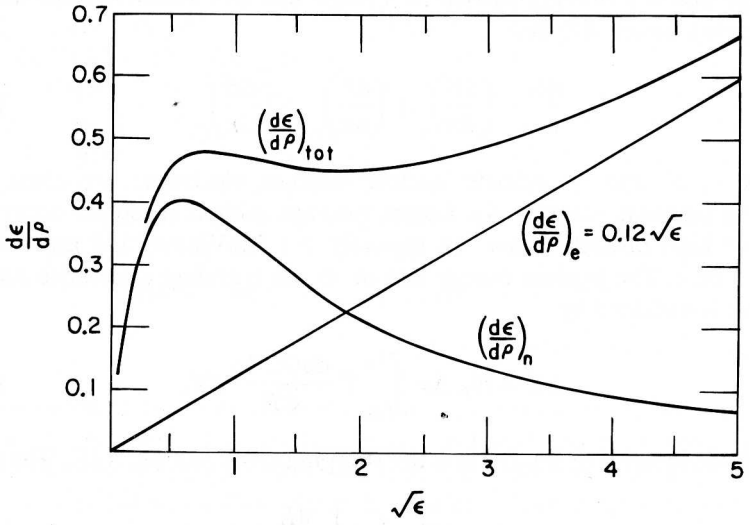

FIG. 4. Nuclear and electronic stopping powers of ions in solids in reduced units.

[11] H. A. Bethe, *Ann. Phys.* **5**, 325 (1930).
[12] F. Bloch, *Ann. Phys.* **16**, 287 (1933).
[13] O. B. Firsov, *Sov. Phys. JETP* **36**, 1076 (1959).
[14] J. Lindhard and M. Scharff, unpublished report.

TABLE 1. CHARACTERISTIC ENERGY, E_c(keV) CORRESPONDING TO $\varepsilon = 1$

PROJECTILE	SILICON	GERMANIUM	TIN	GOLD
B	8.9	20	33	61.4
P	47	85	130	209
As	210	300	400	570
Sb	520	655	820	1140
Bi	1510	1700	1950	2560

which the Lindhard–Scharff theory yields

$$s_e(\varepsilon) = k_L \varepsilon^{1/2}, \tag{2.23}$$

where

$$k_L = \frac{32}{3\pi}\left(\frac{m_e}{m_2}\right)^{1/2} \frac{(1 + m_2/m_1)^{3/2} Z_1^{2/3} Z_2^{2/3}}{(Z_1^{2/3} + Z_2^{2/3})^{3/4}}. \tag{2.24}$$

Equation (2.23) is accurate to $\approx \pm 30\%$ for high enough energies that the band structure is unimportant.[15] Unlike the nuclear stopping power, $s_e(\varepsilon)$ is not a universal function, although the value of k_L does not vary greatly for most ion–target combinations. The electronic stopping is shown in Fig. 4 along with the nuclear stopping power. For convenience in using these plots, which are in reduced units, the projectile energy, E_C, at which $\varepsilon = 1$ is tabulated in Table 1 for a few ion–solid combinations. Since E_1 varies linearly with ε, values of E_1 for other ε are immediately available.

II. Binary Collision and Thermal Spike Models

3. BINARY COLLISION APPROXIMATION

The fundamental assumptions in the binary collision approximation (BCA) are that particles move along straight trajectories between two-body (binary) collisions, and that the fraction of moving atoms is sufficiently small that moving particles collide primarily with particles at rest. The latter condition corresponds to linearization of the Boltzmann transport equation, thus evoking the name '*linear cascades*' for such situations. Both assumptions are reasonably justified while the particles have energies greater than the threshold energy for atomic displacements.

[15] H. E. Schiott, *Radiat. Eff.* **6**, 107 (1970).

a. *Damage Energy*

Calculations of atomic displacements in the BCA rely on the assumption that recoil events are not influenced by the detailed manner in which energy is lost to the electronic system during collisions. This makes useful defining a damage energy E_D given by

$$E_D = E_1 - Q, \tag{3.1}$$

where Q represents the loss of energy to electronic excitation. From the theory of Lindhard, Scharff and Schiott (LSS theory),[16] the damage energy can be obtained from the expression[17]

$$E_D = \frac{E_1}{1 + k_L g(\varepsilon)}, \tag{3.2}$$

where to good approximation,[18]

$$g(\varepsilon) = \varepsilon + 0.40244\varepsilon^{3/4} + 3.4008\varepsilon^{1/6}. \tag{3.3}$$

Figure 5 shows the fractional damage energy for self-ion bombardment of a few targets as a function of ion energy. Even at very low projectile energies, $\approx 20\%$ of the energy is lost to electronic excitation.

b. *Kinchin–Pease Expression*

Kinchin and Pease (KP) calculated by transport theory, using the BCA, that the number of defects produced by a PKA of energy T is given by, $\nu(T) = T/2E_d$, where E_d is the threshold energy for an atom to recoil from its lattice site and create a stable Frenkel pair.[19] For recoils with energies less than E_d, the recoil atom will return to its lattice site (see Section III). The KP expression thus indicates that half of the cascade energy goes into displacements and the other half is dissipated in nonproductive subthreshold recoils. Calculations of defect production using transport theory is adequately described elsewhere[7,20] and thus is not covered here. Moreover, this theory is presently little used for defect calculations, owing to its difficulty in treating alloys and inhomogeneous targets and to the availability of

[16] J. Lindhard, M. Scharff, and H. E. Schiott, *Mater. Fys. Med. Dan. Vid Selsk* **33**, 14 (1963).
[17] J. Lindhard, M. Scharff, and P. V. Thomsen, *Mater. Fys. Med. Dan. Vid Selsk* **33**, 10 (1963).
[18] M. T. Robinson, in *Nuclear Fusion Reactors*, ed. J. L. Hall and J. H. C. Maples, (British Nuclear Engineering Society, London (1970), p. 364.
[19] G. H. Pease and R. S. Pease, *Rep. Prog. Phys.* **18**, 1 (1955).
[20] P. Sigmund, *Radiat. Eff.* **1**, 15 (1969); *Appl. Phys. Lett.* **14**, 114 (1969).

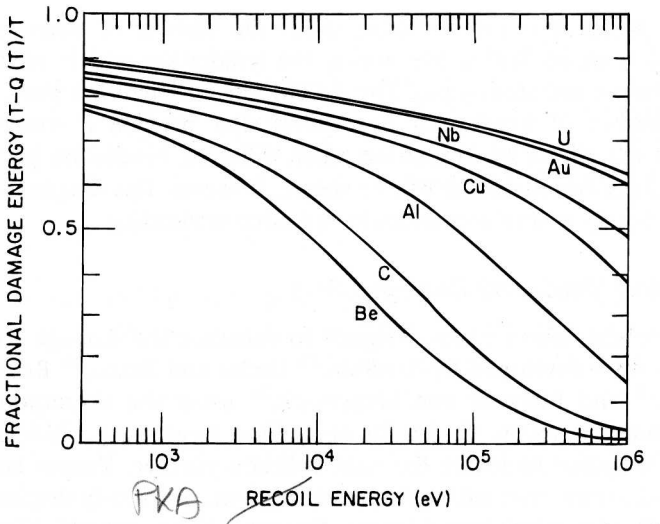

FIG. 5. Fractional damage energy plotted as a function projectile energy for self-ion bombardment of a number of targets. (After Ref. 18.)

accurate, yet efficient computer simulation codes. When realistic interatomic potentials and electronic excitation are included in the calculation, the Kinchin–Pease expression obtains the modified form[20,21]

$$\nu(T) = \begin{cases} 0 & T < E_d \quad (3.4a) \\ 1 & E_d < T < 2.5E_d \quad (3.4b) \\ \dfrac{0.8E_D}{2E_d} & T > 2.5E_d. \quad (3.4c) \end{cases}$$

Defect production for any ion–target combination can thus be calculated using the expression

$$\nu(E_1) = \int_{E_1}^{E_d} \frac{dE}{S_n + S_e} \int_{E_d}^{T_{max}} dT \, \frac{d\sigma(E, T)}{dT} \, \nu(T). \quad (3.5)$$

The inner integral is the Frenkel pair cross section for a projectile of energy E, $\sigma_{FP}(E)$, and the outer integral sums over the various encounters an ion undergoes with target atoms as it slows down and stops. The product

[21] M. J. Norgett, M. T. Robinson, and I. M. Torrens, *Nucl. Eng. Des.* **33**, 50 (1975).

$\sigma_{FP}(E)\Phi$, where Φ is the ion dose, yields the number of times an atom is displaced from its lattice site during the irradiation and is referred to as displacements per atom (dpa). The ASTM has adopted dpa units as a standard measure of irradiation dose since dpa provide a simple way to compare the effects of irradiation when different irradiation particles and materials are employed. As will be shown, however, this simple scaling with damage energy is very approximate and often misleading.

c. *Computer Simulations Employing BCA*

Computer simulation codes designed to calculate the damage structure in cascades were developed by Yoshida,[22] Beeler and Besco,[23] Robinson and Torrens,[24] and Biersack and Haggmark,[25] using the assumptions of the BCA discussed above. Codes for crystalline targets (e.g., MARLOWE[24]) search the lattice to locate the next collision partner. Vacant lattice sites, interstitial atoms, and lattice strain arising from previously displaced atoms are usually not taken into account. For amorphous targets, Monte Carlo procedures are employed for locating successive collision partners (e.g., TRIM[25]). When the recoil energy of a struck target atom exceeds the displacement energy, E_d, that atom joins the distribution of moving particles with an energy $T - E_b$, where E_b is the lattice binding energy; otherwise, this atom is dropped from further consideration. All atoms remain in the cascade of moving atoms until their energy falls below some cutoff energy, E_{cut}. If after the two-body collision the energy of the original projectile falls below E_{cut} and $T > E_d$, the projectile replaces the target atom on its lattice site. If, on the other hand, $T < E_d$ and the projectile energy $< E_{cut}$, the projectile becomes an interstitial atom. The number and locations of interstitial atoms, vacancies, and replaced atoms are thereby obtained.

A primary result of the BCA simulations is their corroboration of the modified Kinchin–Pease expression. This finding may seem obvious at first glance since the underlying assumptions in the transport theory and the simulations are the same. The simulations, however, retain the locations of vacancy and interstitial defects in the cascade volume, which makes possible testing whether a vacancy (interstitial) created in one collision event can recombine with another interstitial (vacancy) produced in the same cascade. The observation that little recombination of this type occurs in cascades is illustrated in Fig. 6, where the average damage energy per Frenkel pair is

[22] M. Yoshida, *J. Phys. Soc. Jpn.* **16**, 44 (1961).
[23] J. R. Beeler, and D. G. Besco, *J. Appl. Phys.* **34**, 2873 (1963).
[24] M. T. Robinson, and I. M. Torrens, *Phys. Rev.* **9**, 5008 (1974).
[25] J. P. Biersack, and L. G. Haggmark, *Nucl. Instrum. Methods* **174**, 257 (1980).

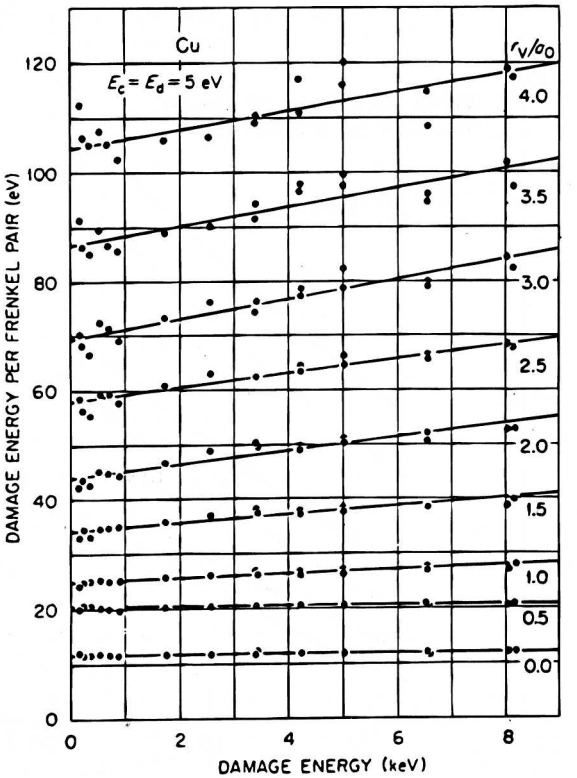

FIG. 6. Average damage energy required to create a Frenkel pair in Cu, plotted as a function of PKA energy using different vacancy capture radii, r_v. The calculation was performed using MARLOWE. (After Ref. 24.)

plotted as a function of energy. Results assuming different capture radii for recombination are shown. Even with a capture radius of $4.0a_0$ (a_0 is defined here as the lattice parameter), the deviation from the modified Kinchin–Pease expression is only $\approx 10\%$ for cascade energies up to 8 keV. A reaction radius of $\approx 1.5a_0$, however, is more reasonable (see Section III), for which the effect is even smaller. Figure 6 shows that the energy required to produce a Frenkel pair increases with increasing capture radius at all energies, but this arises from recombination of the interstitial with its own vacancy.

d. *Cascade Structure: Subcascades*

For projectiles with energies greater than several tens of keV, the mean free path between energetic collisions is long. This is shown in Fig. 7, where the mean free paths between collisions of energy greater than T, $\ell(T)$, are

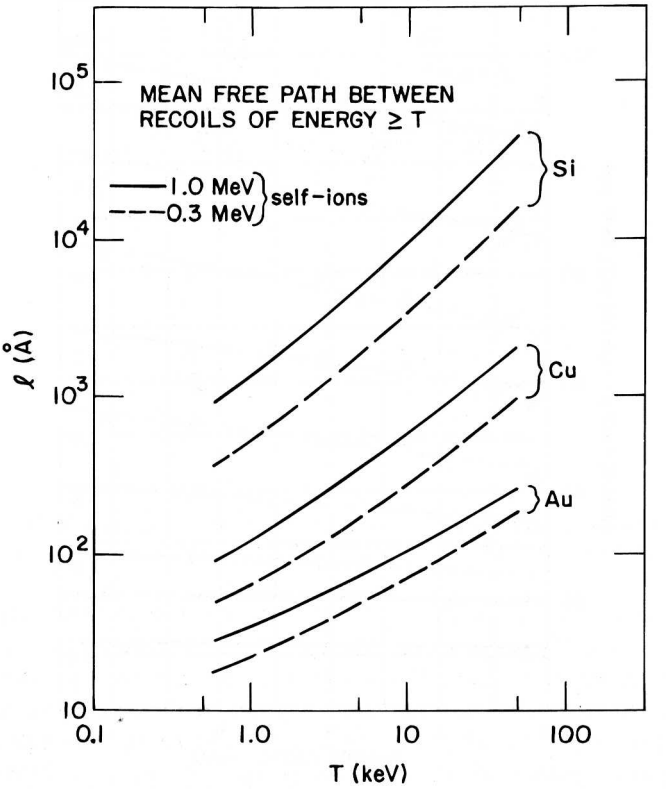

FIG. 7. Mean free paths between collisions with energy transfers greater than T for self-ion bombardment.

plotted for a few representative cases as a function of T. The value of ℓ were calculated using the expression

$$\ell(T) = \left[N_0 \int_T^{T_{\max}} \frac{d\sigma(E, T)}{dT} \right]^{-1}. \tag{3.6}$$

Since most secondary recoils have energies much less than the PKA, which is a consequence of the screened Coulomb interaction, they will undergo subsequent collisions close to their recoil site. The structure of the cascade, therefore, will consist of a string of localized regions containing high defect densities, separated by regions of relatively few defects. This description of subcascade formation is illustrated by the BCA computer simulation shown in Fig. 8, where the locations of point defects produced by a 200-keV recoil in Cu are plotted. Although defects are produced everywhere along the

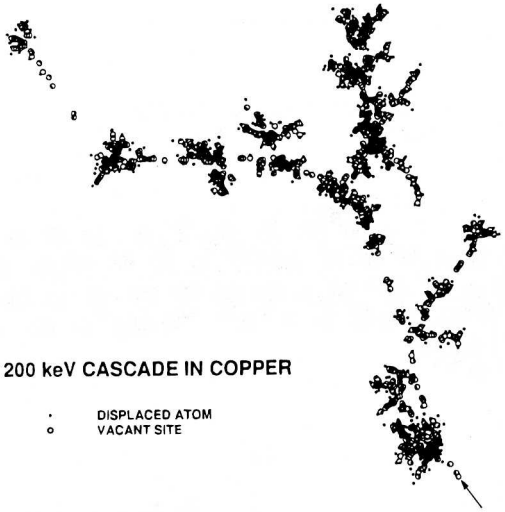

FIG. 8. Locations of point defects created during the stopping of a 200-keV Cu projectile in Cu, as calculated using MARLOWE. (Courtesy of H. Heinisch.[26])

track of the projectile, local pockets with high defect densities are clearly visible.[26] As the PKA energy is reduced, the spacing between major collisions is observed to decrease. Below a critical projectile energy, the average cascade is no longer disconnected, but owing to the stochastic nature of recoil events, large fluctuations in the defect density within a single cascade, and from one cascade to another, will persist. The crystal structure also plays an important role in subcascade formation, particularly at lower energies. It is seen in Fig. 9a that a 5-keV projectile in Ni scatters into a close-packed direction and is then steered by atomic rows of atoms through a crystal channel. The particle then travels over long distances before undergoing another energetic collision.[27] The effect of this channeling behavior on subcascade formation is illustrated in Fig. 9b for a 20-keV cascade in Ni_3Al.

e. *Weighted-Average Recoil Spectrum*

One limit for describing energy deposition in a solid considers each primary recoil as an individual subcascade. This assumption is always valid for neutrons and light ions, for which the mean free path between energetic collisions is much longer than the recoil distance of the PKA. For ion

[26] H. Heinisch, *JOM*, **48** (1996) 38.
[27] N. V. Doan, CEA-Saclay SRMP (1996).

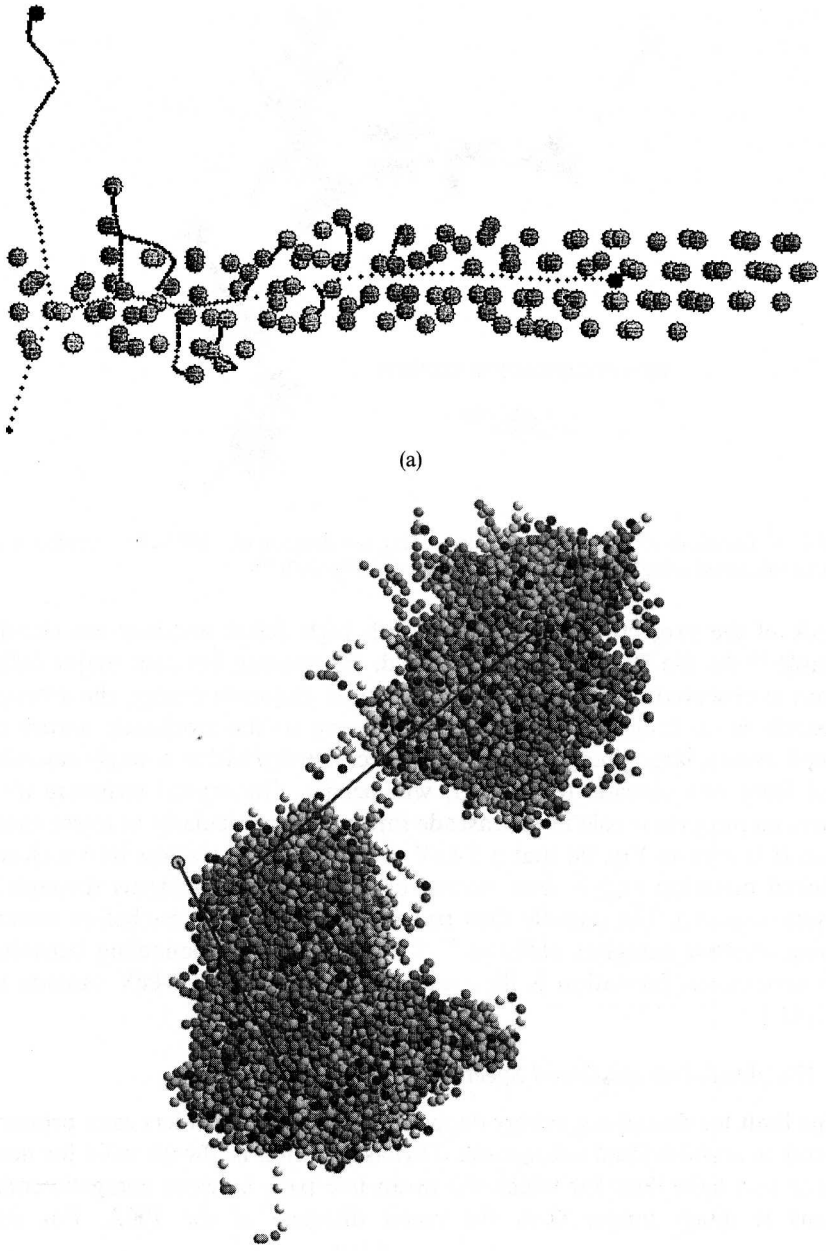

FIG. 9. Molecular dynamics computer simulation showing how channeling can lead to subcascade formation: (a) channeling effect for a 5-keV Ni recoil in Ni; (b) development of a subcascade in a 20-keV cascade in Ni_3Al. (Courtesy of N. V. Doan.[27])

irradiations more generally the irradiation particle is considered the PKA when its energy is less than the cutoff energy for subcascade formation, while its recoil spectra represent the PKAs otherwise. Since the number of atomic displacements resulting from each recoil often varies nearly linearly with damage energy, as evidenced in the KP model, it is useful to construct a function that weights each recoil by its associated damage energy. The integral function $W(E, T)$ is thus defined as

$$W(E, T) = \frac{1}{E_D} \int_{T_{\min}}^{T} dT' \frac{d\sigma(E, T')}{dT'} E_D(T'), \tag{3.7}$$

where E_D is the total damage energy produced by the projectile. $W(E, T)$ represents the fractional damage energy created in all recoils between E_d and energy T. It is shown in Fig. 10 for various 1-MeV particle irradiations of Ni. The usefulness of the $W(E, T)$ function can be realized by considering irradiations of Ni with 1-MeV protons, neutrons, and Ni ions. Since the masses of protons and neutrons are the same, the maximum recoil energies are also the same. On the other hand, the collision cross section for protons is represented by Coulomb scattering, while for neutrons it is nearly hard-sphere scattering. As a consequence, most of the damage energy is deposited in energetic recoils for neutrons but is distributed over a broad spectrum of recoils for protons. For this reason, proton irradiations do not

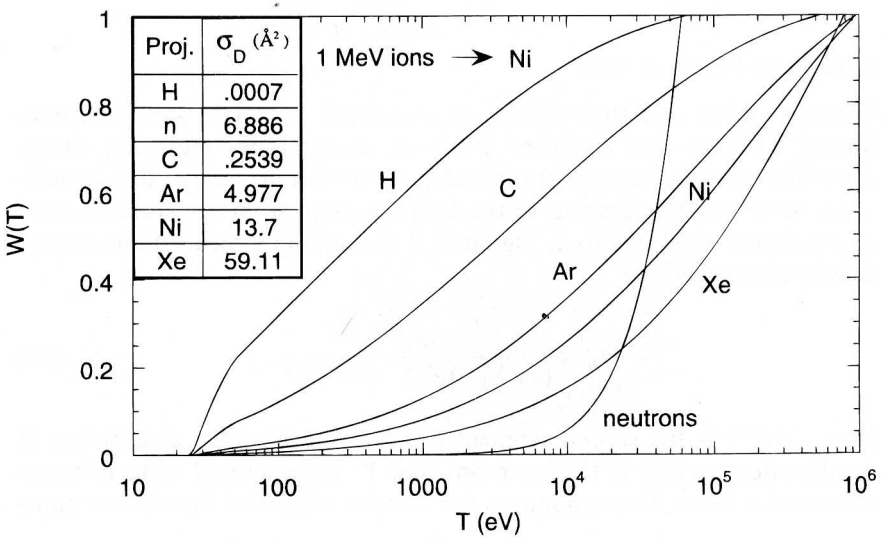

FIG. 10. The $W(E, T)$ function showing the fraction of damage energy produced in recoils below energy T by E = 1-MeV particles in Ni.

provide a good simulation of damage production in materials placed in a fast-neutron environment. The damage spectrum for 1-MeV Ni, however, is far closer to that of fast neutrons, and for this reason, heavy ions are employed to simulate fast neutron damage. Often the parameter, $T_{1/2}$, is employed to represent the recoil spectrum of a particular irradiation. It is the value of T at which $W(E, T) = \frac{1}{2}$, so that half of the damage energy is deposited in recoils above $T_{1/2}$ and half in recoils below it. The inset contains the damage energy cross section σ_D for each particle. It is given by integral in equation 3.7 with the upper limit of integration $T = T_{\max}$; it is not normalized by E_D. The relative amounts of damage energy produced by each particle is given by this cross section.

4. Thermal Spikes

The BCA simulations of defect production discussed in Section 3c suggest that the concentration of defects produced in cascades in a material such as Cu is ≈ 0.01. Since ≈ 50 eV are dissipated in the lattice during the production of each Frenkel pair, the cascade volume will contain an energy density, $\Theta_D \approx 0.5$ eV/atom at the end of the displacement cascade. The corresponding temperature T (assuming that $\Theta_D = 3k_B T$, where k_B is Boltzmann's constant), will be greater than ≈ 2000 K, thus raising the question whether thermal spikes influence cascade dynamics.

a. *Damage-Energy Density*

Thermal spikes and their effects on irradiated materials were first considered by Seitz and Koehler;[1] however, uncertainties regarding energy deposition and heat transport prevented them from arriving at firm conclusions. With the development of the LSS theory of stopping, some of these uncertainties were removed. Sigmund,[28] for example, defined the energy density of a cascade as

$$\Theta_D = \frac{E_D}{(4\pi/3)(\langle \Delta X^2 \rangle + 2Y^2)^{3/2}}. \tag{4.1}$$

Here, $\langle \Delta X^2 \rangle$ is the second moment of the damage-energy distribution in the direction parallel to the ion beam, and Y^2 is the second moment transverse to the beam. These moments can now be calculated from either trans-

[28] P. Sigmund, *Appl. Phys. Lett.* **25**, 169 (1974; **27**, 52 (1975)).

port theory[29] or computer simulation. Energy densities in excess of 1 eV/atom are typical for targets with high atomic numbers. This statistical treatment of cascades, however, does not accurately treat subcascade formation, and therefore it greatly underestimates the local energy densities produced by high-energy particles.

b. Macroscopic Models of Thermal Spikes

Although estimates of energy density illustrate that temperatures in the cascade can well exceed the melting temperature of most materials, a thermal spike description is only meaningful if the lifetime of the spike, τ_c, is long relative to the period of lattice vibrations. An estimate of τ_c for a spherical cascade can be obtained by calculating the time required for the temperature of a cascade containing a damage energy, E_D, to fall below some characteristic temperature, T_x. From the heat equation,

$$\tau_c = \frac{r_c^2 - r_0^2}{4D}, \tag{4.2}$$

where r_c is given by

$$r_c^2 = \left(\frac{E_D}{4\pi k_B T_x N_0}\right)^{2/3} \tag{4.3}$$

and r_0 is the initial radius of the cascade. For a 5 keV cascade in Cu, choosing T_x equal to the melting temperature, T_m, and assuming a (lattice) thermal diffusivity of 1×10^{12} nm^2/s, $\tau_c \approx 2.5$ ps, which is significantly longer than the period of a lattice vibration.

A direct consequence of this formulation of thermal spikes is that every cascade ends in a thermal spike since at sufficiently small T_x, the lifetime of the cascade is long. The influence of thermal spikes on any particular process, therefore, depends on the characteristic energy of the process. For example, the characteristic energy for sputtering is the sublimation energy, typically 5 eV; therefore, sputtering is not usually influenced by thermal spikes. Desorption of gases from surfaces or liquid diffusion, on the other hand, are characterized by very low activation energies, some tenths of electron volts, and therefore they are far more likely to be affected by spikes. It

[29] K. B. Winterbon, Ion Implantation Range and Energy Distributions, IFI Plenum Press New York (1975).

is not surprising that defect production was assumed unaffected by spikes in formulating BCA models since threshold energies for creating Frenkel pairs are ≈ 25 eV.

Various attempts have been made to combine BCA and thermal spike models to account for the distribution of energy along the ion path. The simplest of these considered each primary recoil as a separate subcascade for input into a standard thermal spike model.[30] Alurralde *et al.* used MARLOWE to obtain a more realistic distribution of damage energy in the crystal, and subsequently solved the heat equation numerically.[31] These authors suggested that the number of distinct melt zones within the cascade represented a straightforward measure of the number of subcascades. Additional refinements were incorporated by Kapinos *et al.*, who also employed MARLOWE to generate the initial damage energy distribution, but they also included the effects of electron–phonon coupling (see below) and hydrostatic pressure on the cascade dynamics.[32]

Although these various models all provide some insight into the physics of cascade dynamics, they suffer from the shortcoming of not providing quantitative predictions. The problem arises from the uncertainties in the physical properties of the cascade region. First, the thermal diffusivity of a highly disturbed region, in which temperature gradients of 10^4 K/nm are present, is simply unknown and energy loss by shock waves and focusons are not easily included. Other physical properties of the cascade region are also uncertain. For example, Seitz and Koehler estimated diffusion in the cascade region assuming equilibrium diffusion coefficients and found little atomic mixing.[1] Others have assumed diffusion in a solid containing high supersaturations of point defects or liquid diffusion.[30] These different assumptions, of course, have dramatic effects on the conclusions concerning the significance of thermal spikes, and within the bounds of reasonable assumptions, thermal spike effects can either be substantial or negligible. For these reasons, thermal spike models are currently best employed to provide qualitative ideas about possible behaviors but not used for quantitative predictions.

c. *Electron–Phonon Coupling*

One of the difficulties in estimating cooling rates in cascades derives from the uncertainties in the coupling between the electron and phonon systems when a fast pulse of energy drives one or the other from equilibrium. Seitz

[30] D. Peak and R. S. Averback, *Nucl. Instrum. Methods B* **7/8** (1985).
[31] M. Alluralde, A. Caro, and M. Victoria, *J. Nucl. Mater.* **183**, 33 (1991).
[32] V. G. Kapinos and D. J. Bacon, *Phys. Rev. B* **52**, 4029 (1995).

and Koehler concluded that for cascades in metals such as Cu, cooling by lattice conduction is fast relative to the relaxation time for equilibration between the two systems.[1] For other systems, however, Flynn and Averback showed that the situation was less certain,[33] depending on whether the local electronic system can be heated above the ambient lattice temperature. When this occurs, the phonon system is quenched, owing principally to the heat capacity of the electrons, but heat conduction by the electrons also plays a role. For example, the electronic specific heat of a metal such as Fe at $T = 2T_m$ is already comparable to the lattice specific heat. The heating of electrons in the cascade was estimated by noting that an electron undergoes $n = (R_C/\lambda)^2$ collisions with phonons while it random walks out of the cascade zone absorbing an energy of $\approx k\Theta_D$ in each collision (Θ_D = Debye temperature). For Cu, which has an electron mean free $\lambda \approx 4.5$ nm in the liquid,[34] virtually no heating will occur in a cascade of comparable dimension. The electron mean free path in liquid Fe, on the other hand, is much less, $\lambda \approx 0.045$ nm,[34] and heating becomes possible. In this model the power absorbed by the electronic system is given by

$$P = \frac{4\pi}{3} r_c^2 C_e \lambda v_F \frac{T}{r_c} \frac{\theta_D^2 Q T}{\pi^2 k_B T_0^4}, \tag{4.4}$$

where Q is the deposited energy in the spike, $C_e (= \gamma T)$ the electronic specific heat, v_F the Fermi velocity, T the temperature, $\lambda = 3\pi^2 k_B^2 N(E_F)$, and r_c is the critical radius for the electron and phonon systems to come to equilibrium; it is given by

$$r_c = \frac{r_s \theta_D Q}{3 k_B T_0}, \tag{4.5}$$

where r_s is the radius of the Wigner–Seitz cell and $T_0 = \lambda(T/r_s)$. From the dependence of C_e in Eq. (4.4) it is observed that electron–phonon (e–p) coupling is most significant in metals with a large density of states at the Fermi level; this is expected since more electrons are available to absorb heat and their mean free paths will be short. The question of the importance of e–p coupling affects much of the future discussion, but unfortunately no definitive answer is yet possible. It does appear, however, that in metals with small values of C_e, e–p coupling has at most a small influence.

[33] C. P. Flynn and R. S. Averback, *Phys. Rev. B* **38**, 7118 (1988).
[34] J. S. Brown, *J. Phys. F* **11**, 2099 (1981).

III. Defect Production near Threshold Energies

Calculation of the energy required to remove an atom from its lattice site and transport it into an interstitial site is indeed a difficult problem. Seitz suggested in 1949 that if the process were performed in a reversible manner, it would require an energy of about twice the sublimation energy, $2E_s$, but if it were performed dynamically, the displacement would require about twice that, or $4E_s$. Since materials with strong bonding have a sublimation energy of 5 to 6 eV, Seitz estimated a displacement energy of 25 eV.[35] Improvement on this rough estimate by theoretical means has only been achieved through the use of molecular dynamics (MD) computer simulations, which can properly treat the many-body interactions. Although the potential value of MD for this purpose was recognized around 1959 by Vineyard and co-workers, it is only recently that computational capabilities and realistic interatomic potentials have become available to make it a practical approach. A description of the MD method can be found in the literature;[36] however, owing to the importance of MD simulations for the present article, a brief summary of how this method is used for defect production calculations is provided here.

5. Molecular Dynamics Model

a. *Introduction*

MD simulation is based on the simple integration of the classical equations of motion for an ensemble of atoms in a crystal. Since atom trajectories are computed from forces derived from the gradient of an interatomic potential and integrated using Newton's equations, the simulation can describe the complete phase space available to the system. The MD methods neglects quantum effects in atomic motion, which become important at low temperatures. Simulations at 0 K, therefore, refer to a static lattice. The general procedure now employed to compensate for ground-state vibrations is to set a background temperature of ~ 80 K.

A simulation event is initiated by assigning an appropriate energy to one atom in the crystal interior or by directing an external atom toward the crystal surface. The time step, Δt, between force calculations is selected so that no atom travels a distance greater than $0.01a_0$; otherwise, energy is

[35] F. Seitz, *Discuss. Faraday Soc.* **5**, 271 (1949).

[36] M. P. Allen, and D. J. Tildesley, *Computer Simulation of Liquids*, Oxford Science publications, Oxford (1987).

not conserved and the calculation becomes unstable. Typically, the initial Δt is on the order of 10^{-17} s but is then allowed to increase to a maximum value of 10^{-15} s as the simulation progresses. No standard procedures have been adopted for selecting the size of the computational cell, but generally when the projected range of the projectile is less than one-fourth the length of the cell and the number of atoms in the cell is greater than ≈ 25 times larger than the projectile energy in eV, the boundaries have little influence. Computational cells containing over 10^6 atoms are now possible, thus allowing simulations of recoil events of some tens of keV. Periodic boundary conditions are usually employed, using Langevin dynamics at the boundaries to maintain the background temperature. Damping in the boundaries also helps to prevent the reflection of energy emanating from the cascade.

For low-keV recoils, only $\approx 20\%$ of the cascade energy is lost to electronic stopping, and therefore it has been neglected in most work to date. Electronic stopping, however, is readily implemented in MD. One method adds a viscous force to the equations of motion,

$$m\ddot{\mathbf{x}} = \mathbf{F} - \beta\dot{\mathbf{x}}, \tag{5.1}$$

where β is given in the Lindhard theory by[14]

$$\beta = \frac{0.857 N Z_1^{7/6} Z_2}{(Z_1^{2/3} + Z_2^{2/3})^{3/2}} \qquad \text{Å} - \sqrt{\text{eV}}. \tag{5.2}$$

Damping of thermal modes is avoided by assigning a cutoff energy of 1 eV, below which β is set to zero. Since Langevin dynamics are applied to the atoms in the boundary of the computational cell, the final equation that must be integrated to describe the dynamics of the crystal is given by

$$m\ddot{\mathbf{x}} = \mathbf{F} + \eta(t) - (\beta_{\text{el}} + \beta_{\text{damp}})\dot{\mathbf{x}}, \tag{5.3}$$

where β_{damp} and $\eta(t)$ are applied only to boundary atoms. $\eta(t)$ adds random forces to the boundaries to maintain the bath temperature.[36]

Below 1 eV, the losses from interactions with the electronic system derive from electron–phonon coupling. Caro and Victoria introduced a means to include these losses within the same framework as Lindhard stopping.[37] Their method employs the local density approximation to find the stopping

[37] A. Caro and M. Victoria, *Phys. Rev. A* **40**, 2287 (1989).

power based on the expression[7]

$$S_e(\mathbf{r}) = I(v, \rho(\mathbf{r}))[Z_1^*(v)]^2, \tag{5.4}$$

where I is the interaction of a particle of unit charge with a plasma of density ρ, and Z_1 is the velocity-dependent effective charge of the projectile. The idea is that the stopping of an ion depends only on the local electron density through which it moves, independent of whether it is a vibrating or recoiling atom. The advantage of this approach is that the local electron density at the ion location can be obtained in the MD simulation from the interatomic potentials (see Section 5c). Although Eq. (5.4) cannot be solved at arbitrary velocities for real situations, Caro and Victoria employed theoretical estimates for the solution in different regimes of density and constructed an empirical equation for the stopping power. Since the stopping power is predicted to vary linearly with velocity throughout this range of energies, the results were formulated in a density-dependent stopping constant, β, where

$$\beta = A \log_{10}(\alpha\rho^{1/3} + b). \tag{5.5}$$

Here $\alpha = (3\pi^2)h^2/e^2m$, A is adjustable but approximately $2Z^2e^4m^2/3\pi h^3 = 2 \times 10^{-9}$ g/s and b is an adjustable parameter that contains the information on e–p coupling.[37] The coupling constant varies by approximately two orders of magnitude over the relevant range of densities, which reflects the smaller losses in the e–p coupling than in the stopping power regime. Despite its smaller value of β, e–p coupling can be important since it operates over long times and includes many moving particles.

As the electronic system heats, as described in Section 4c, it feeds energy back into the phonon system. Caro and Victoria[37] have formally included this return energy through the term $\eta(t)$ in Eq. (5.3); however, calculating the local electron temperature requires solving the heat equation for the electronic system. This has not yet been carried out in MD; in fact, the method has only been applied with the assumption that the electronic thermal diffusivity is large relative to the power input by e–p coupling (i.e., systems where e–p coupling is weak). This discussion points out that treating the e–p coupling suffers from many of the same difficulties as thermal spike models. The formalism is clear, but several of the parameters are either unknown or assumed equal to those obtained in spatially homogeneous systems near equilibrium. Implementation of this method for Cu has shown that inclusion of e–p coupling has a noticeable but small effect on

the cascade properties,[38] a result expected for all noble metals for the reasons discussed previously. Nevertheless, the uncertainties in treating electronic stopping and e–p coupling are probably the main sources of error in the MD simulations of simple metals.

b. *Interatomic Potentials*

Interatomic potentials used for calculations of energetic displacement cascades must describe interactions ranging in energy from some hundredths of electron volts to several keV. The procedure generally adopted has been to use force models based on semi empirical many-body potentials to describe the interactions not far from equilibrium and pair potentials, such as the universal potential, to describe the high-energy binary collisions. Several procedures are employed to spline these two potentials. The difficulty has been the ill-prescribed way of turning off the many-body aspects of the low-energy potential as it joins the pair potential. Unfortunately, this must be carried out in the critical range of energies from a few eV to ≈ 25 eV, where few measurable properties are available to guide the procedure, but it is precisely the regime where atoms are displaced by ballistic recoils. The use of the experimental values for the threshold displacement energies as fitting points, however, appears to be a satisfactory solution when they are available. An alternative solution is to calculate fitting points by ab initio methods, but this has not yet been done.

Common choices for the semi-empirical many body potentials are those based on the embedded atom method (EAM)[39] and the method of Finnis and Sinclair.[40] For the EAM, the metal is treated as positively charged ions "embedded" in a local electron density. The energy of the system therefore derives from an embedding energy and the ion core repulsion. The important assumption of this model comes from density functional theory, which states that the total electronic energy is a unique function of the local electron density in which the ion is embedded. The EAM method approximates this local density by the superposition of the atomic densities of the surrounding atoms. The total energy, therefore, is given by

$$E_{\text{tot}} = \sum_j F(\rho_i) + \tfrac{1}{2} \sum_{i,\, j(=i)} \Phi(R_{i,j}). \tag{5.6}$$

The precise forms of the embedding function $F(\rho)$ and the pair potential $\Phi(R)$ can be found in the original references.

---

[38] T. Diaz de la Rubia and M. W. Guinan, *Mater. Res. Forum* **97/99**, 23 (1992).

[39] M. S. Daw and M. I. Baskes, *Phys. Rev. B* **29**, 6443 (1984).

[40] M. W. Finnis and J. E. Sinclair, *Philos. Mag. A* **50**, 45 (1984).

The EAM has been tested and used in a wide variety of applications. It is particularly well suited for close-packed metals; other, somewhat similar effective-medium approaches can be used in other metals. Commonly used EAM potentials give a good description of many bulk effects, such as phonon spectra, thermal expansion, and elastic constants, and a fair description of many surface effects. The melting point of most metals is typically underestimated by the EAM potential. Importantly for studies of irradiation-induced defects, EAM potentials generally give reliable descriptions of point defect formation and migration energies and defect formation volumes.

Isotropic potentials such as EAM are not satisfactory for treating the highly directional nature of the covalent bonds in materials such as Si, so other methods are required. The existing potentials can be classified by how they describe the Si covalent bonding. Cluster potentials employ separate two- and three-body potential terms, where the three-body part carries the burden of favoring the ideal tetrahedral bonding. Cluster functional potentials have the form of a pure two-body potential, but the strength of this potential depends on the local environment of the atom in a way that favors fourfold coordination. Although none of the numerous Si potentials is clearly superior to the others, two of them have been widely used and found to give a fair description of a wide range of different silicon properties.[41] The Stillinger–Weber potential[42] is a cluster-type potential which, contrary to most other potentials, was fitted to both liquid and solid Si properties. It reproduces the experimental melting point accurately, gives a good description of elastic constants, and predicts the lowest-energy vacancy and interstitial configurations correctly. Disadvantages of the potential include a 6% too large cohesive energy and too strong a penalty for structures where atoms have bond angles smaller than 90°. The cluster-functional Tersoff potential describes well many different bonding configurations and can be used to describe all the tetrahedral elements C, Si, and Ge and their alloys. One form of the Tersoff potential is well suited for use with radiation damage problems since it gives accurate elastic constants and a reasonable threshold displacement energy, but it does not give the point defect energies in the right order.[43] The repulsive part of both Stillinger–Weber and Tersoff potentials are grossly unrealistic and must be augmented with an accurate repulsive potential at small interatomic separa-

[41] H. Balamane, T. Halicioglu, and W. A. Tiller, *Phys. Rev. B* **46**, 2250 (1992).
[42] F. H. Stillinger and T. A. Weber, *Phys. Rev. B.* **31**, 5262 (1985).
[43] J. Tersoff, *Phys. Rev. B* **38**, 9902 (1988).

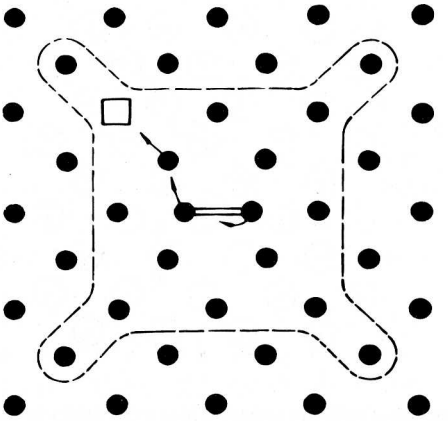

FIG. 11. Schematic representations of the spontaneous recombination volume.

tions, as described for the EAM potential. Recent studies of keV collision cascades in Si have shown that despite their clearly different form and characteristics, the Tersoff and Stillinger–Weber potentials give similar overall results in simulations of collision cascades, suggesting that cascade damage is not overly sensitive to the choice of potential.[44,45] In fact, it appears quite generally that calculations of many cascade properties, including ion beam mixing and defect production, are insensitive to the choice of potential if the displacement energies and the cohesive properties of the solid are properly fit. Calculations of the details of the final defect configurations and the possibility of phase transitions, on the other hand, should be viewed with more caution, especially for more complex structures such as intermetallic compounds and semiconductors.

6. FRENKEL PAIR PRODUCTION AT LOW RECOIL ENERGIES

a. *Introduction*

The production of a stable Frenkel pair requires separating an interstitial atom from its vacancy suitably far to avoid immediate spontaneous recombination. The critical distance of separation and the details of the displace-

[44] T. Diaz de la Rubia and G. H. Gilmer, *Phys. Rev. Lett.* **74**, 2507 (1995).
[45] K. Nordlund and R. S. Averback, *Phys. Rev. B* (in press).

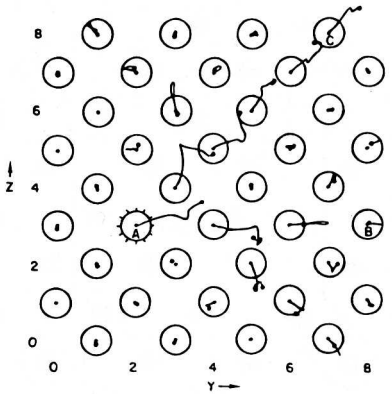

FIG. 12. Replacement collision sequence along the ⟨110⟩ in Cu. (After Ref. 46.)

ment process were elucidated using computer simulation in one of the early applications of molecular dynamics.[46] The region of instability surrounding the vacancy, called the *spontaneous recombination volume* (SRV), is shown schematically in Fig. 11. The mechanism for transporting interstitial atoms beyond the SRV is shown in Fig. 12, where it is seen that one atom replaces the next along a close-packed row. This replacement collision sequence (RCS) terminates with the last atom in the chain being ejected into an interstitial site. These two quantities, the SRV and the RCS, have fundamental importance in the theory of radiation effects. The SRV not only determines the energy required for a displacement, but also the maximum concentration of defects that can be stored in the lattice. The probability of initiating RCSs determines the cross section for creating Frenkel pairs in metals, at least at low energies, while the lengths of RCSs determine the probability that a defect can escape from its vacancy once it becomes mobile.

The Brookhaven simulations, which employed a Born–Mayer potential, obtained a SRV of $\approx 100\Omega_0$ in Cu, which corresponds to an interaction radius of $\approx 1.8a_0$. Radiation annealing experiments have substantiated these approximate results. As shown in Fig. 13, for example, the rate of producing defects in Cu decreases nearly linearly with the instantaneous concentration of defects during 2.8-MeV e^- irradiation.[47] This is understood using the expression

$$\frac{dc}{d\phi} = \sigma(1 - \alpha_i c_i - \alpha_v c_v + O(c^2) \approx \sigma(1 - 2\alpha c), \tag{6.1}$$

[46] J. B. Gibson, A. N. Goland, M. Milgram, and G. H. Vineyard, *Phys. Rev.* **120**, 1229 (1960).

where α_i (α_v) is the volume around an interstitial atom (vacancy) in which a vacancy (interstitial) is unstable. Higher-order terms are required to treat overlap of SRVs. The right side of the equation assumes that $\alpha_i = \alpha_v = \alpha$ and that $c_i = c_v$. The initial slope of the curve in Fig. 13 yields -2α. Typical values of α deduced from these experiments[48] are $125\Omega_0$, Cu; $48\Omega_0$, Pt; and $125\Omega_0$, Au, which are in satisfactory agreement with the MD calculations.

The large SRVs in close-packed metals have a direct bearing on the way Frenkel pairs are produced. For example, separating an atom a distance of $1.8a_0$ from its lattice site in Cu requires an energy of ≈ 200 eV, whereas the experimental value for producing a Frenkel defect in Cu is ≈ 20 eV. The low threshold energy for displacements illustrates the importance of the RCS mechanism. The same mechanism for defect production was found by

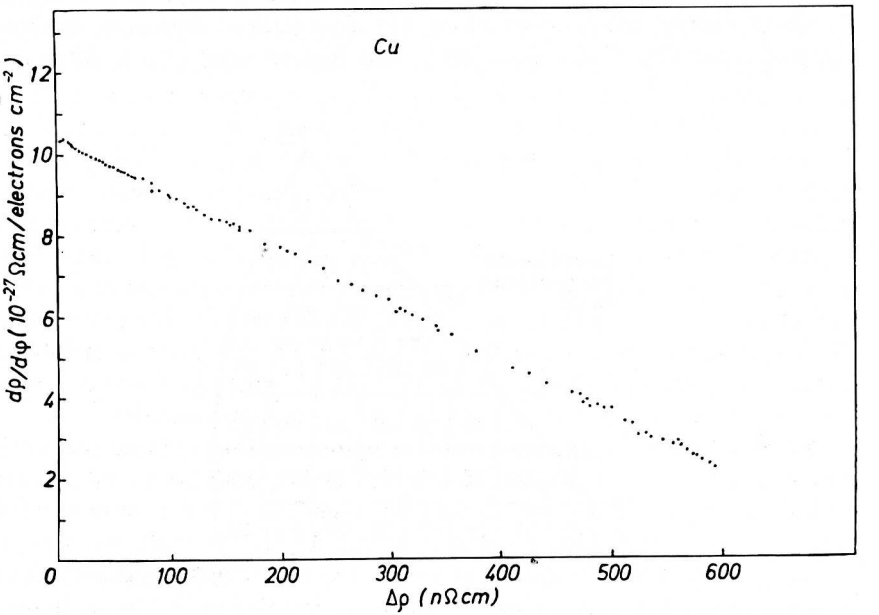

FIG. 13. Damage rate curve for 2.8-MeV e^- irradiation of Cu at 4.6 K. (After Ref. 47.)

[47] G. Deussing and W. Schilling, *Cryst. Lattice Defects* **1**, 55 (1969).

[48] H. J. Wollenberger, in Vacancies and Interstitials in Metals, ed. A. Seeger, D. Schumacher, W. Schilling, and J. Diehl, North-Holland, Amsterdam (1970), p. 215.

the Brookhaven group for the more open body-centered-cubic structure of Fe.[49] The RCS mechanism has been confirmed experimentally by measurements of perturbed angular correlation (PAC) on a Cu sample doped with radioactive ^{111}Sn.[50] When ^{111}Sn decays into ^{111}In, it emits a neutrino which causes the excited nucleus to recoil with an energy of 29 eV and thus to create a Frenkel pair. Subsequent measurements of the PAC signal on the ^{111}In probe revealed that it was located on a lattice site and adjacent to a vacancy. This demonstrated that the ^{111}In recoil has replaced its neighbor, leaving a vacancy behind, and has not become an interstitial atom itself some distance away from the vacancy.

A careful study of the dependence of the threshold energy in Cu on recoil direction was performed by King *et al.*, who employed in situ electrical resistivity measurements on electron-irradiated thin films.[51] By varying the energy of the electron beam and the orientation of the Cu film, they were able to map the threshold energy surface accurately. Their results are illustrated in Fig. 14. Note that the surface is rather anisotropic, with the threshold energy being lowest along the close-packed directions in face-centered-cubic Cu, ⟨110⟩ and ⟨100⟩, and highest near ⟨111⟩. Although

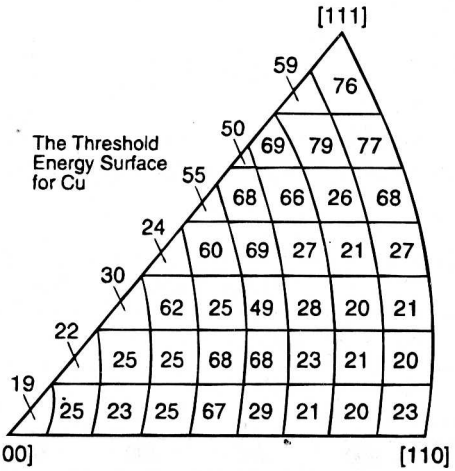

FIG. 14. Threshold energy surface for producing Frenkel pairs in Cu. (After Ref. 51.)

[49] C. Erginsoy, G. H. Vineyard, and A. Englert, *Phys. Rev.* **133**, A595 (1964).
[50] H. Metzner, R. Sielemann, S. Klaumünster, and E. Hunger, *Phys. Rev. B* **36**, 9535 (1987).
[51] Reprinted from W. E. King, K. I. Merkle, and M. Meshi, *J. Nucl. Mater.* **117**, 12 (1983) with kind permission from Elsevier Science–NL, Sara Burgerhartstraat 25, 1055 KV Amsterdam, The Netherlands.

detailed threshold surfaces like that shown in Fig. 14 are not available for many materials, the minimum threshold energy has been determined for many materials using electron irradiations on polycrystalline samples; these are tabulated in Table 2.

The understanding of RCSs derives from the original analysis of focused collision sequences by Silsbee.[52] The case of simple focusing of hard spheres is illustrated in Fig. 15. If one of the spheres recoils at an angle θ_1 with respect to the row, its neighbor will recoil at angle θ_2, where from Fig. 15,

$$(D - 2R)\theta_1 = -2R\theta_2 . \tag{6.2}$$

where R is the hard-sphere radius and D is the interatomic spacing. The ratio θ_2/θ_1, or focusing parameter, f, is given by

$$f = -\frac{\theta_2}{\theta_1} = \frac{D}{2R} - 1. \tag{6.3}$$

For equal spacing of atoms along the row,

$$\theta_n = (-f)^n \theta_0 . \tag{6.4}$$

For $D < 4R$, $f < 1$ and θ_n converges. The momentum in this case becomes focused along the atomic row. Equation (6.3) illustrates that focusing is

TABLE 2. THRESHOLD ENERGIES FOR FRENKEL PAIR PRODUCTION IN VARIOUS METALS AND SEMICONDUCTORS

METALS	Ag	Al	Au	Cu	Fe	Ni	Mo	Pt	W	SS
T_d(eV)	25	16	36	19	17	23	33	34	41	18
SEMICONDUCTORS	C_{dia}	C_{gr}		GaAs	Ge	Si				
T_d(eV)	35	25		10	15	13				

Source: Data from P. Lucasson, in *Fundamental Aspects of Radiation Damage in Metals*, ed. M. T. Robinson and F. W. Yound, Jr., ERDA Report CONF-751006 (1975) p. 42; and H. H. Andersen, *Appl. Phys.* **18**, 131 (1979).

[52] R. H. Silsbee, *J. Appl. Phys.* **28**, 1246 (1957).

favored in targets with atoms having large hard-sphere radii and along close-packed directions. Since the hard-sphere radius of an atom depends on its atomic number and its energy (as noted in Section 2a), focusing is a low-energy phenomenon that is most efficient in heavy close-packed materials. Lehmann and Leibfried, for example, calculated maximum focusing energies of 36 eV in Cu and 170 eV in Au.[53]

Although the discussion above refers to the focusing of momentum, the same principle applies to RCSs. Energy is lost, however, in each replacement collision by interactions with neighbors as the recoil atom passes through its saddle point. The number of replacements, therefore, increases with increasing recoil energy from the minimum displacement energy up to the maximum focusing energy. It is also expected from these arguments that the lengths of RCSs will decrease with increasing temperature and other imperfections in the lattice. Calculations of RCSs in Au along ⟨110⟩ show, however, that once ground-state vibrations have been included, the effect of temperature is not overly large, reducing the maximum number of focused collisions from 66 at 0 K (159 in a static lattice at 0 K) to 39 at 340 K.[54]

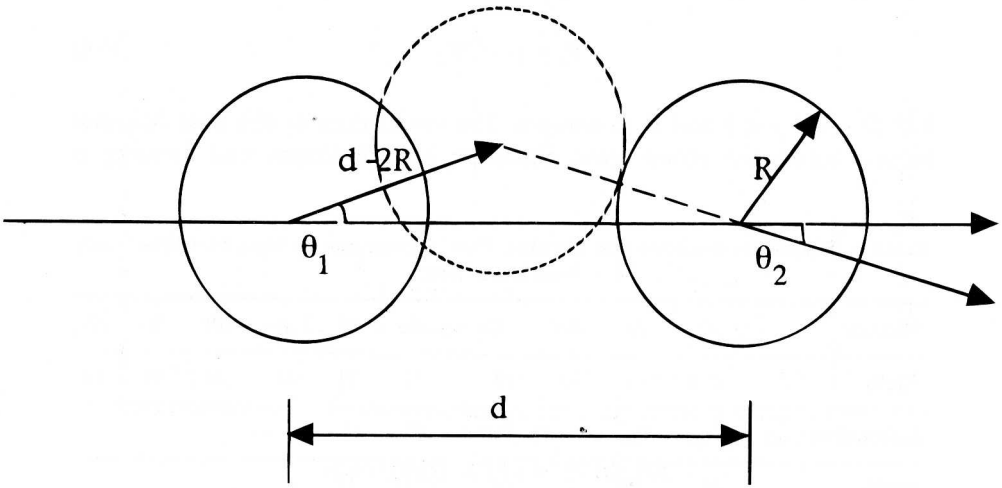

FIG. 15. Geometry of focusing collisions with hard spheres.

[53] C. Lehmann and G. Leibfried, *J. Appl. Phys.* **34**, 2821 (1963).
[54] M. W. Thompson, Defects Radiation Damage in Metals, Cambridge University Press, Cambridge (1969), p. 211.

b. *Threshold Energy Surfaces and Displacement Energies: Computer Simulation*

(i) PURE METALS. The threshold surface of Cu was examined carefully by King and Benedek[55] using pair potentials and more recently by Foreman *et al.*[56] using more realistic many-body potentials. Results from the latter work are illustrated in Fig. 16 along with the experimental results of King *et al.*[51] The remarkably good agreement between the simulations and experiments provides a degree of confidence in the reliability of the simulations. It should be noted that Foreman *et al.* fit the repulsive, short-range part of their potential to two points on the experimental threshold surface (indicated in Fig. 16), as discussed in Section 5b.

The lengths of the RCSs were not examined by Foreman *et al.*, although they reported that lengths of ≈ 6 nm or more were typical along the $\langle 110 \rangle$ at 0 K. Unfortunately, the computational cell employed in the study did not

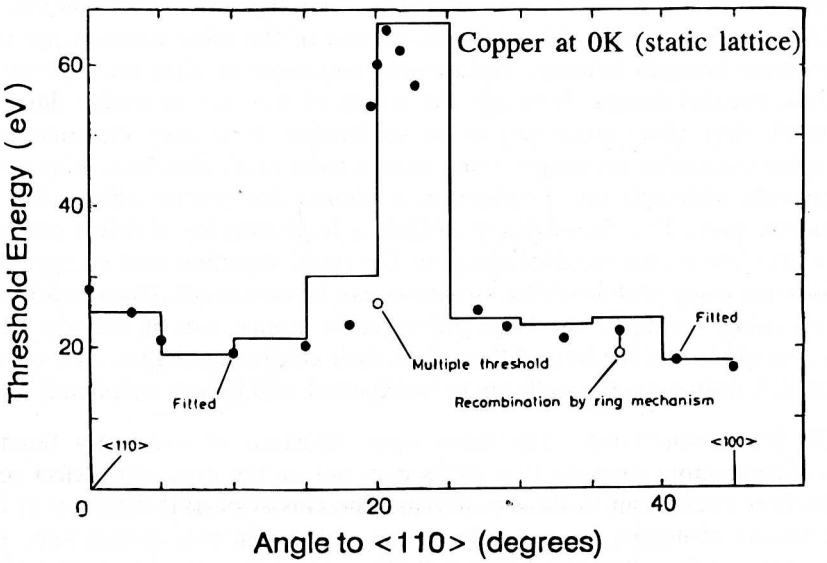

FIG. 16. Threshold energy surface for Cu computed using MD simulation. Experimental data of King *et al.* [51] are included for comparison. (After Ref. 56.)

[55] W. E. King and R. Benedek, *Phys. Rev. B* **23**, 6335 (1981).
[56] A. J. E. Foreman, W. J. Phythian, and C. A. English, *Philos. Mag. A* **66**, 655 (1992).

allow for longer sequences to propagate. For displacements in Ni at 0 K, Gao and Bacon reported RCSs in the ⟨110⟩ direction as long as 90 Å.[57] It is also observed in 0-K simulations that RCSs propagating along closed-packed directions end with the interstitial in an unstable crowd-ion configuration, and unless they are well beyond the SRV, they tend to return to their vacancy. Few simulations have been performed at elevated temperatures or when there are imperfections in the lattice. The theoretical calculations noted above and simulations by Foreman *et al.*[56] show, however, that RCSs lose more energy per replacement in these cases. Additionally, the interstitials in these events can convert from the unstable crowd-ion configuration to a more stable configuration and avoid recombination. As a consequence, the displacement energy is likely to be about the same at high and low temperatures. This was indeed observed by Gao and Bacon in Ni_3Al.[58] The sensitivity of the lengths of RCSs to the choice of potential has not yet been carefully examined.

(ii) Ordered and Random Alloys. Threshold energy surfaces in ordered Ni_3Al[58,59] and β-NiAl[60] have now been investigated by MD simulation. Of interest is whether the different masses of the alloy components and ordering energies influence replacement sequences or alter the stability of close Frenkel defects. Although the results of the various studies differ in detail, they share some important similarities. First they illustrate that replacements can propagate along atomic rows containing both alloy components, although the propagation is shorter for greater mismatches in atomic mass. For the NiAl compounds a large number of defect configurations are produced, depending on the recoil direction and energy. The SRV for many of these defect structures can be very small. This result is not surprising, owing to the large difference in atomic size of the two alloy components and the large difference in their electronegativities. As a consequence, deep potential wells are to be expected, and indeed, calculated.[58–61]

(iii) Semiconductors. The more open structure of covalently bonded semiconductors suggests that RCSs may not be the dominant defect production mechanism in these materials. The closest-packed direction in the diamond structure, for example, is the ⟨111⟩. On this atomic row, the atomic spacing alternates between $0.433a_0$ and $1.30a_0$, and from Fig. 15 it is clear that this arrangement is unfavorable for RCSs. MD simulations

[57] F. Gao and D. J. Bacon, *Philos. Mag. A* **67**, 289 (1993).
[58] F. Gao and D. J. Bacon, *Philos. Mag. A* **71**, 43 (1995).
[59] A. Caro, M. Victoria, and R. S. Averback, *J. Mater. Res.* **51**, 409 (1990).
[60] H. Zhu, R. S. Averback, and M. Nastasi, *Philos. Mag. A* **71**, 735 (1995).
[61] A. Caro and D. F. Pedrazza, *Nucl. Instrum. Methods B* **59/60**, 880 (1991).

have now been performed on Si,[62,63] GaAs,[64] and AlAs.[62] The main differences in defect production near threshold energies between these covalently bonded materials and metals are: (1) threshold energies tend to be much smaller in semiconductors; (2) replacement sequences are far shorter; and (3) Frenkel pair production by the direct recoil of atoms into interstitial sites is a more common displacement path. The lower threshold energy in semiconductors can be understood by the smaller SRVs in these materials. Recombination distances of $\approx 0.45a_0$ have been reported for Si and GaAs, and $0.67a_0$ for AlAs,[62] which compare to $\approx 1.8a_0$ in metals. These small SRVs also make it possible for the direct ejection of an atom into an interstitial site without the need for an RCS. In fact, the difficulty of creating defects by $\langle 111 \rangle$ RCSs is illustrated by the result in GaAs that the threshold energy for Frenkel pair production ($=10$ eV) is significantly smaller than that for antisite defect production ($=20$ eV); antisite defects are produced by $\langle 111 \rangle$ replacement sequences in GaAs.[64] Although the configurations of the defects and the exact values of the recombination distances are likely to be sensitive to the potentials in semiconductors, the general trends cited here appear to be fairly robust.

c. *Experimental Determinations of the Lengths of Replacement Sequences in Metals*

A large number of experiments have been designed to determine the lengths of RCSs, owing to their importance in the theory of radiation effects. A few of the more significant of these are described here, but they represent few systems, so that general conclusions cannot be made.

(i) STAGE I RECOVERY. Since Frenkel pairs are produced by RCSs in metals during electron irradiation, the minimum RCS length can be estimated from measurements of SRVs. As noted above, this yields $R_{\mathrm{SRV}} \approx 3$ replacements in metals. Additional information is obtained by considering the recovery of defects during low-temperature annealing (annealing is discussed in Section 17a). It is now known that recovery at low temperatures is due to interstitial migration. Since the probability of a randomly migrating defect to escape from its own vacancy is given by[48]

$$P = 1 - \frac{R_{\mathrm{SRV}}}{R_{\mathrm{RCS}}}, \tag{6.5}$$

---

[62] M. Sayed, J. H. Jefferson, A. B. Walker, and A. G. Cullis, *Nucl. Instrum. Methods B* **102**, 232 (1995).

[63] M. J. Caturla, T. Diaz de la Rubia, and G. H. Gilmer, *Mater. Res. Soc. Symp. Proc.* **316**, 141 (1994).

[64] T. Mattila and R. M. Nieminen, *Phys. Rev. Lett.* **74**, 2721 (1995).

a lower bound on the length of RCSs can be obtained by measuring the residual damage remaining after the interstitials have migrated. (Impurities are added to the samples in these experiments in order to trap interstitials that escape from their own vacancy before they recombine with another vacancy elsewhere in the specimen.) Typical values of P for e^- irradiated metals are $\approx \frac{1}{3}$,[65] suggesting that the average RCS length is ≈ 4 to 5 replacements. If it is assumed that the length distribution, $f(x)$, falls off exponentially with number of replacements, x, then Eq. (6.5) with the conditions $P = \frac{1}{3}$ and $x_{\min} = 3$ yields $f(x) = 2.07 \exp(-0.485x)$. The average length of RCSs for e^- irradiated metals is then $\langle x \rangle \approx 5.2$ replacements per displacement.

(ii) Disordering of Order–Disorder Alloys. Ordered alloys provide an opportunity to probe atomic rearrangements since various physical properties are sensitive to changes in chemical order. Kirk *et al.* measured the change in magnetization of Ni_3Mn to obtain its disordering rate during thermal neutron irradiation.[66] The magnetization behavior of Ni_3Mn, which has the Cu_3Au structure, is particularly interesting for disordering studies since according to the theory of Marcinkowski, each Mn atom aligns ferromagnetically with nearest-neighbor Ni atoms, unless three or more nearest-neighbor Mn atoms are present, in which case the central Mn atom aligns antiferromagnetically.[67] The passage of a $\langle 110 \rangle$ RCS in Ni_3Mn, therefore, will not induce a spin flip in a fully ordered alloy (only two nearest-neighbor Mn would be present), but it can in a partially ordered alloy. The number of $\langle 110 \rangle$ exchanges could thus be obtained by measuring the change in magnetization during irradiation for a series of alloys prepared with different long-range-order (LRO) parameters. The results of this study are illustrated in Fig. 17, where the number of magnetic spin flips are plotted as a function of the initial LRO parameter. The best fit to the experimental data was obtained assuming that 80 $\langle 110 \rangle$ replacements were produced per primary recoil event along Ni–Mn rows, as indicated in the figure. If sequences along Ni–Ni and Ni–Mn $\langle 110 \rangle$ rows are equally probable, then 160 replacements would have occurred per recoil event. Accounting for the larger capture cross section for Mn than for Ni (13.2 barns versus 4.7 barns), Kirk *et al.*[66] concluded that the number of $\langle 110 \rangle$ replacements is 112 to 150 per recoil event. Since the average recoil energy for thermal neutron capture in Ni_3Mn is 450 eV, more than one

[65] See, e.g., W. Schilling, G. Burger, K. Isebeck, and H. Wenzl, in Vacancies and Interstitials in Metals, ed. A. Seeger, D. Schumacher, W. Schilling, and J. Diehl, North-Holland, Amsterdam (1970), p. 255.

[66] M. A. Kirk, T. H. Blewitt, and T. L. Scott, *Phys. Rev. B* **15**, 2914 (1977).

[67] M. J. Marcinkowski and R. M. Poliak, *Philos. Mag.* **8**, 1023 (1963).

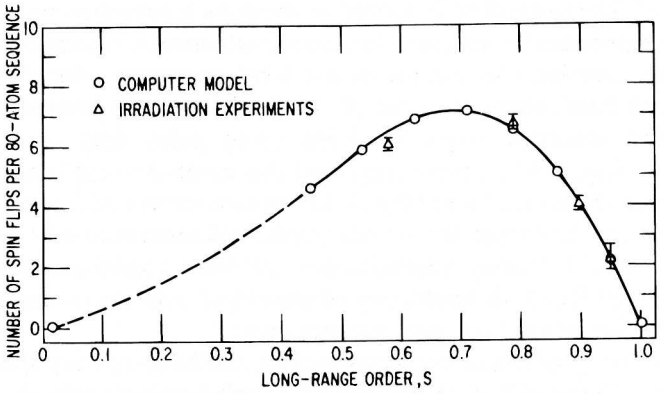

FIG. 17. Comparison between the computed number of spin flips of Mn atoms per 80-atom RCS and the measured number of spin flips shown as a function of long-range-order parameter in Ni_3Mn. (After Ref. 66.)

RCS could be generated by each recoil event. Measurements have shown that an average of four Frenkel pairs are produced by each recoil event, so the magnetization results can be restated as 33 $\langle 110 \rangle$ replacements per actual Frenkel pair, or based on dpa calculations [see Eq. (3.5)], their results yield 22 replacements per displacement.

Electron irradiations have also been performed on Ni_3Mn to examine disordering rates. For these, electrical resistivity measurements were used to monitor the LRO parameter during irradiation. The details of disordering experiments are discussed in Section 9c; however, these studies showed that during e^- irradiation, only four replacements were produced per displacement.[68] The reason for the substantial difference in these two experiments is uncertain, but the less energetic recoil spectrum of electrons is a likely factor. If the Frenkel pairs are produced just above the threshold energy, as for e^- irradiation, little energy is available for the propagation of long RCSs, (i.e., each Frenkel pair requires a recoil of E_d), whereas for 450-eV recoils, more than $2E_d$ [see Eq. (3.5)] is available for the propagation of each RCS.

(iii) FIELD ION MICROSCOPY OF W. The locations of point defects can be directly mapped in three dimensions using field ion microscopy (FIM)

[68] D. Becker, F. Dworschak, C. Lehmann, K. T. Rie, H. Schuster, H. Wollenberger, and J. Wurm, *Phys. Status Solidi* a **81**, 145 (1968).

methods.[69] The procedure is simply to irradiate a specimen with energetic ions and subsequently, measure the distances between vacancies and interstitials. In practice, the surface of the FIM specimen, which is a sharp needle with hemispherical radius of ≈ 15 to 30 nm, is imaged while dissecting the specimen atom by atom using pulse field evaporation.[70] Seidman and co-workers have employed this method to examine the defect structure produced by 20 to 30-keV ion bombardment of W at 18 K. For irradiations of this type, the recoils produce displacements in a compact zone, and at 18 K neither vacancies nor interstitial atoms are mobile in W. The lengths of RCSs, therefore, can be associated with the distance between the interstitials and the compact vacancy zone.

The relative position of vacancies and interstitial atoms are shown in an isometric drawing in Fig. 18 for 20-keV to self-bombardment of W.[71] The vacancies are contained in a single compact zone called a depleted zone, described later. The interstitial atoms, on the other hand, are scattered throughout the tip. Since no vacancies were observed outside the depleted zone, the interstitials could safely be assumed to have emanated from the depleted zone. The lengths of RCSs was thus estimated by measuring the shortest distances between the interstitial atoms and the depleted zone

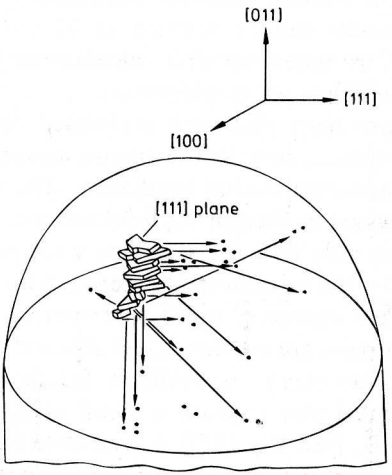

FIG. 18. Isometric drawing showing the locations of interstitial atoms and vacancies in an FIM specimen following the impact of a single 20-keV W ion. (After Ref. 71.)

[69] E. W. Müller and T. T. Tsong, Field Ion Microscopy, Elsevier, New York (1969).
[70] See, e.g., D. N. Seidman, in Radiation Damage in Metals, ed. S. D. Harkness and N. L. Peterson, American Society for Metals, Metals Park, OH (1976), p. 28.
[71] L. A. Beavan, R. M. Scanlan, and D. N. Seidman, *Acta. Metall.* **19**, 1339 (1971).

along a close-packed direction. A composite histogram of RCS lengths obtained from several cascade events is shown in Fig. 19.[72] The distribution falls off approximately exponentially with distance and has a mean length of 16 nm, or ≈ 50 replacements.

(iv) SEMICONDUCTORS: DIFFUSE X-RAY SCATTERING. No direct measurements of the lengths of RCSs have been performed in semiconductors; however, it has been shown by Huang diffuse x-ray scattering (HDS) measurements that most interstitial atoms are displaced only very short distances from their vacancies. Huang scattering refers to the symmetrical part of the x-ray scattering from defects around a reciprocal lattice vector. In the limit of small defect concentrations, the HDS intensity is given by the expression[73]

$$S(\mathbf{k}) = \langle |\tilde{c}(\mathbf{q})|^2 \rangle |A(\mathbf{k})|^2 \tag{6.6}$$

where $\mathbf{q} = \mathbf{k} - \mathbf{G}$, $\mathbf{k}$ is the scattering vector, and $\mathbf{G}$ is the reciprocal lattice vector closest to $\mathbf{k}$. $A(\mathbf{k})$ is the scattering intensity from a single defect and varies as $1/q^2$ at small q. $c(\mathbf{q})$ is the Fourier transform of the spatial fluctuations in the defect concentration. For randomly distributed defects at small

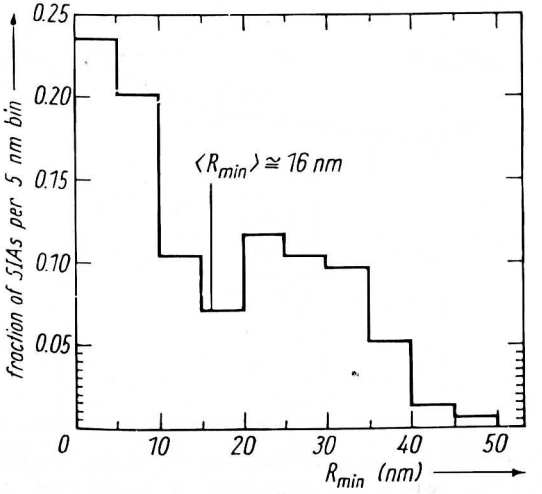

FIG. 19. Composite histogram for the lengths of RCSs in W produced by 20-keV self-ions. (After Ref. 72.)

[72] C. Y. Wei and D. N. Seidman, *Philos. Mag. A* **43**, 1419 (1981).
[73] See, e.g., P. Ehrhart, *J. Nucl. Mater.* **216**, 170 (1994).

concentrations, $\langle |\tilde{c}(\mathbf{q})|^2 \rangle = c(1-c) \approx c$. Thus deviations of $q^2 S(\mathbf{k})$ from a horizontal line when plotted versus q reveal the composition fluctuations in the defect distribution. Since the locations of an interstitial atoms are correlated with their own vacancies, their distance of separation can be probed by measuring $\langle |\tilde{c}(\mathbf{q})|^2 \rangle$. For an interstitial separated from a vacancy by a distance **R**, the fluctuation takes the form, $A(1 - \cos \mathbf{qR})$, where A varies as $1/q^2$. The results of HDS measurements performed on electron irradiated Si at 4.6 K are illustrated in Fig. 20; they show correlation effects of the type described. From these data, Ehrhart and Zillgen deduced that the maximum separation between most interstitials and vacancies, R, is <0.8 nm.[74] (The data do not extend to larger values of q to probe smaller separa-

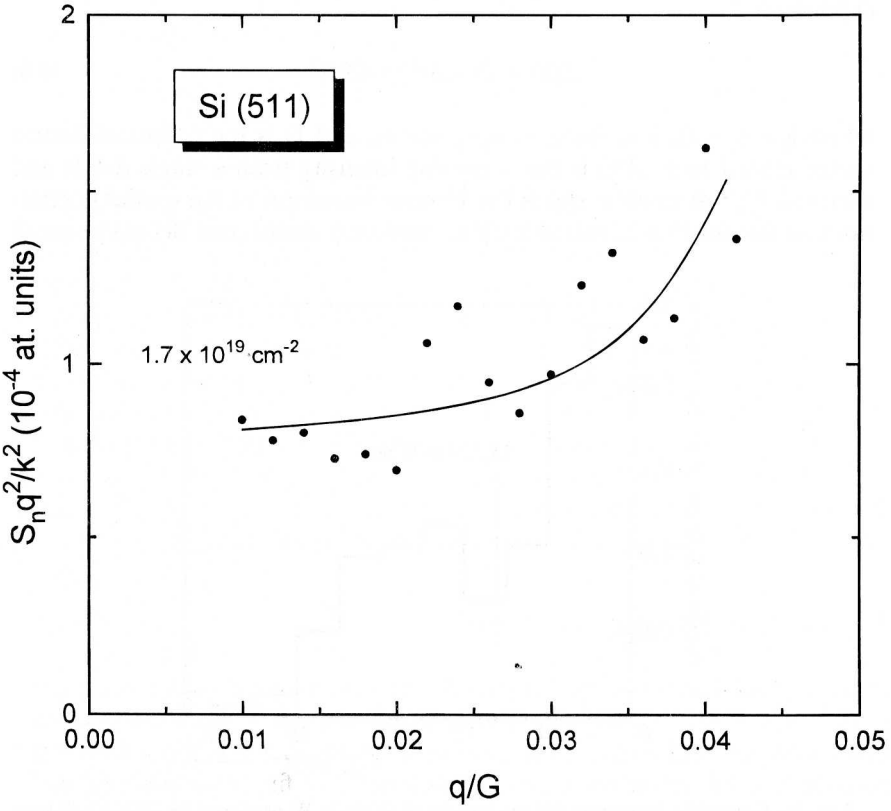

FIG. 20. Huang diffuse scattering from point defects produced in Si during 3-MeV e^- irradiation. (After Ref. 74.)

[74] Reprinted from P. Ehrhart and H. Zillgen, *Nucl. Instrum. Methods* in press with kind permission from Elsevier Science–NL, Sara Burgerhartstraat 25, 1055 KV Amsterdam, The Netherlands.

tions.) This same method was employed for GaAs, for which $R \approx 1.0$ nm,[75] and for InP, for which $R \approx 0.6$ nm.[76] These small separations are in agreement with the predictions of the MD simulations. It can be concluded, therefore, that replacement sequences are, indeed, short in semiconductors and that close interstitial–vacancy configurations are stable. The somewhat larger separation in GaAs may indicate that replacement sequences are longer in this material. Pillukat and Ehrhart noted that the details of the scattering data suggested that the defects were displaced along $\langle 111 \rangle$. They also found for higher energy recoils ~ 20 eV, that the measured relaxation volumes per defect were large, indicating that double displacements were involved, (i.e., two Frenkel pairs were produced). These results thus indicate that short replacements sequences do occur GaAs.[75]

IV. Dynamics of Collision Cascades: Beyond BCA Models

A fundamental assumption of the BCA model is that defects are produced in isolation, without interference from nearby recoils. As a consequence, these models either use average displacement energies or SRVs deduced from threshold energy experiments as their criteria for defect production. As pointed out in Section III, the creation of a Frenkel pair agitates the lattice over extended distances so that the production of many defects in close proximity may alter their stability. Thermal spike models, on the other hand, completely neglect the atomic displacement process. Although attempts have been made to synthesize these two descriptions, assuming that the cascade region thermalizes only after the ballistic phase has ended, they do not offer a satisfactory solution to the complex dynamics of collision cascades. A firm theoretical description of the atomic displacement process has only been obtained through the use of MD simulations.

7. Collective Behavior in Cascades

Fundamental findings of the MD simulations of energetic displacement cascades are that the cascade region undergoes local melting and that melting has a profound influence on the number of atoms that are displaced in the cascade and on the primary state of damage.[77] A first indication of local

[75] A. Pillukat, K. Karsten, and P. Ehrhart, *Phys. Rev. B* **53**, 7823 (1996).
[76] K. Karsten and P. Ehrhart, *Phys. Rev. B* **51**, 10508 (1995).
[77] R. S. Averback, T. Diaz de la Rubia, and R. Benedek, *Nucl. Instrum. Methods B* **33**, 693 (1988).

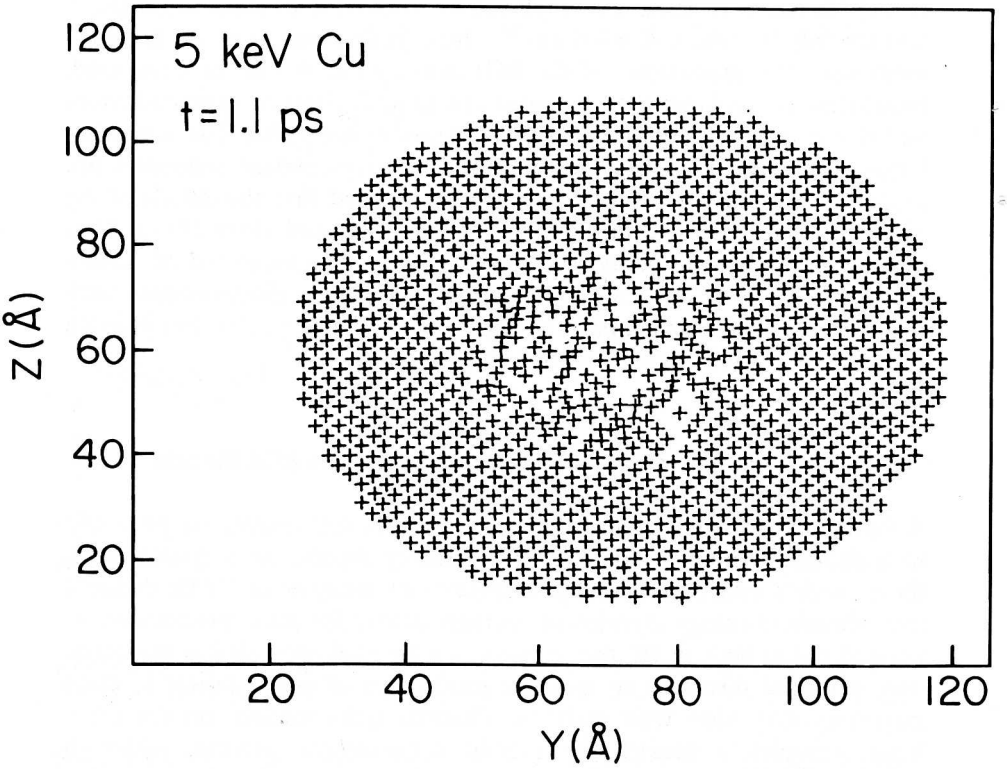

FIG. 21. Cross-sectional slice of thickness $a_0/2$ through the center of a 5-keV cascade in Cu, showing atom locations after 1.1 ps. (After Ref. 78.)

melting is illustrated in Fig. 21, where a compact, structurally disordered zone is observed at the center of a 5-keV cascade in Cu. In addition, a well-defined interface separating two distinct phases are seen in this figure.[78] This is not surprising since by 1.1 ps, several lattice vibrations have occurred, allowing local equilibration. Additional evidence for local melting is shown in Fig. 22, where the pair correlation functions, $g(r)$, for those atoms in the disordered zone are compared with the pair correlation function for liquid Cu. The similarity is remarkable, most notable is the disappearance of the (200) peak in crystalline Cu at $r = 3.6$ Å. Although these first simulations of cascades in Cu were performed with a Born–Mayer pair potential, the same behavior has been reproduced using many-body poten-

[78] T. Diaz de la Rubia, R. S. Averback, R. Benedek, and W. E. King, *Phys. Rev. Lett.* **59**, 1930 (1987).

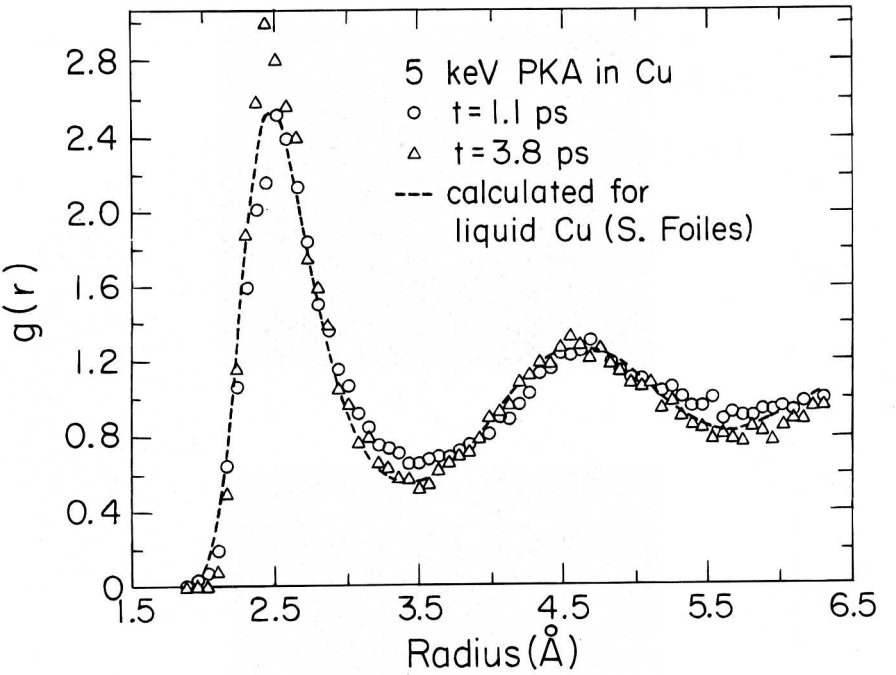

FIG. 22. Pair correlation function for atoms in the core of the cascade at 1.1 ps and 3.83 ps. Also shown is the pair correlation function for liquid Cu as calculated by Foiles. (After Ref. 78.)

tials. Figure 23, for example, shows a 25-keV event in Cu simulated using EAM potentials.[79] The general features are the same as those in Fig. 21. This higher-energy event also shows the onset of subcascade formation, although in this particular case the separate branches of the cascade subsequently melt into a single cascade. The observation of local melting, with its attendant features of high pressure, liquidlike diffusion, and a resolidification front provides the basis for understanding many aspects of cascade damage.

The melt has been further characterized by its temperature and density. The local temperature in the 5-keV cascade described above is plotted at different instants of time in Fig. 24a as a function of distance from its center of energy. The temperature (assuming that $\frac{3}{2}k_B T$ = average kinetic energy/atom) is observed to exceed the melting temperature out to a distance ≈ 2.0 nm, and the center of the cascade remains above the melting temperature

[79] Reprinted from T. Diaz de la Rubia and M. W. Guinan, *Mater. Res. Forum*, **97/99**, 23 (1992) with kind permission from Elsevier Science–NL, Sara Burgerhartstraat 25, 1055 KV Amsterdam, The Netherlands.

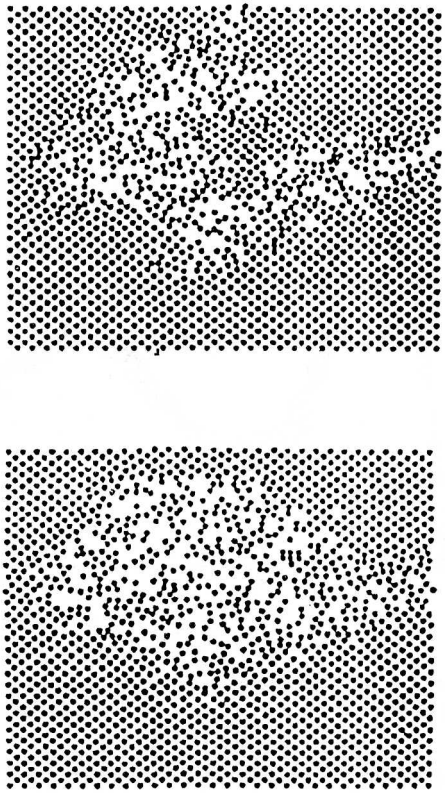

FIG. 23. Cross-sectional slice of thickness $a_0/2$ through the center of a 25-keV cascade in Cu at two different times: (a) 0.19 ps; (b) 1.01 ps. (After Ref. 79.)

for nearly 5 ps. The melting temperature of the potential used in this study is ≈ 1150 K.[80] The variation of atomic density with distance from the center of energy is shown in Fig. 24b for the 5-keV event. At 0.25 ps, the temperature in the cascade interior is ≈ 5000 K, yet the density is only somewhat smaller than that of the solid. This illustrates that the cascade has not yet equilibrated, even on a local scale. By 1.41 ps, however, the temperature has cooled to $\approx 2T_m$ and the density has decreased by ≈ 15 to 20%; this change is a factor of 2 more than for equilibrium melting. Outside the cascade core, a ridge of high density is formed. These changes in density are not due to the ejection of interstitial atoms into the periphery, as pictured by Brinkman in Fig. 1,[5] but rather, to a pressure wave associ-

[80] H. Hsieh, T. Diaz de la Rubia, R. S. Averback, and R. Benedek, *Phys. Rev. B* **40**, 9986 (1989).

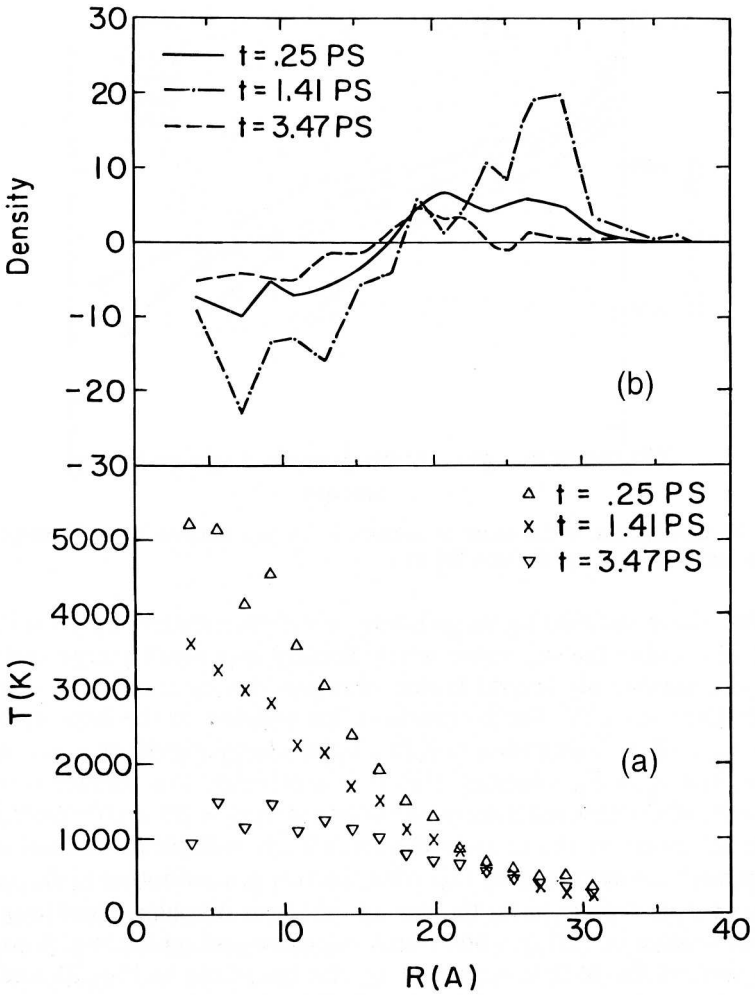

FIG. 24. (a) Local temperature and (b) density as a function of distance from the center of energy in the cascade. (After Ref. 79.)

ated with the rapid heating of the lattice and local melting. After the cascade has cooled, the density returns to nearly that of the perfect solid.

Cooling rates in cascades were studied in more detail in Cu using EAM potentials.[81] In Fig. 25 the temperature at the center of the cascade is plotted as a function of time for different cascade energies. The lifetime of the cascade, τ_{sp}, defined here as the time that the center of the cascade

[81] Reprinted from T. Diaz de la Rubia and W. J. Phythian, *J. Nucl. Mater.* **191/194**, 108 (1992) with kind permission from Elsevier Science–NL, Sara Burgerhartstraat 25, 1055 KV Amsterdam, The Netherlands.

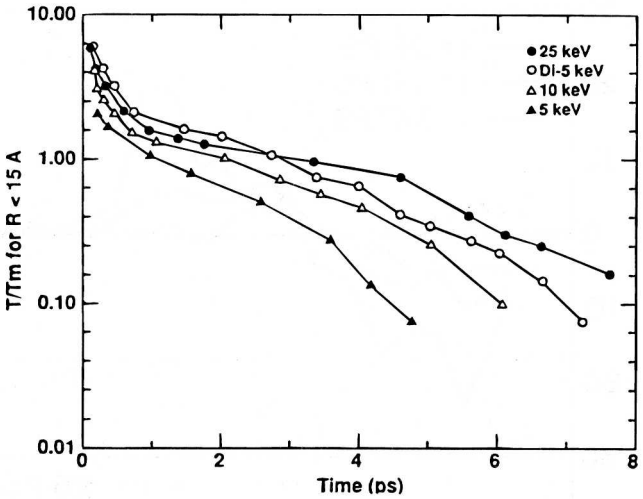

FIG. 25. Cooling rate at the center of cascades in Cu as a function of recoil energy. The ambient temperature was 10 K. (After Ref. 81.)

remains above the melting temperature, obeys the relation, $\tau_{sp}(\text{ps}) \approx 0.2E_D$ (keV), illustrating that τ_{sp} varies nearly linearly with recoil energy and that the spike persists for several lattice vibrations for cascades with energies greater than ≈ 1 keV. For comparison, the solution to the heat equation yields $\tau_{sp} \propto (E_D)^{2/3}$, assuming that the initial energy distribution is a small sphere, and $\tau_{sp} \propto E_D$ assuming that it is a cylinder. The average thermal diffusivity of Cu deduced from these cooling rates is $\approx 2.5 \times 10^{12}$ nm^2/s.

The transition in the cascade dynamics from ballistic to thermal spike phases has been examined by following the energy distribution of the atoms in the cascade region. Since the cascade shape is irregular, identifying the cascade volume in MD has often been imprecise and misleading. A convenient method for MD is suggested by the snapshots in Figs 21 and 23, where the melt zone is readily identified by its instantaneous structure, without the need for time averaging. The structural order parameter of the kth atom, $P_{st}(k)$, was thus defined by its angular coordination with its neighbors, that is,

$$P_{st}(k) = \frac{\left\{\sum_i^N [\theta_k(i) - \theta_k^p(i)]^2\right\}^{1/2}}{p_u(k)} \tag{7.1}$$

where $\theta_k(i)$ is the ith smallest angle formed with atom k at the vertex and two nearest-neighbor atoms, $\theta_k^p(i)$ is the same quantity for the perfect lattice,

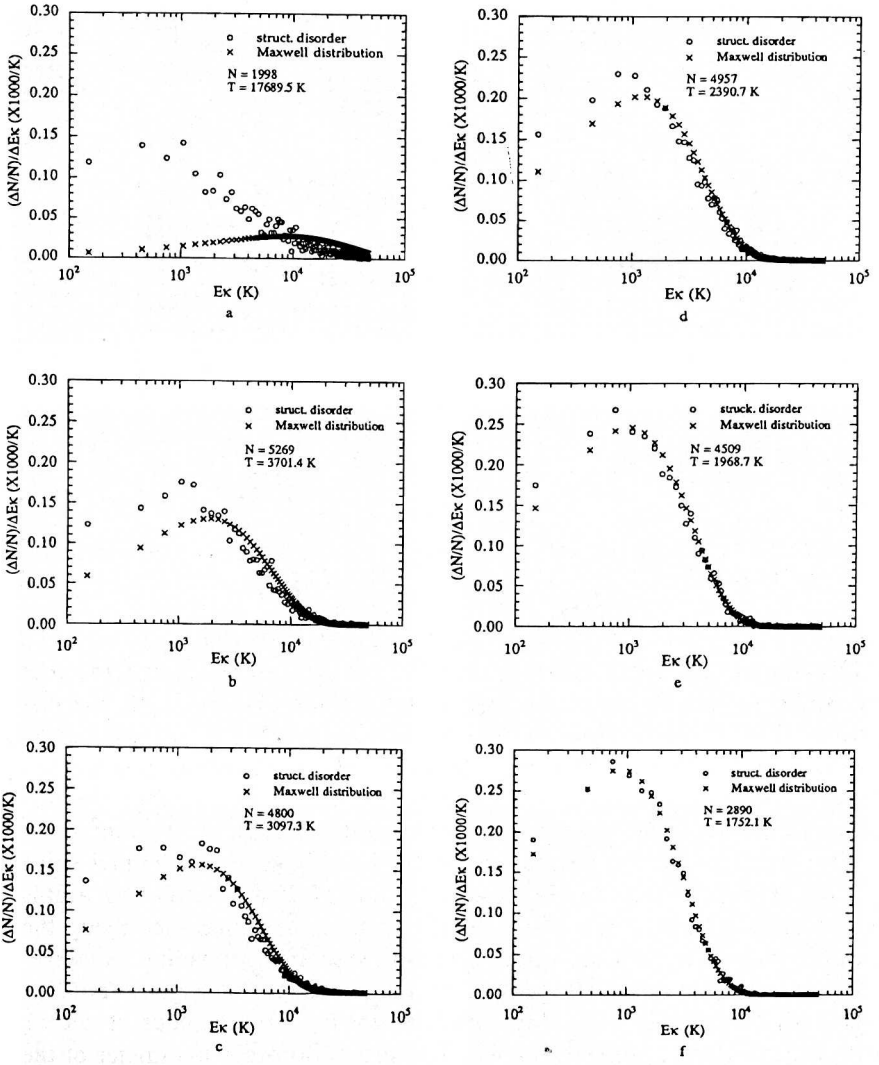

FIG. 26. Distribution of kinetic energies of atoms in the local melt during the evolution of a 10-keV cascade in β-NiAl showing the approach to local equilibrium. N is the number of atoms in the melt. (After Ref. 60.)

and $p_u(k)$ is a normalization constant.[60] The sum is over the set of all possible angles. By calculating the range of values of $P_{st}(k)$ for atoms in a liquid, the criterion for identifying liquid atoms in the cascade volume was obtained. Thermalization of a 10-keV cascade in β-NiAl was examined using this procedure. In Fig. 26 kinetic energy distributions of atoms in the

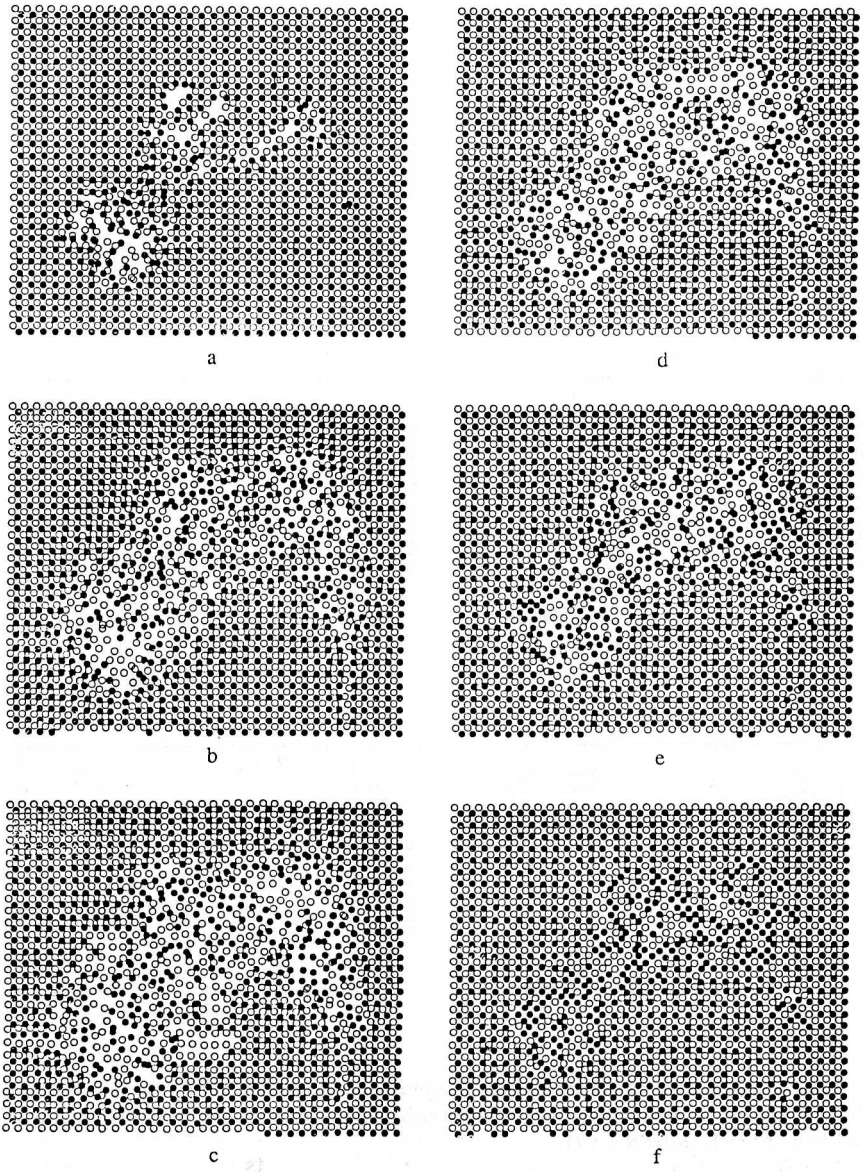

FIG. 27. Cross-sectional view of atoms in a slab of thickness a_0 through the center of a 10-keV cascade in β-NiAl at various instants of time. N is the number of atoms in the melt. (After Ref. 60.)

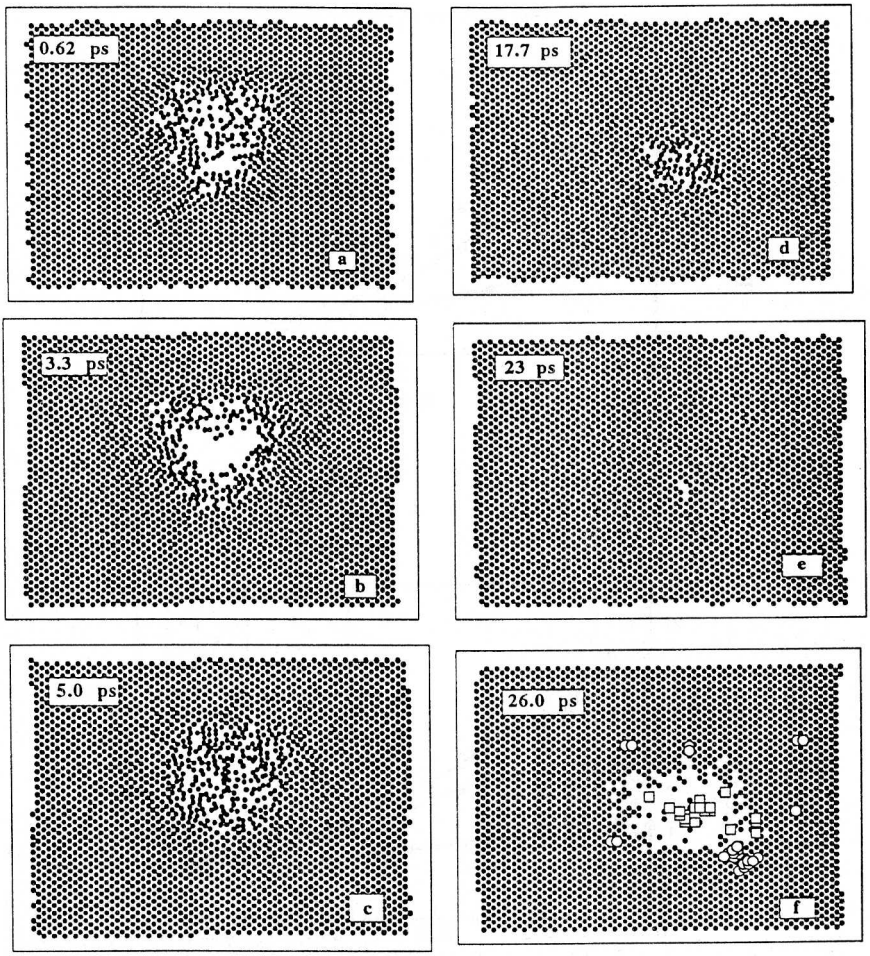

FIG. 28. Cross-sectional view of atoms in a slab of thickness $a_0/2$ through the center of a 10-keV cascade in Au at various instants of time. (After Ref. 82.)

melt zone are shown at different instants of times. As expected, the distribution becomes Maxwellian at ≈ 0.4 ps, which corresponds to a few lattice vibrations. Figure 26 also illustrates that the size of the cascade reaches its maximum value at about this same time. Snapshots of the atom locations are shown in Fig. 27 for this same cascade to illustrate how the structure of the cascade develops during thermal equilibration.

The thermal spike effects discussed for Cu and β-NiAl are more prominent in materials with large atomic numbers and low cohesive energies, owing to the greater localization of energy in the cascade core, lower

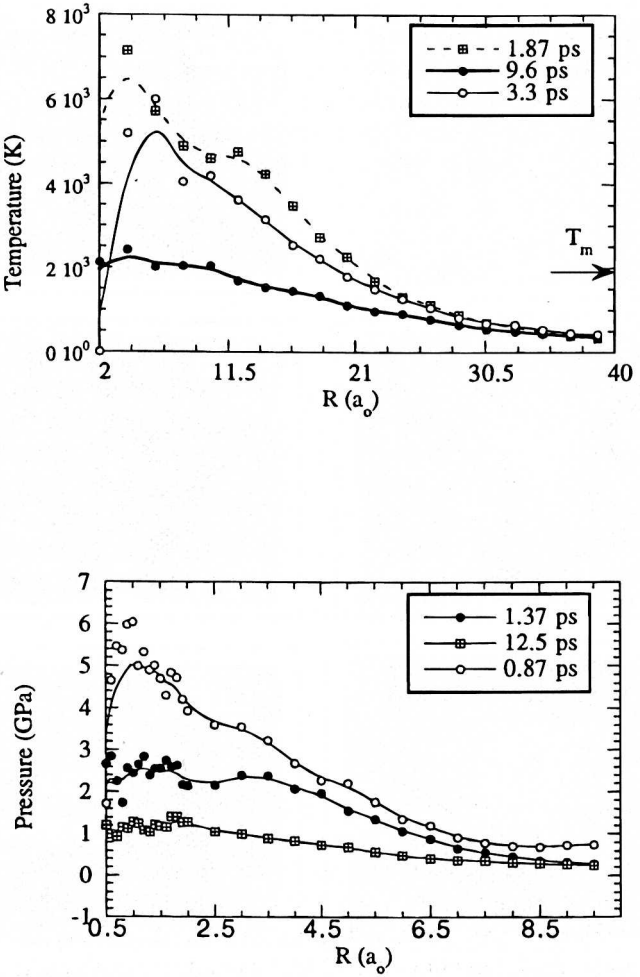

FIG. 29. (a) Temperature and (b) hydrostatic pressure in a 10-keV cascade in Au plotted as a function of distance from the center of energy. (After Ref. 82.)

melting temperature, and softer surrounding medium. For example, the evolution of a 10-keV cascade in Au is shown in Fig. 28. In this case, extensive cavitation is clearly observed.[82] The high temperatures and pressures associated with this event are plotted in Fig. 29a and b. The temperature at the center of the cascade reaches $\approx 6T_m$, while the pressure is ≈ 8 GPa. For comparison, the shear modulus of Au is ≈ 28 GPa, which raises the possibility of local plastic deformation. Although it was not observed in this

[82] M. Ghaly and R. S. Averback, *Nucl. Instrum. Methods B*, in press.

particular event, evidence for plastic deformation has recently been found in a 30-keV MD event in Au.[83] The comparison between 10-keV events in β-NiAl and Au illustrates that the details of cascade dynamics in cascades vary greatly from one material to another, depending on their cohesive properties. Melting, however, appears to be a rather general feature.

V. Ion-Beam Mixing

Ion-beam mixing refers to the relocation of atoms in cascades during irradiation. It is a topic of considerable practical interest since it is important for predicting phase stability in reactor components and for synthesizing new materials by ion implantation. For example, mixing a thin film with its underlying substrate by low-temperature irradiation can often lead to metastable phases since thermally activated diffusion is suppressed. From a fundamental point of view, measurements of ion-beam mixing are enormously useful for understanding displacement processes in irradiated materials since they provide a direct measure of the number of atoms that are relocated in a cascade and the distances they move.

8. Phenomenological Models

a. *BCA Models*

The magnitude of ion-beam mixing can be estimated within BCA models by assuming that mixing occurs as part of the defect production process. Specifically, if ν Frenkel pairs are produced in a cascade with damage energy E_D, and s replacement events are involved in the creation of each displacement (Frenkel pair), then using the Kinchin–Pease expression for ν, the mean-square displacement of atoms in a cascade is obtained as

$$\langle R^2 \rangle = \frac{0.8 E_D s \lambda^2}{2E_d}, \tag{8.1}$$

where λ is the replacement distance. A more useful form of Eq. (8.1) is obtained by normalizing $\langle R^2 \rangle$ by the damage energy deposited in the sample, that is, $E_D = F_D \Phi V = F_D \Phi N / N_0$, where F_D is the energy deposition per unit length normal to an irradiated surface, Φ the ion fluence, N the number of atoms in the sample, and $V(=N/N_0)$ is the volume of the

[83] T. Diaz de la Rubia, unpublished.

sample. Thus the mean-square displacement per atom, $\langle R_a^2 \rangle$, normalized by the damage energy per unit volume is given by

$$\xi_{\text{IM}} = \frac{\langle R_a^2 \rangle}{\Phi F_D} = \frac{0.8 s \lambda^2}{2 N_0 E_d}, \tag{8.2}$$

where ξ_{IM} is called the mixing parameter. A value of $s \approx 5$ yields $\langle R_a^2 \rangle \approx 10$ Å^5/eV. Boltzmann transport theory provides a more rigorous treatment of ion-beam mixing but about the same result. Sigmund and Gras-Marti, for example, obtained the expression[84]

$$\frac{\langle R_a^2 \rangle}{\Phi F_D} = \frac{\Gamma_0 \zeta_{21} \lambda_c^2}{3 N_0 E_c}, \tag{8.3}$$

where Γ_0 is a dimensionless constant ($=0.608$), $\xi_{21} = 4(m_1 m_2)/(m_1 + m_2)^2$, E_c is the minimum energy for atomic displacements, and λ_c is the mean range of a target atom with energy E_c. Equations (8.2) and (8.3) both predict that the mixing parameter is independent of damage energy, has only little variation between different materials, and has a magnitude of ≈ 10 Å^5/eV.

Computers simulations based on BCA models have also been employed to treat ion-beam mixing.[85] These simulations, which are usually based on TRIM (i.e., amorphous targets), operate as described in Section 3c. For simulations of mixing, however, the target atoms are "relaxed" after the passage of an ion through the material to maintain constant density. (This step is unnecessary if recombination of interstitals and vacancies is allowed.) Several trajectories are run to provide adequate statistics. The BCA simulations predict approximately the same magnitude of mixing as transport theory, although a direct comparison is difficult, owing to the different parameter sets employed in the calculations. The simulations also find linear scaling between $\langle R_a^2 \rangle$ and damage energy per atom.

b. *Thermal Spike Models*

Seitz and Koehler,[1] and later Vineyard,[86] considered whether thermally activated atomic transitions such as diffusion and desorption could take place during the brief lifetime of a thermal spike. The number of these tran-

[84] P. Sigmund and A. Gras-Marti, *Nucl. Instrum. Methods B* **182/183**, 25 (1981).
[85] W. Möller and W. Eckstein, *Nucl. Instrum. Methods B* **7/8**, 645 (1985).
[86] G. H. Vineyard, *Radiat. Eff.* **29**, 245 (1976).

sitions was calculated in the Vineyard model using the expression

$$\eta = \int \mathrm{d}^3 r \int A \exp\left[\frac{-Q}{kT(r,\, t)}\right] \mathrm{d}t, \tag{8.4}$$

where the transition rate per unit volume of lattice is $R = A \exp(-Q/k_B T)$, and Q is the appropriate activation energy. With the assumptions of temperature-independent thermal conductivity κ and specific heat C, and a deposition of energy represented by either a point $[\varepsilon = \varepsilon_0 \delta(r)]$ or a line $[\lambda = \lambda_0 \delta(\rho)]$ source, Vineyard obtained

$$\eta_c = \frac{A\lambda_0^2}{8\pi C \kappa Q^2} \tag{8.5}$$

for cylindrical spikes, and

$$\eta_{\mathrm{sp}} = \frac{0.02226 A \varepsilon_0^{5/3}}{C^{2/3} \kappa Q^{5/3}} \tag{8.6}$$

for spherical spikes. This formalism is readily adapted to ion-beam mixing. For the geometry of tracer diffusion experiments, for example, the profile broadening, $\langle \Delta x^2 \rangle$, is given by[30]

$$\langle \Delta x^2 \rangle = 2\Phi \int_{P=0}^{E} \mathrm{d}P \, \frac{\mathrm{d}\sigma(P,\, E)}{\mathrm{d}P} \int_0^{\infty} \mathrm{d}t \; n_0 \, v_d(t) D(t), \tag{8.7}$$

where $v_d(t)$ is the volume of the cascade at time t, and $D(t)$ is the diffusion coefficient of atoms in the cascade. For solids, the inner integral corresponds to either Eq. (8.5) or (8.6) but weighted by the square of the jump distance. The outer integral averages over the primary recoil spectrum.

Johnson and co-workers modified the Vineyard expression for cylindrical spikes to include thermodynamic driving forces through the Darken equation.[87] For regular alloy solutions, Eq. (8.5) becomes

$$\eta = \frac{A\lambda_0^2}{8\pi C \kappa Q^2} \left(1 - \frac{2\, \Delta H_m}{k_B T}\right), \tag{8.8}$$

[87] W. L. Johnson, Y. T. Cheng, M. Van Rossum, and M.-A. Nicolet, *Nucl. Instrum. Methods B* **7/8**, 657 (1985).

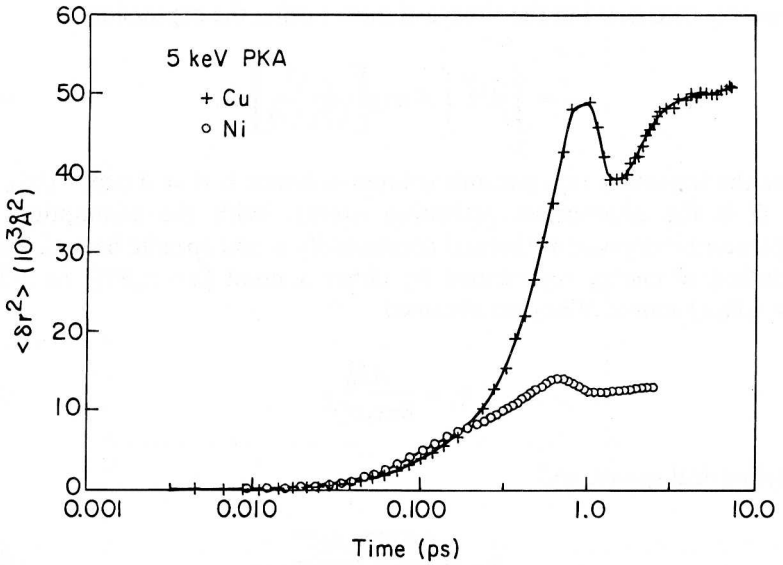

FIG. 30. Mean-square displacements of atoms in 5-keV cascades as a function of time for Cu and Ni. (After Ref. 88.)

where ΔH_m is the heat of mixing. Since Q is related to the activation energy for diffusion, Johnson *et al.* associated it with the cohesive energy of the material. The important contribution of Eq. (8.8) is that it relates ion-beam mixing to the thermodynamic quantities, Q and ΔH_m, and thus provides a means to distinguish ballistic mixing experimentally from thermal spike mixing.

9. MD SIMULATIONS OF ION-BEAM MIXING

a. *Pure Metals*

The mixing is calculated in MD simulations by summing the mean-square displacements of all atoms in the cell following a cascade event. It can be related to the experimental mixing parameter through the relation

$$\xi_{\text{IM}} = \frac{\langle R_a^2 \rangle}{\Phi F_D} = \frac{\langle R^2 \rangle}{N_0 E_c}, \tag{9.1}$$

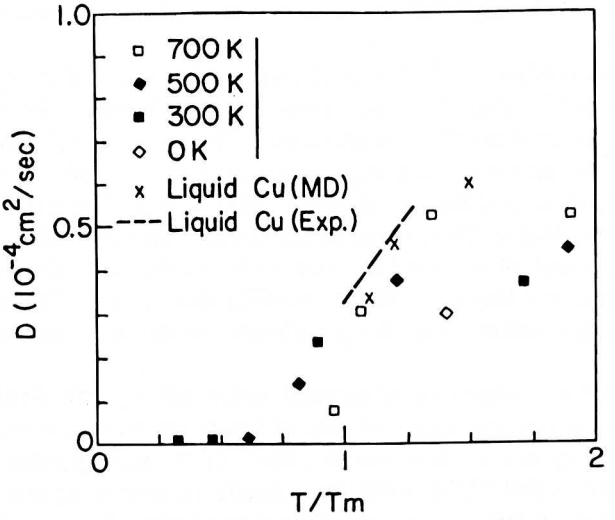

FIG. 31. Diffusion coefficients of atoms in the core of a 3-keV cascade in Cu, in liquid "MD" Cu, and in liquid Cu as a function of temperature. (After Ref. 80.)

where E_c is the cascade energy and $\langle R^2 \rangle$ is the mean-square displacement of all atoms in the simulation cell:

$$\langle R^2 \rangle = \sum_{i=1}^{N} [\mathbf{r}_i(t) - \mathbf{r}_i(t=0)]^2, \tag{9.2}$$

where $\mathbf{r}_i(t)$ is the position vector of atom 'i' at time t. Mixing is shown for Cu and Ni in Fig. 30 as a function of time following the initiation of 5-keV cascade events.[88] The results illustrate that mixing in Cu is approximately three times larger than in Ni. More significantly, these simulations provide the time evolution of mixing, which makes it possible to examine how the mixing takes place. Cu and Ni have been compared here since these metals have nearly the same atomic number and very similar displacement energies but different melting temperatures. Ballistic mixing should therefore be nearly the same for the two but not the thermal spike mixing. At short times, when ballistic mixing dominates, the mixing is indeed observed to be the same, while after 0.2 ps, when the thermal spike phase becomes important, a substantial difference is found. The peak in the mixing curve for Cu

[88] T. Diaz de la Rubia, R. S. Averback, H. Hsieh, and R. Benedek, *J. Mater. Res.* **4**, 579 (1989).

arises from the reversible lattice expansion around the hot melt but is not of interest here.

Additional studies on Cu compared the mixing in the thermal spike with liquid diffusion.[80] This study was performed by initiating 3-keV events in Cu held at different ambient temperatures. The results are shown in Fig. 31. Except for the points at very high temperatures, agreement between diffusion in the cascades, diffusion in liquid "MD" Cu, and experimental values of diffusion in liquid Cu is remarkably good. This study also showed that the total amount of mixing increases with increasing lattice temperature, being a factor of 4 larger at 700 K ($\approx 0.6T_m$) than at 0 K. This is consistent with the larger volume and longer lifetime of the melt at elevated temperatures.

Although the association of thermal spike mixing with liquid diffusion provides a concise, conceptual picture of ion-beam mixing, it would be misleading to carry this analogy too far. Most of the mixing takes place early in the thermal spike phase while the cascade volume is rapidly expanding. Figure 32, for example, shows the time dependence of mixing in a 10-keV cascade in Au; this should be compared with the structure of the cascade zone shown in Fig. 28. The mixing is nearly complete by ≈ 7 ps, while the cross sections in Fig. 28 illustrate that complete solidification does not occur until much later. It is also observed in these figures that most of the mixing occurs while extensive cavitation is still present in the cascade. Although Au represents an extreme example of cavitation, a similar relationship between mixing rate and local density was observed in β-NiAl.[60] All of the mixing in this alloy occurred in a region where the relative density was less than ≈ 0.85. Although this is appreciably higher than the density in the Au cascade, it is significantly less than the density of a

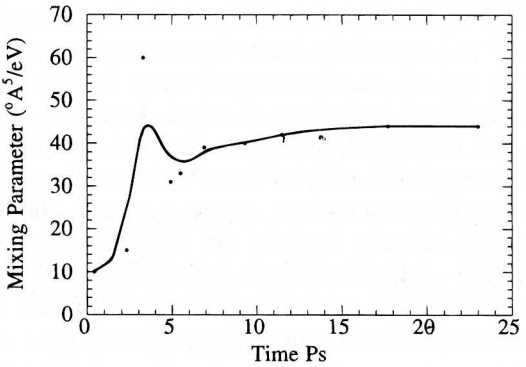

FIG. 32. Mean-square displacements of atoms as a function of time in a 10-keV cascade in Au. (After Ref. 82.)

homogeneous liquid. In accordance with their relative changes in local density, the mixing in the β-NiAl cascade was nearly 10 times smaller than that in Au.

The fraction of atoms that move in a cascade and the distance that they move are important quantities for understanding phase stability in irradiated materials.[89] These fractions have been found for 10-keV cascades in Ni[90] and β-NiAl.[60] Although mixing is relatively small in these metals, the fraction of relocated atoms is nevertheless large; for Ni the fraction is ≈ 0.50, and for β-NiAl it is ≈ 0.35, which indicate nearly all the atoms in the hotter, less dense regions of the cascade have relocated. The distributions for the relocation distances in these same two cascades are plotted in Fig. 33. Most relocated atoms are found on the nearest-neighbor sites in Ni, showing that most atoms undergo just one jump during the spike. In β-NiAl, relocation to the first and second nearest-neighbor sites is nearly equal. This difference between the two metals is apparently due to effects of chemical ordering, since relocation to a first nearest-neighbor site creates an antisite defect in the CsCl structure of β-NiAl. The figure also shows that

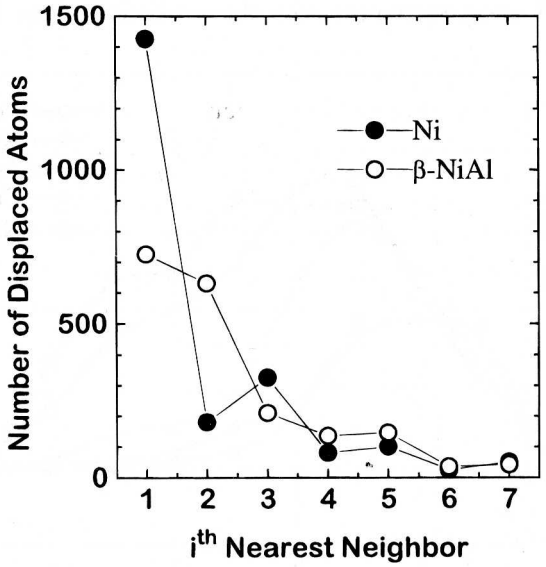

FIG. 33. Distribution of relocation distances, measured by neighbor site location, for atoms in the cascade core of 10-keV events in Ni and β-NiAl. (After Refs. 60 and 90.)

[89] G. Martin and P. Bellon, *Solid State Physics*, Vol. 50, ed. H. Ehrenreich and F. Spaepen, Academic Press, New York (1996), p. 307.

[90] H. Zhu, M. K. Nordlund, and R. S. Averback, unpublished result.

some atoms move quite far. These include the 10-keV PKA and other high-energy recoils. The relative contributions to the mixing from atoms that have moved a distance x_i during the cascade have been determined for these and other metals as shown in Fig. 34. Plotted here is the fractional mixing F_i,

$$F_i = \frac{f_i x_i^2}{\sum_j f_j x_j^2}, \tag{9.3}$$

where f_i is the fraction of atoms that are displaced a distance x_i. These two figures, Figs. 33 and 34, illustrate that nearly all atoms in the cascade undergo at least one jump and that in energetically denser cascades, a large fraction of them undergo two or three jumps.

MD simulations have also been employed to examine the influence of thermodynamic factors on ion-beam mixing. Gades and Urbassek, for example, parametrized their interatomic potentials to adjust the heat of solution and cohesive energy independently to test Eq. (8.8).[91] These authors found good agreement with the prediction of an inverse-square

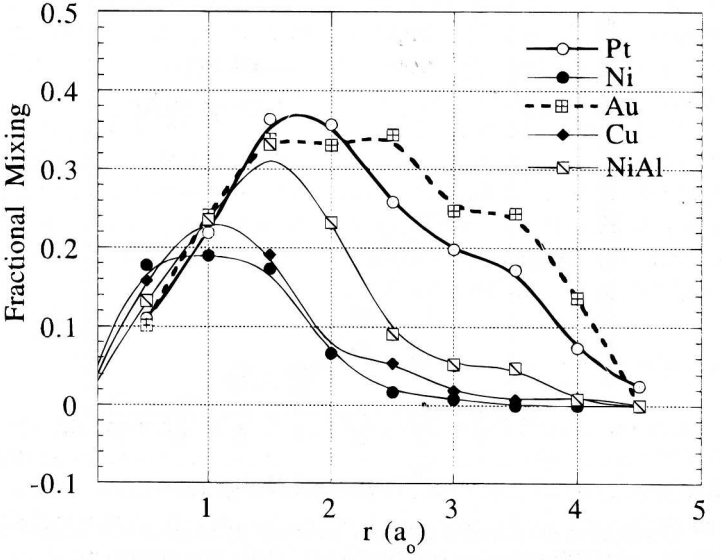

FIG. 34. Fractional contributions to the mixing as a function of the relocation distance of the atoms. (After Ref. 90.)

[91] H. Gades and H. M. Urbassek, *Phys. Rev. B* **51**, 14559 (1995).

dependence on cohesive energy. For the dependence on the heat of solution, they found the same trend as Eq. (8.8) but not the linear relationship. Since these simulations were performed using rather low cascade energies, 1 keV, better agreement should probably not be expected, since the thermal spike mixing may not greatly exceed ballistic mixing and only the former is included in the phenomenological model.

b. *MD Simulations of Mixing and Disordering in Order–Disorder Alloys*

Chemical disordering and mixing in order–disorder alloys have been investigated by MD simulations of cascades in Cu_3Au,[92] β-NiAl,[60] and Ni_3Al.[93] These simulations have examined the number of antisite defects created in the cascade, the mixing parameter, and the change in the LRO parameter, S, and the short-range-order parameter, q. The determination of the order parameters, however, is imprecise since the concentration of antisite defects in the cascade is needed, not just the number of them, and this requires the cascade volume. For β-NiAl, for which the cascade volume was determined by Eq. (7.1), two regions of short-range disorder were found; one was highly disordered with a value of $q = 0.2$, and the other region was only slightly disordered, $q = 0.8$. The evolution of this cascade undergoing disordering is illustrated in Fig. 27. Here the highly disordered region in the center of the cascade is clearly evident. It is noteworthy that this region, seen in Fig. 27f, is significantly smaller than the once-melted volume, Fig. 27c. This illustrates that melting (structured disordering) is a more rapid process than mixing (chemical disordering) and that the melt cannot equilibrate, even on a local level (i.e., the liquid does not uniformly disorder). Only in the central core region of low density is mixing sufficiently rapid to cause disordering. The simulations have also shown that mixing on the two sublattices is the same despite the different masses on each.

10. Experimental Results

A vast literature on ion-beam mixing in all classes of hard materials is now available.[94] Three types of mixing experiments are common: tracer diffusion, chemical interdiffusion, and chemical disordering of order–disorder alloys. The two diffusion experiments are performed similarly to thermal diffusion experiments, although due to sputtering, the tracer atoms must be buried

[92] T. Diaz de la Rubia, A. Caro, and M. Spaczer, *Phys. Rev. B* **47**, 11483 (1993).
[93] F. Gao and D. J. Bacon, *Philos. Mag. A* **71**, 65 (1995).
[94] See, e.g., B. M. Paine and R. S. Averback, *Nucl. Instrum. Methods B* **7/8**, 666 (1985).

below the surface. The spatial resolution in these experiments is typically ≈ 10 nm. Since the mean-square displacement of most atoms in the cascade is less than ≈ 0.5 nm, ion doses of several dpa (i.e., several cascade overlaps) are required in these experiments. Thus mixing experiments are performed in heavily damaged materials. This experimental limitation has important consequences for studies at high temperatures when defects are mobile, as discussed in Section IX, but it is probably not a significant source of error at low temperature. The lengths of RSCs, however, might be affected by the damage for the reasons discussed earlier. Measurements of disordering rates in order–disorder alloys are limited to a small number of systems, but they provide the sensitivity to probe the mixing within individual cascades using such techniques as electrical resistivity or magnetization. The relationship between ion-beam mixing and disordering rates, however, is model dependent, complicating comparison between the two types of experiments.

a. *Measurements of Tracer Diffusion*

The results of tracer diffusion experiments are tabulated in Tables 3 and 4 for several metals and semiconductors. The mixing parameters refer to tracer diffusion of impurities rather than to self-diffusion. For most metals the mixing parameters are not very sensitive to the type of tracer impurity, although differences are measurable. Correlations, for example, between the mixing parameter, ξ_{IM}, for different tracer impurity atoms and thermal tracer impurity diffusion coefficients have been noted.[95,96] Large variations in ξ_{IM} are observed in Si and Ge for different tracer atoms. Mixing of W atoms in amorphous Si yields $\xi_{IM} = 144$ Å^5/eV, whereas mixing of Au

TABLE 3. ION BEAM MIXING PARAMETERS IN SELECTED METALS

	Ag	Al	Au	Cu	Er	Fe	Ni	Mo	Pt	Ti	W	CuEr	NiTi
ξ_{IM}	550	120	720	135	115	38	50	45	114	25	66	360	7
T_m	961	660	1063	1083	1795	1536	1453	2610	1769	1668	3410		
Z	47	13	79	29	68	26	28	42	78	22	74	29/68	28/22

Source: Data for crystalline metals from B. M. Paine and R. S. Averback, *Nucl. Instrum. Methods B* **7/8**, 666 (1985); data for amorphous alloys and Er from R. S. Averback and D. N. Seidman, *Mater. Sci. Forum* **15/18**, 963 (1987).

[95] S. J. Kim, M.-A. Nicolet, R. S. Averback, and D. Peak, *Phys. Rev. B* **37**, 38 (1988).
[96] E. Ma, S.-J. Kum, M.-A. Nicolet, and R. S. Averback, *J. Appl. Phys.* **63**, 2449 (1988).

TABLE 4. ION-BEAM MIXING PARAMETERS IN SELECTED SEMICONDUCTORS

MATRIX	AlAs[a]	GaAs[a]	Ge[b]	InP[a]	Si[b]
Marker	Ga	Al	Si	(As, Ga)	Ge
ξ	144	720	570	$\approx$1200	480

[a] Data from D. V. Forbes, J. J. Coleman, J. L. Klatt, and R. S. Averback, *J. Appl. Phys.* **77**, 3543 (1995).

[b] Data from B. M. Paine and R. S. Averback, *Nucl. Instrum. Methods B* **7/8**, 666 (1985).

atoms yields $\xi_{IM} = 700$ Å^5/eV.[94] Since Si and Ge are mutually soluble, tracers of one in the other probably best represent self-atom mixing, so these values were included in the table. Irradiation of both Si and Ge render them amorphous, so their mixing parameters refer to the amorphous structure. The significant trends in these data are:

1. The magnitude of the mixing parameter in both metals and semiconductors is greater than that predicted by the models of ballistic mixing, in some cases by nearly a factor of 100.

2. The mixing parameter in metals increases as a function of both atomic number and decreasing melting temperature.

3. The mixing parameter varies somewhat for different tracer impurity atoms in the same matrix, appearing to be correlated with thermal diffusion coefficients.

4. The mixing parameter is as large or larger in amorphous metallic alloys than in their pure, crystalline alloy components. Although not shown in the table, mixing in $Ga_xAl_{1-x}As$ and InP compounds was found to be larger when these compounds were amorphous rather than crystalline.[97] The mixing parameters in the semiconductors, moreover, are generally larger than those in metals.

5. The mixing parameter in metals correlates inversely with the power loss from electron–phonon coupling [Eq. (4.4)].[98–100]

Since most of the data in Tables 3 and 4 were obtained during irradiation at 6 or 80 K and analyzed by Rutherford backscattering at the irradiation

[97] D. V. Forbes, J. J. Coleman, J. L. Klatt, and R. S. Averback, *J. Appl. Phys.* **77**, 3543 (1995).
[98] K. Tappin, I. M. Robertson, and M. A. Kirk, *Philos. Mag. A* **70**, 463 (1994).
[99] I. Koponen, *J. Appl. Phys.* **72**, 1194 (1992).
[100] J. L. Klatt, R. S. Averback, and D. Peak, *Appl. Phys. Lett.* **55**, 1295 (1989).

temperature, they should not be affected by thermally activated diffusion processes. The trends seen in the marker mixing have no explanation within the BCA model. The magnitude of the mixing, moreover, is too large for ballistic mixing except, perhaps, in the more refractory metals with low atomic number. On the other hand, all the data fit rather well with the qualitative predictions of phenomenological models of thermal spike mixing. Quantitative comparisons, however, are more difficult to make, owing to the various unknown parameters in these models, but it does deserve mention, for the sake of plausibility, that estimates of mixing using Eq. (8.7) and assuming liquid diffusion in the cascades do agree with experiments.[95] The correlation between electron–phonon coupling and mixing is intriguing but tenuous, since the e-p coupling could not be varied while other parameters were held fixed. Unfortunately, those metals for which electron–phonon effects should be largest are also metals that have high melting temperatures. Despite this difficulty, Koponen performed calculations of ion-beam mixing, in the framework of Eq. (8.7), and showed that inclusion of e-p coupling in the model improved the agreement with experiments. More definitive evidence is needed, however, to establish how significantly e-p coupling influences mixing.

The large mixing parameters in semiconductors relative to those in metals of comparable atomic numbers and melting points are not yet explained. Since the semiconductors were in an amorphous state during mixing, some enhanced thermal spike mixing might be expected in these materials, owing to their lower thermal diffusivities. Indeed, the amorphous metals show enhanced mixing, but this appears to be only a small effect. An alternative explanation attributes enhanced mixing in semiconductors to stimulated diffusion by electronic excitation. Since the mixing parameters in Si are not sensitive to the mass and energy of the irradiation particles,[101] and therefore independent of electronic stopping power, this explanation is not likely to be correct. The large mixing parameters in semiconductor, therefore remains unexplained.

b. *Measurements of Chemical Interdiffusion*

The influence of thermodynamic driving forces on ion-beam mixing was first investigated by Cheng *et al.*,[102] who compared the mixing in a series of bilayer samples, one layer being either Au or Pt and the other being a 3*d* transition metal. Within this series, the heat of mixing varied significantly

[101] M.-A. Nicolet, T. C. Banwell, and B. M. Paine, *Mater Res. Soc. Symp. Proc.* **27**, 3 (1984).
[102] Y. T. Cheng, M. Van Rossum, M.-A. Nicolet, and W. L. Johnson, *Appl. Phys. Lett.* **45**, 185 (1984).

while other parameters were nearly constant. The results of these experiments are shown in Fig. 35 where the mixing is plotted as a function of ΔH_m. Although there is considerable scatter in the data, the trend seems unmistakable. These general results, moreover, have been confirmed using similar measurements on other systems.[103,104] The slope in the mixing versus $-\Delta H_m$ curve is predicted by Eq. (8.8) to be proportional to the cascade temperature, and from which a cascade temperature of 10^4 K was deduced. Although the analysis is very approximate, the magnitude of the temperature obtained appears physically plausible. The temperature found by MD simulation in a 10-keV cascade in pure Au, for example, was $\approx$8000 K (see Fig. 29).

Several investigations have focused on mixing in systems with positive heats of mixing.[105–107] Mixing in these systems should be reduced by the

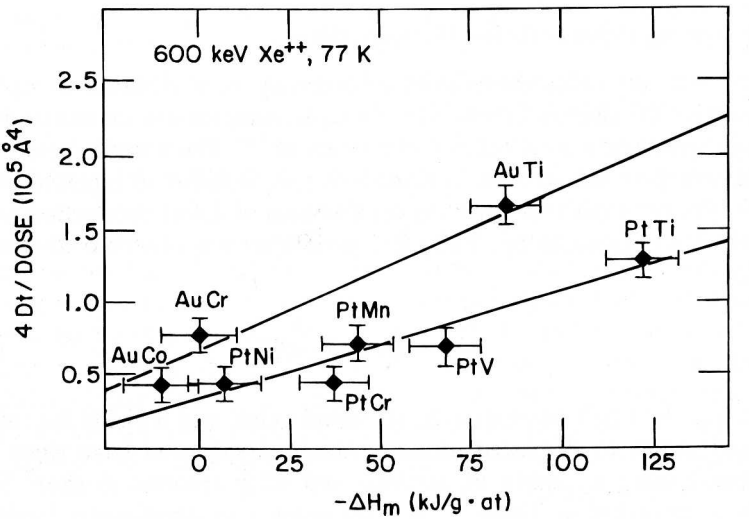

FIG. 35. Amount of ion-beam mixing as a function of the heat of mixing in for a series of Au and Pt diffusion couples. (After Ref. 102.)

[103] T. A. Workman, Y. T. Cheng, W. L. Johnson, and M.-A. Nicolet, *Appl. Phys. Lett.* **50**, 1486 (1987).
[104] W. Boise, *Mater. Sci. Eng. R* **12**, 53 (1994).
[105] Z. L. Qang, J. F. M. Westerdorp, and F. W. Saris, *Nucl. Instrum., Methods B* **209/210**, 115 (1983).
[106] R. S. Averback, D. Peak, and L. J. Thompson, *Appl. Phys. A* **39**, 59 (1986).
[107] A. Crespo-Sosa, P. Schaaf, W. Boise, and K.-P. Lieb, *Phys. Rev. B* **53**, 14795 (1996).

thermodynamic factor, and when $2\Delta H_m > 1$ it should be completely suppressed. Typically, these are systems that form immiscible liquids. This prediction has been firmly established in Fe–Ag.[107] This result also clarifies the relative importance of ballistic and thermal spike processes. Ballistic mixing involves recoils that should not be much influenced by the chemical driving forces. Since mixing is completely suppressed in some systems, any ballistic mixing that occurs early in the cascade evolution must be reversed during the subsequent thermal spike.[106] The lack of mixing in Fe–Ag, therefore, indicates that mixing in the thermal spike in this system must far exceed the ballistic component of mixing. The possibility of phase separation in cascades of highly immiscible systems was tested by irradiating an alloy sample of CuMo. The sample was prepared by physical vapor deposition at a temperature too low to allow thermal diffusion. Subsequent irradiation at 80 K led to nearly complete phase separation into the pure alloy components.[108]

c. *Disordering Rates of Order–Disorder Alloys*

Experiments on radiation-induced disordering were reported as early as 1949, where the electrical resistivity of Cu_3Au samples was measured during neutron irradiation in a reactor environment.[109] These early experiments had shown that the amount of disordering, or number of replaced atoms, was far greater than that expected on the basis of defect production i.e, the number of displaced atoms. The LRO parameter was observed to obey the relation[110]

$$S(\Phi) = S_0 \exp(-\alpha\Phi) \tag{10.1}$$

where S is the LRO parameter, S_0 its initial value, and α yields the ratio of replaced atoms to displaced atoms.† Many experiments have since been performed using a variety of particles and alloy systems. A short list of results is provided in Table 5. In most cases α is significantly larger for mixing produced by cascades than by electron irradiation. At one time the large ratio of replacements to displacements in Cu_3Au was cited as evidence for long-range replacement sequences; however, the greater importance of thermal spikes in this alloy has proven this conjecture incorrect. Nevertheless, the large RCS lengths reported in W and Ni_3Mn should influence the

[108] L. Wei and R. S. Averback, unpublished result.
[109] S. Siegel, *Phys. Rev.* **75**, 1823 (1949).
[110] L. R. Aronin, *J. Appl. Phys.* **25**, 344 (1954).
† α only equals this ratio in a random model of disordering and when Φ is measured in dpa.

TABLE 5. DISORDERING PARAMETER α

	Cu_3Au	CuPd	FeCo	Ni_3Mn	Zr_3Al	Ni_3Al
MeV e^-	1[a]	3.1[b]	32[c]	4[d]	2[e]	4
Thermal n	20[f]			24[g]		
1 MeV He	22[h]					
Fast n	60[i]	24[b]	90[c]	16[i]	10[j]	

[a] From M. Z. Hammed, R. E. Smallman, and M. H. Loretto, *Philos. Mag. A* **46**, 707 (1982).

[b] From R. H. Zee, M. W. Guinan, and G. L. Kulcinski, *J. Nucl. Mater.* **114**, 190 (1983).

[c] From J. P. Riviere and J. F. Dinhut, *J. Nucl. Mater* **118**, 333 (1983).

[d] From D. Becker, F. Dworschak, C. Lehmann, K. T. Rie, H. Schuster, H. Wollenberger, and J. Wurm, *Phys. Stat. Solidi A* **81**, 145 (1968).

[e] From E. M. Schulson, *J. Nucl. Mater.* **83**, 239 (1979).

[f] From R. Zee and P. Wilks, *Philos. Mag. A* **42**, 463 (1980).

[g] From M. A. Kirk, T. H. Blewitt, and T. L. Scott, *Phys. Rev. B* **15**, 2914 (1977).

[h] From M. Ghaly, Y. S. Lee, R. S. Averback, and C. P. Flynn, unpublished result.

[i] From M. A. Kirk and T. H. Blewitt, *Metall. Trans* **9a**, 1729 (1978).

[j] From L. M. Howe and M. H. Rainville, *Philos. Mag. A* **39**, 195 (1979).

mixing. For example, if the value of s in Eq. (8.1) were changed from 5 to 30, the experimental mixing parameter in W could then be explained largely by RCSs.

Mixing experiments do not distinguish between RCSs and random atomic motion. Moreover, since mixing experiments are performed at high doses, the lengths of RCSs could be reduced severely, owing to large accumulations of damage, as mentioned above. The disordering experiments of Kirk *et al.* discussed in Section 6c for thermal neutrons, therefore, in principle provide a means to examine RCSs produced in cascades, as they distinguish $\langle 110 \rangle$ replacements from random disordering and can be performed at very low doses. As pointed out in Section 6c, low-energy recoils typical of thermal neutrons (450 eV in Ni_3Mn) result in long replacement sequences ($\approx$22 replacements per displacement). Kirk and Blewitt repeated their experiments but with fast neutron irradiation for which energetic cascades are produced ($T_{1/2} \approx 30$ keV), and a far different result was obtained.[111] Their computer modeling of the magnetization, using the theory of Marcinkowski, indicated that for fast neutrons, disordering was due entirely to random replacements of atoms. A maximum contribution to

[111] M. A. Kirk and T. H. Blewitt, *Metall. Trans.* **9a**, 1729 (1978).

the disordering from ⟨110⟩ replacement sequences was 4%. They further deduced a value of 16 replacements per displacement from these experiments.

These results for fast neutrons implies that long RCSs are not initiated in energetic cascades even though they are in 450-eV recoils in the same material. Kirk and Blewitt[111] explained this observation by suggesting that the lattice would be highly disturbed in the cascade volume and that this would disrupt the RCSs before they propagate. Since the speed of sound in metals is only a factor of 2 slower than the propagation of RCSs, their interpretation may have some merit. Nevertheless, if only 4% of the disordering is due to RCSs, it means that RCSs cannot be the principal means of defect production in cascades. This point is discussed below in more detail. For the present discussion, however, it should be noted that Kirk and Blewitt's conclusions are sensitive to their model. The MD simulations described above for Ni and β-NiAl have shown that nearly all of the atoms in the cascade undergo at least one replacement during the cascade evolution. Any replacements produced by ⟨110⟩ RCSs, therefore, would be mixed further during the thermal spike, changing the local environment of Ni and Mn atoms. The simulation model, therefore, would recognize only those RCSs that extended beyond the disordered melt zone. Nevertheless, the result that the number of replacements per displacement for fast neutrons is smaller than that for the thermal neutrons does indicate that the production of long RCSs is less efficient in cascades, but the actual length distribution cannot be determined by this experiment.

Since it was noted in Section 6c that long RCSs were observed in W for 20 to 30 keV cascade events, some comment is in order, since the FIM experiments are surely the most definitive. The present authors believe that W must be somewhat unique, owing partially to its high atomic number. Cascades in W are very compact, so that most RCSs will not need to travel far through the developing cascade. The high atomic number, moreover, results in a large hard-sphere radius, which increases the focusing energy. This allows more energy for each RCS. Similar arguments, of course, apply to other heavy metals, but no experimental data are available to check this expectation.

d. *Quantitative Comparisons Between Experiments and MD Simulations*

Mixing and disordering experiments provide critical tests of the quantitative accuracy of the MD simulations. Diaz de la Rubia and Guinan have calculated mixing in Cu for a number of recoil energies between 1 and 25 keV. The mixing parameter was observed to increase with increasing

cascade energy, approximately as $E^{1/2}$. At some higher energy, the cascade will split into subcascades, and at that point the mixing becomes independent of energy; this is apparently not yet realized in Cu at 25 keV. The experimental value for the mixing parameter, Table 5, is approximately twice that found in the simulations at 25 keV; however, the mixing experiments were performed using 750-keV Kr ions and are not directly comparable to the simulations. The value of $T_{1/2}$ for the Kr irradiation is ≈ 50 keV. If the simulation data are extrapolated to 50 keV, which is a reasonable cutoff for subcascade formation, the simulation and experimental results become within a factor of 1.4, which is approaching the uncertainties in the experiments and the statistical significance of the simulations.

A similar comparison was made for Ni. For 10- and 25-keV cascades a mixing parameter of $\xi_{IM} \approx 42$ Å^5/eV was obtained, which is in very good agreement with the experimental results, although the latter again refer to higher-energy irradiations. Why the mixing parameter does not depend on energy between 10 and 25 keV in Ni but it does in Cu is uncertain; however, subcascade formation may play a role. If it is assumed that the mixing is confined to a much smaller volume in Ni cascades than in Cu, due to its higher melting temperature, then overlap of the hot subcascade cores is less likely in Ni than in Cu. Ballistic mixing may also play a larger role in the mixing in Ni, and it is independent of energy.

MD simulations have also been compared with disordering experiments in Cu_3Au. As mentioned above, electrical resistivity measurements provide the necessary sensitivity to probe disordering in nonoverlapping cascades. For 1-MeV He irradiation, moreover, nearly all the damage is produced in isolated recoils with energies less than ≈ 20 keV. A direct comparison with experiment is therefore possible by calculating the disordering rate for several energies up to 20 keV and averaging the results over the primary recoil spectrum of the He irradiation. The relationship between the change in LRO parameter deduced from experiments and the number of antisite defects found in the simulations is given by

$$\frac{\Delta S}{\Delta \Phi} = \frac{2.5 E_d N_{AS}}{X_A X_B E_C} \tag{10.2}$$

where E_d is the displacement energy, N_{AS} the number of antisite defects on one of the sublattices, E_C the damage energy in the cascade, and Φ the dose (measured in dpa). The experimental value of the disordering rate for 1-MeV He irradiation of Cu_3Au is 21 replacements per displacement,

whereas the spectrum averaged simulations yield 22 replacements per displacement.[112]

VI. Defect Production in Cascades

It was shown in the preceding section that nearly all of the atoms are displaced from their initial lattice sites in cascades. Only a few of these displacements, however, lead to the creation of point defects. Nevertheless, these defects are important since at elevated temperatures when they are mobile, they mediate such radiation effects as radiation-enhanced diffusion, segregation, and creep. For predictions of these effects it is necessary to know both the number of defects that are produced by irradiation and the detailed configuration of these defects. The first of these is treated in the present section and the latter in the following.

11. Damage Function

a. *Experimental Results*

(i) Metals. Detailed experimental studies of the damage function, $\nu(T)$, are available in very few materials, despite its central role in the calculation of radiation effects. For years the modified Kinchin–Pease expression had been used in lieu of more precise information. The primary obstacle preventing an experimental determination of $\nu(T)$ stems from the difficulty in measuring the concentration of point defects in crystals. Several measurable properties are proportional to the Frenkel pair defect concentration, but the proportionality is either unknown or depends on the detailed configuration of the defects. It is the latter that hampers the application of powerful spectroscopic methods to studies of the damage function in semiconductors and insulators. In metals, electrical resistivity measurements provide a satisfactory solution. These measurements are sensitive to small concentrations of defects; they are performed conveniently at liquid-helium temperatures, which prevents defect annealing; the resistivity increment per unit concentration of Frenkel pairs, ρ_F, is known for many metals with reasonable accuracy $\pm 25\%$;[113] and ρ_F is insensitive to the detailed configuration of the defects, at least if the defects are not too highly clustered, as in voids or dislocation loops. Values of ρ_F are included in Table 6.

---

[112] M. Ghaly, Y. S. Lee, R. S. Averback, and C. P. Flynn, unpublished result.

[113] See, e.g., P. Ehrhart, *J. Nucl. Mater.* **69/70**, 200 (1978).

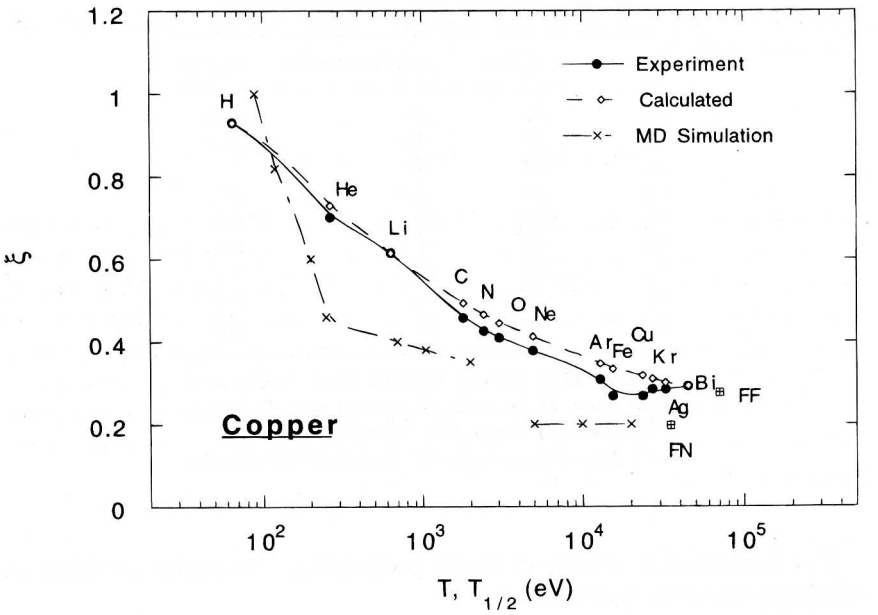

FIG. 36. Defect production efficiency in Cu plotted as a function of energy. Experimental and calculated data are plotted versus $T_{1/2}$; MD simulation are plotted versus T. (Experimental data from Ref. 114; MD simulation from Refs. 123 and 126.)

A second problem in determining the damage function concerns the production of monoenergetic recoils. MeV electrons and thermal neutrons produce recoils close to the threshold energy, and fast neutrons create recoils with energies over some tens of keV. Ion beams must therefore be used at intermediate energies. Self-ions, however, cannot be employed at low energies, owing to their shallow penetration energies below ≈ 1 MeV. Light ions have better penetration and produce some recoils at low energies, but each ion creates a spectrum of host atom recoils. The experimental procedure, therefore has been to irradiate thin films with a series of energetic ions, ranging in mass from protons to self-ions, and measuring the defect production due to each. As the ion mass becomes heavier, the recoil spectrum shifts to higher energies (see Fig. 10). The damage function is then obtained by deconvolution of Eq. (3.5) using data for $\nu(E_1)$ from each ion irradiation. This procedure is now widely employed for investigating the influence of recoil spectrum on a number of radiation effects.

TABLE 6. CASCADE EFFICIENCIES IN METALS[a]

ELEMENT	E_d (eV)	ρ_F ($\mu\Omega \cdot$ cm/at%)	$\xi_{FP}(T_S)$
Ag	39	2.1	0.38
Al	27	4.0	0.40
Au	43	3	
Cu	29	2.5	0.25
Fe	40	20	0.39
Ni	40	7.1	0.30
Mo	60	15	0.38
Pt	43	9.5	0.37
W	90	27	0.66

Source: Data from G. Wallner, M. S. Anand, L. R. Greenwood, M. A. Kirk, W. Mansel, and W. Waschkowski, *J. Nucl. Mater.* **152**, 146 (1988).

[a] Values of E_d and ρ_F used for analysis are indicated.

For fundamental studies of defect production, it is useful to define an efficiency function, $\xi_{FP}(T)$, where

$$\nu(T) = \xi_{FP}(T)\nu^{KP}(T) \tag{11.1}$$

and $\nu^{KP}(T)$ was defined in Eq. (3.4). $\xi_{FP}(T)$, therefore, is a measure of the deviations from the Kinchin–Pease model. Complete damage functions have been obtained for only few metals using the procedures just outlined.[114,115] An example is shown in Fig. 36 for Cu. Here $\xi_{FP}(T)$ is plotted versus $T_{1/2}$ rather than T. Recall that $T_{1/2}$ is a spectrum average such that half of the defects are created in recoils both below and above $T_{1/2}$. The main results are that the defect production efficiency falls off very rapidly from unity with energy near the displacement energy and approaches an asymptotic value, $\xi_{FP}(T_S)$, $\approx 1/3$, at high energies, $T > T_s$, where $T_s \approx 2$ to 5 keV. Data for fast neutron and fission fragment irradiation of Cu have been included in the plot for comparison. The general findings seen here for Cu of a rapid decline in $\xi_{FP}(T)$ at low energies and an asymptotic value of $\approx 1/3$ were also observed in Ag[114] Al[114] and Fe.[115] A far more extensive set of data for just $\xi_{FP}(T_s)$ have been obtained using electrical resistivity

[114] R. S. Averback, R. Benedek, and K. L. Merkle, *Phys. Rev. B* **18**, 4156 (1978); R. S. Averback, R. Benedek, K. L. Merkle, and J. Sprinkle, *J. Nucl. Mater.* **113**, 211 (1983).

[115] C. Jaoruen, J. P. Riviere, C. Templier, and J. Delafond, *J. Nucl. Mater.* **131**, 11 (1985).

measurements on specimens irradiated with fast neutron. These data are compiled in Table 6.[116] Most values of $\xi_{FP}(T_S)$ are between 0.25 and 0.40.

Values of $\xi_{FP}(T_s)$ for W[117] and Pt[118] have been obtained more directly using field ion microscopy. These studies used irradiations with particles ranging in mass from 40 (Ar) to 174 (W) amu and varying in energy from 15 to 90 keV. Lower energies could not be employed without significant interference from the surface. The results of these investigations are that the efficiencies for both Pt and W are independent of the projectile mass and energy and that $\xi_{FP}(T_s) \approx 1.0$. The first result, that $\xi_{FP}(T)$ does not vary with the mass and energy of the irradiation particles, indicates that T was greater than T_s for all these irradiations; this is consistent with the results on Cu. The values of $\xi_{FP}(T_S)$, however, are significantly higher than those found using electrical resistivity measurements on W and Pt and most other metals (see Table 6). Although the efficiency for W shown in Table 6, $\xi_{FP}(T_S) \approx 0.7$, is not far different from the FIM result, the comparison is misleading, since in the FIM study E_d was assumed equal to 56 eV, whereas, in the electrical resistivity study it was assumed to be 90 eV. The actual difference between the experiments is therefore nearly a factor of 2. This difference has been difficult to resolve. The resistivity measurements suffer from the uncertainty in ρ_F in W, and also from the assumption that ρ_F is independent of defect configuration since defects in cascades in Pt and W are highly clustered. The FIM experiments, however, examine damage very close to the surface, and it will be shown in Section 14b that this may lead to an overestimate of the defect production.

(ii) SILICON. Damage in Si has been investigated by RBS channeling.[119] Channeling detects the number of atoms displaced from crystal lattice sites; however, for quantitative studies the location of the atoms in the channel must be known. In most studies, it is assumed that the interstitial atoms are distributed uniformly in the channels. A drawback of the method is its poor sensitivity to defects, ≈ 1 at%, so that high defect levels are required.

The damage function in Si deduced from these experiments appears quite different from metals. The production efficiency is not observed to decrease with increasing recoil energy, but rather, it remains nearly unity over a wide range of projectile masses and energies. For irradiations with very heavy ions for which the energy density in cascades is raised above that attainable

[116] G. Wallner, M. S. Anand, L. R. Greenwood, M. A. Kirk, W. Mansel, and W. Waschkowski, *J. Nucl. Mater.* **152**, 146 (1988).
[117] C. Y. Wei, M. I. Current, and D. N. Seidman, *Philos. Mag. A* **44**, 459 (1981).
[118] D. Pramanik and D. N. Seidman, *J. Appl. Phys.* **60**, 137 (1986).
[119] D. A. Thompson, *Radiat. Eff.* **56**, 105 (1981).

by Si projectiles, the production efficiency is observed to increase above unity. An additional observation that adds insight to the defect production process in Si is that the production efficiency is an increasing function of ion dose,[119] a result that is contradictory to the concept of spontaneous recombination volumes. This indicates that defect production is made easier in damaged regions. The different defect production behavior observed in metals and in Si will be seen to stem from the amorphization of Si under irradiation.

b. *MD Simulations of Defect Production*

Although it has been recognized for some time that thermal spikes must be responsible for $\xi_{FP}(T)$ decreasing with increasing recoil energy,[114] the details of the defect production process are only now being established. Using a pair potential for W in their MD code, Guinan and Kinney were able to reproduce the general form of the damage function.[120] They attributed their reduced production efficiency to defect migration and recombination during the thermal spike phase of a cascade. Subsequent simulations on Cu showed that reduced defect production could be associated more specifically with local melting in the cascade.[78] The mechanism proposed was that Frenkel pairs created during the collisional phase of the cascade are subsequently absorbed in the local melt. On resolidification, the crystal grows back almost perfectly, restoring an essentially defect-free crystal. Only those interstitials ejected from the melt, and a corresponding number of vacancies in the center of the cascade, remain as lasting damage. The decrease in the production efficiency with energy was attributed to the corresponding increase in the volume of the melt and the decreasing probability for an interstitial to be ejected beyond its boundaries.

The possibility that regrowth of the local melt restores a nearly damage-free crystal has been tested further by MD simulations in the following manner. A local region of lattice in Au was doped with various concentrations of vacancies and interstitials and an energetic recoil was subsequently initiated in this vicinity. In the region that had undergone local melting, all the preexisting Frenkel pairs recombined, leaving only the original excess of one or the other of the defects. Outside the melt zone, on the other hand, very few defects recombined.[121]

The foregoing picture of defect production in cascades illustrates a few general points. The first concerns regrowth of the solid. As noted above, growth of defect-free crystalline metals can be maintained even though the

[120] M. W. Guinan and J. H. Kenny, *J. Nucl. Mater.* **103/104**, 1319 (1981).
[121] K. Nordlund and R. S. Averback, Phys. Rev. B (in press).

velocity of the resolidification front is a few tenths of the speed of sound. In semiconductors the kinetics of crystallization is much slower than in metals, so that Si quenches into an amorphous phase. Damage in semiconductors, is therefore enhanced in cascades by the melting process rather than being reduced. The second concerns the absorption of interstitials and vacancies in the melt. The addition of an interstitial atom into a liquid creates high local stresses. These cannot be supported in a material with a vanishingly small shear modulus, so the matrix relaxes around the extra atom. The relaxation radiates outward from the defect at approximately the speed of sound, and thus the interstitial is quickly absorbed in the liquid. The effective recombination of the interstitials and vacancies in the liquid therefore occurs before the melt can resolidify.

c. *Comparison Between Simulated and Experimental Damage Functions*

(i) METALS. Damage functions obtained by MD simulations are shown in Fig. 37 for a number of metals.[122] The remarkable feature is their similarity. Physical properties of the metals, such as melting temperature and atomic number, which cause large variations in ion mixing, have a negligible effect

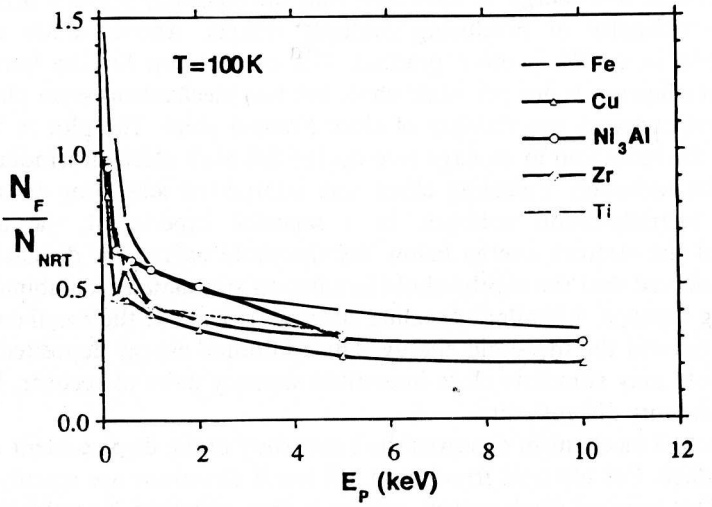

FIG. 37. Defect production efficiency function, $\xi(T) = N_F/N_{NRT}$, calculated for several metals using MD, shown as a function of energy. (After Ref. 122.)

[122] D. J. Bacon, in *Computer Simulations of Materials*, ed. H. O. Kirchner *et al.*, Kluwer Academic Publ., The Netherlands, 1996 189.

on the production efficiency. A part of the reason must lie in the high rate at which interstitials are absorbed into the melt. Once this has been achieved, no further reduction in the mixing efficiency is possible, except possibly for a few additional interstitials migrating from the periphery of the cascade back into the melt. For mixing, on the other hand, the relocation of atoms depends on the temperature of the spike and its duration.

The overall agreement between the experimentally determined damage functions in Cu, Ag, and Al and the MD simulations is remarkably good. The defect production efficiencies drop very rapidly and $\xi_{FP}(T_S) \approx \frac{1}{3}$. A comparison between simulation and experiment is illustrated in Fig. 36, where the MD efficiency function for Cu[123] is shown along with the experimental function. The MD function, however, is plotted as a function of recoil energy, while the experimental data are plotted versus $T_{1/2}$. The two sets of data can be directly compared, however, by calculating the defect production for each ion irradiation using the MD-simulated damage function in Eq. (3.5). The results are calculated in Fig. 36.

An interesting feature in the true damage function that might be missed in the experimental plot of $T_{1/2}$ is the precipitous drop in the efficiency function just above the threshold energy. By 250 eV, $\xi_{FP}(T)$ has already fallen below 0.4, which means that on average only 1.3 defects are produced per recoil at this energy. It illustrates that the efficiency initially drops due to the difficulty of producing multiple defects. Above $\approx$500 eV the reduction in $\xi_{FP}(T)$ is more gradual. The explanation for the immediate drop in efficiency is not yet established, but two mechanisms seem plausible. The first concerns the stability of close Frenkel pairs. The plot in Fig. 12 shows the reduction in damage rate during 2.8-MeV electron irradiation of Cu. The radiation annealing effect was interpreted according to spontaneous recombination volumes. In a separate experiment, the authors reduced the electron energy below the threshold energy for displacements and observed that the subthreshold irradiation stimulated recombination of existing damage. A similar annealing effect may occur as the recoil energy is raised beyond the threshold energy. The additional energy deposited at the recoil site may stimulate close interstitial-vacancy pairs to recover, leaving only the more distant pairs.

A second mechanism concerns the anisotropy of the displacement threshold surface. For electron irradiation, all recoil directions are equally probable. The average displacement energy is thus obtained by averaging the threshold energy over all solid angles, including close-packed directions. Once the recoil atom leaves its lattice site, however, secondary collisions

[123] A. J. E. Foreman, W. J. Phythian, and C. A. English, *Philos. Mag. A* **66**, 671 (1992).

along close-packed directions are no longer accessible, owing to a shadowing effect from the atoms in the row. This situation is analogous to blocking in channeling experiments. The elimination of these "easy" directions for displacements could lower the efficiency for defect production. Reduction in efficiencies from crystallinity effects was suggested by Lucasson much earlier.[124]

(ii) SILICON. The damage function in Si and other covalently bonded materials was noted above to exceed the estimates of linear cascade theory for cascade energy densities larger than a few tenths of an electron volt per atom. This has been interpreted as being the result of amorphization induced by the thermal spike. Recent MD simulations on damage production in Si have shown that solidification of the locally molten cascade zone occurs at a rate $\approx 10^{14}$ to 10^{15} K/s, which in Si would lead to interface velocities much larger than the critical velocity for amorphization.[125] Figure 38 illustrates the dynamics of a 5-keV Si impact in a Si lattice. Only atoms with potential energies $E_P > 0.2$ eV above the ground-state energy are represented in the figure. The diameter of each symbol provides an indication of the potential energy of the atom in the range 0.2 to 1 eV or larger. The gray level of the spheres indicates atomic level stress, σ. The gray scale ranges from light for tensile stress to dark for compressive stress.

At the start of the collision process, the energy is concentrated in a relatively small number of atoms with large potential energies, as shown in Fig. 38. At this time, 0.1 ps after the start of the 5-keV atom, the region of damage has not extended to its full extent, and the cascade region is under large compressive stress. The maximum number of atoms with $E_P > 0.2$ eV occurs about 0.2 ps after the first collision; at this point the average total energy per atom is ≈ 1 eV for those atoms with $E_P > 0.2$ eV. The average potential energy of the atoms illustrated in Fig. 38(b) ($t = 1$ ps) is 0.47 eV, whereas the latent heat of fusion given by the Stillinger-Weber potential is 0.325, suggesting that these particles may have properties similar to that of liquid Si. Figure 38c shows that ≈ 500 atoms still have $E_P \geq 0.2$ eV after 8 ps; the average potential energy of these atoms is 0.34 eV.

Further analysis of the simulation data showed that the average coordination number in the cascade region, as determined from integrating the pair correlation function out to the first minimum, increases to a value of ≈ 6.5 at 0.5 ps and then decreases to ≈ 4.3 after equilibration with the surrounding lattice. These coordinations are suggestive of local melting at the

---

[124] P. Lucasson, *Fundamental Aspects of Radiation Damage in Metals*, ed. M. T. Robinson and F. W. Yound, Jr., ERDA Report CONF-751006 (1975) p. 42.

[125] T. Diaz de la Rubia and G. H. Gilmer, *Phys. Rev. Lett.* **74**, 2507 (1995).

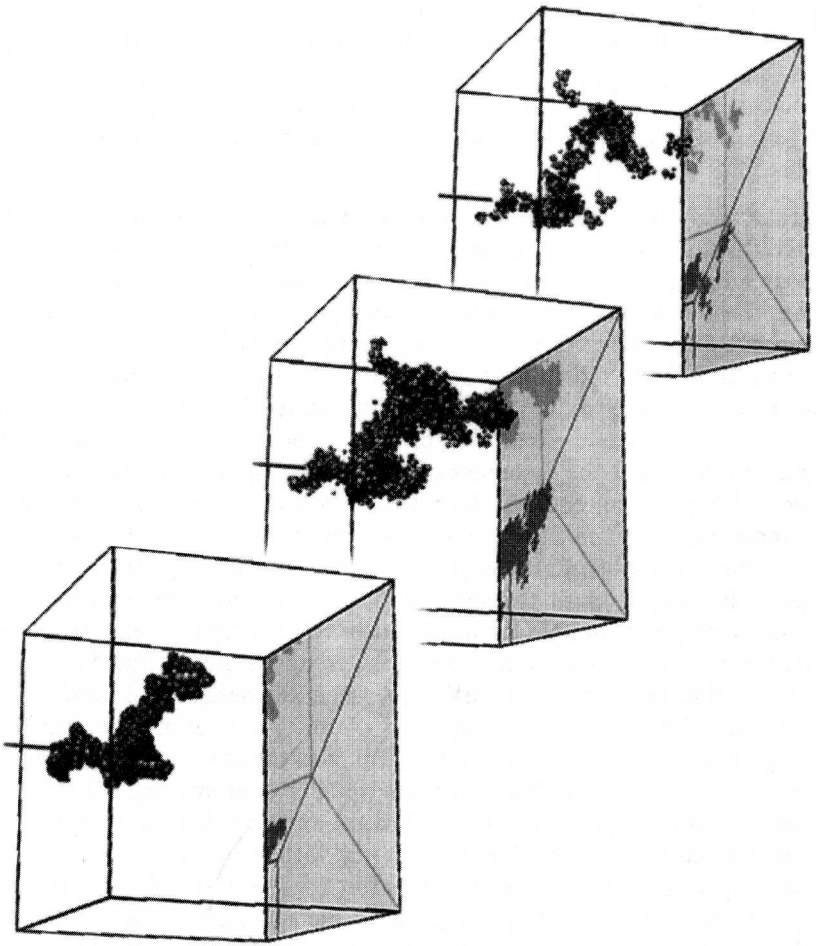

FIG. 38. Three snapshots of a 5-keV cascade in Si initiated by a Si recoil at the surface. The atoms shown are those with potential energy >0.2 eV above the ground state of the silicon crystal. The development of the damage is shown at (a) 0.1 ps, (b) 0.5 ps, and (c) 6 ps. The gray scale represents the atomic level stress. (After Ref. 125.)

earlier time, followed by solidification. Similarly, the density in the cascade region at 0.5 ps becomes somewhat larger (3%) than the crystalline density, and the local stress also becomes tensile at about 0.5 ps. These changes are consistent with the coordination number changes described above. The results are all consistent with the idea that a local melt of liquid Si quenches to form a highly nonequilibrium, amorphous material.

In good agreement with the experimental evidence, the MD results on silicon show that the number of displaced atoms produced in cascades by light ions is comparable to the prediction of the modified Kinchin–Pease equation. However, for heavy ions such as As and Pt, the formation of very large amorphous pockets results in twice as many displaced atoms at room temperature and below than is predicted by the BCA calculations.

VII. Primary State of Damage

12. MD Simulations of Defect Structures

(i) Metals. The descriptions of cascade dynamics and the mechanisms of defect production presented earlier suggest that the primary state of damage in metals will consist of a mantle of isolated interstitial atoms surrounding a core of vacancies called a depleted zone. Examination of the details of the MD simulations, however, reveals a more complex dynamics in the development of the defect structures. First, Foreman *et al.* noticed a strong tendency for the interstitials to cluster on the periphery of the cascade, even in a cascade of only 2.5 keV.[123] Figure 39 shows this tendency for interstitial clustering in Cu as a function of cascade energy.[126] It is observed that in Cu the fraction of interstitials in clusters increases with energy, becoming $\approx \frac{3}{4}$ by 25 keV. Clustering has been observed in most

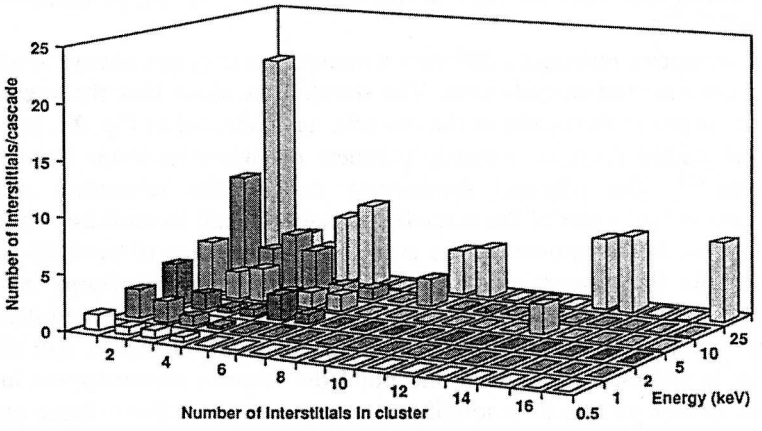

Fig. 39. Cluster-size distribution of interstitial atoms observed in MD simulations of Cu. (After Ref. 126.)

[126] Reprinted from T. Diaz de la Rubia and W. J. Phythian, *J. Nucl. Mater.* **191–194**, 108 (1992) with kind permission from Elsevier Science–NL, Sara Burgerhartstraat 25, 1055 KV, Amsterdam, The Netherlands.

other pure metals that have been examined as well.[127] Farther away from the cascade, the interstitials are mostly isolated, as they are produced by RCSs.

The reason for the interstitial clustering is still unclear. Small clusters, two or three interstitial atoms, possibly form by nearby interstitial atoms migrating under their strong elastic attraction during the thermal spike. Large clusters, however, cannot form by this method, since migration is limited to ≈ 1 or 2 steps during the thermal spike.[121] It is observed in higher energy events in Cu and Au, that interstitial clusters tend to form planar structures on the periphery of the melt. An example is illustrated in Fig. 28 for a 10 keV event in Au. These finding suggest that the large interstitial platelets are created in a collective event, possibly induced by high shear stresses which develop in the thermal spike. Recent simulations of 10 and 30 keV cascades in Au have shown that the atomic-level stresses in the cascade core are very different for events where interstitial clusters are produced from those where clusters are not produced.[128] For cascades where interstitial loops are produced, very high shear stresses develop during the first few tenths of picoseconds in the neighbourhood of the region where the loops eventually appear. In fact, loops are already visible in the cascade periphery 0.4 ps after the initiation of the event, indicating that the clusters are initiated by the high pressure wave leaving the cascade. Whatever their cause, the creation of interstitials in clusters, rather than as single defects, has a strong influence on various radiation effects, as will be discussed in section IX.

The vacancies undergo a different dynamics, as they are always confined to the once-melted cascade core. The simulations show that the vacancies tend to cluster in the center of the cascade, as illustrated in Fig. 28. In a few cases at higher energies, vacancy platelets or prismatic loops have been observed.[128] The physical mechanism driving the relocation of the vacancies to the center of the cascade has been difficult to establish from the simulations, but it appears to be a simple consequence of resolidification kinetics. As the cascade cools, the solid–liquid interface sweeps inward, leaving a perfect lattice behind. Depending on the velocity of the interface, excess free volume in the liquid, from the original vacancies, can either migrate in advance of the front and build the vacancy concentration in the cascade center, as in a slow solidification process, or the free volume can be overrun by the interface and freeze out as vacancies more uniformly in the

[127] See, e.g., D. J. Bacon, A. F. Calder, F. Gao, V. G. Kapinos, and S. J. Wooding, *Nucl. Instrum. Methods B* **102**, 37 (1995).

[128] E. Alonso, M. J. Caturla, M. Tang, H. Huang and T. Diaz de la Rubia, *Mater. Res. Soc. Symp. Proc.* (Fall 1996), in press.

solid. This process has been likened to zone refining.[78] Other mechanisms, however, have been discussed.[129]

(ii) SILICON. MD simulations of displacement cascades in Si show that few isolated Frenkel pairs are produced. Most of the damage, particularly for heavy ions, is in the form of amorphous pockets.[130] This point is illustrated by comparing the damage produced by B and As ions. Figure 40 shows a two-dimensional projection onto a (001) plane of the displaced atoms that were produced by 3-keV B (a) and 15-keV As (b) cascades, and their nascent lattice sites. Also shown in the figure are the trajectories of the incoming ion and secondary recoils and the excess (+) or deficit (−) of atoms in several of the damage clusters. The figure illustrates that while a number of isolated Frenkel pairs and small clusters are observed in the case of the B cascade, large amorphous clusters of displaced atoms dominate the damage in the As irradiation.

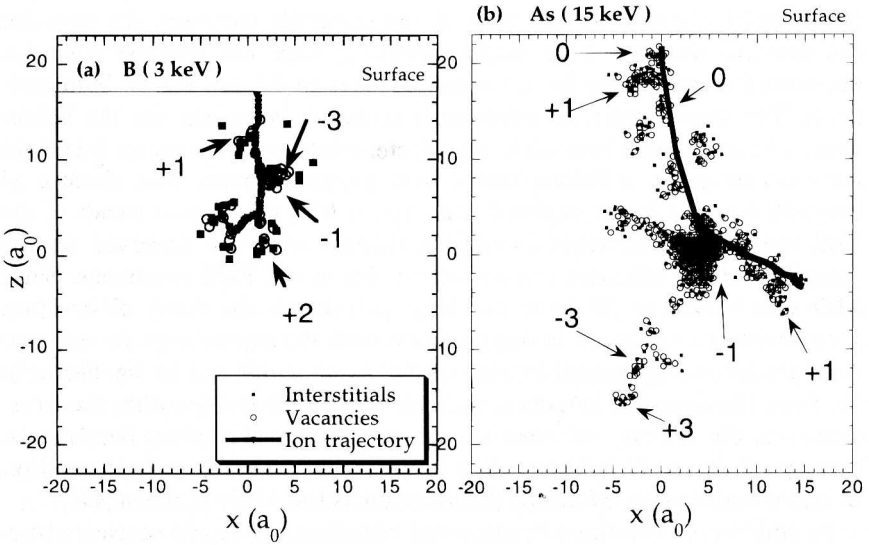

FIG. 40. Two-dimensional projection on a (010) plane of the vacancies and interstitials produced by (a) a 3-keV B recoil and (b) a 15-keV As recoil in Si. (After Ref. 130.)

[129] V. I. Protasov and V. G. Chudinov, *Radiat. Eff.* **66**, 1 (1982).

[130] M. J. Caturla, T. Diaz de la Rubia, L. Marques, and G. H. Gilmer, *Phys. Rev. B* **54**, 16683 (1996).

13. Experimental Observations of Defects Structures in Cascades

a. *Field Ion Microscopy*

Snapshots of the cascade structure in W and Pt have been obtained experimentally using field ion microscopy.[117,118] Although such pictures are currently available for just these two materials, they represent the only experimental evaluation of the cascade structure on an atomic level and therefore warrant detailed discussion. It was remarked above that the proximity of the cascade zone to the surface may influence the defect production efficiency; this remark, however, is presently one of conjecture. In any case it is not likely that these surface effects will greatly influence the structure of the cascades, at least in the more refractory metal, W (see Section VIII). For this reason, however, only the experiments on W are discussed here.

In Fig. 41 the locations of individual vacancies produced by 30-keV projectiles of Cr, Mo, or W are shown. No interstitial atoms were observed in these depleted zones. As the mass of the projectile increases, the cascades are seen to become increasingly compact, with the cascade diameter decreasing from 3.1 nm for Cr bombardment to 1.1 nm for W bombardment. The development of subcascade structure is evident for the lighter ions, which is consistent with Fig. 7, showing how the mean free path between energetic collisions varies with projectile mass. The absence of interstitial atoms in the depleted zone agrees with the general trends of the MD simulations; however, interstitial clusters were not observed on the periphery of the cascades nor anywhere else in the FIM specimens. Since MD simulations on W have not been performed, the latter observation should not be considered in disagreement with the simulations. In fact, two considerations suggest that interstitial clustering would not be significant in W. First, the extended lengths of RCSs in W will efficiently scatter the interstitials in the matrix, reducing the probability for clustering. Second, the shear modulus in W is higher than in most other metals, so the formation of interstitial clusters by plastic deformation, is less likely in this metal.

In addition to the three-dimensional visualizations of the cascade structures in W, the FIM provides a wealth of quantitative information. For example, the degree of vacancy clustering within cascades has been examined by forming the size distributions of vacancy clusters. This distribution, F_n, was defined as

$$F_n = \frac{n_{\mathrm{cl}} N_n}{\sum_n n_{\mathrm{cl}} N_n}, \tag{13.1}$$

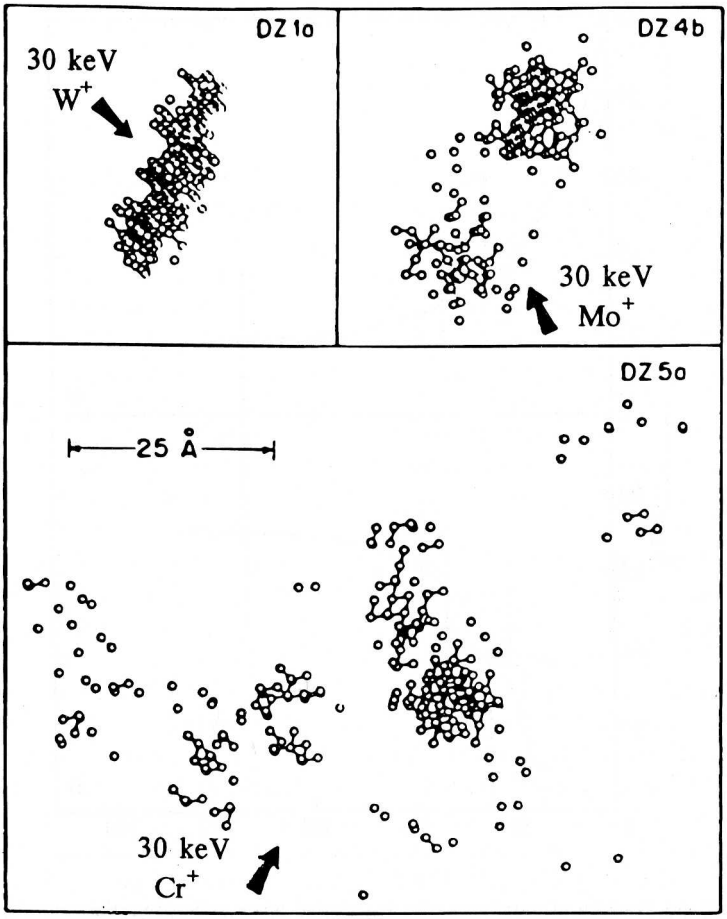

FIG. 41. Visualization of three depleted zones in W produced by 30-keV bombardment with W, Mo, or Cr projectiles. Nearest-neighbor vacancies are connected by a rod. (After Ref. 72.)

where N_n is the number of clusters of size n_{cl}. The cluster size n_{cl} is the number of vacancies within a nearest-neighbor distance of another vacancy in the same cluster. The results are plotted in Fig. 42 for monovacancies, $n_{cl} = 1$, and for large clusters, $n_{cl} > 10$, as a function of projectile mass. The cascade energy was 30 keV in all cases. The fractions of vacancies in just these two groups were 75 to 90% for the irradiation particles studied. The dashed line shown in the figure extrapolates F_1 to $m_1 = 1$, assuming that $F_1 = 1$ at this mass. A remarkable similarity appears between this curve

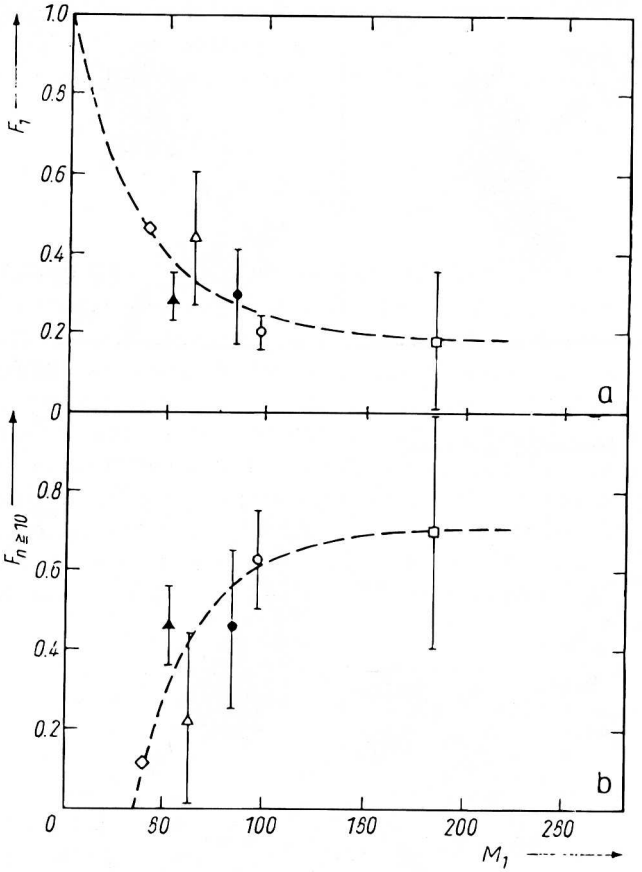

FIG. 42. (a) Fraction of monovacancies F_1, plotted against the projectile mass for 30-keV projectiles; (b) fraction of vacancies in large clusters $F_{n>10}$ plotted against projectile mass for the same 30-keV particles. (After Ref. 72.)

and that shown for defect production, Fig. 36, which reinforces the suggestion made in Section 11c that once multiple defects are produced by a recoil, the defect production efficiency drops very quickly. Unfortunately, no irradiations were performed in this study using projectiles with lower masses. The fractions F_1 and $F_{>10}$ show similar, but inverse, dependencies on mass. For self-ion bombardment, the cascades consist mostly of large vacancy clusters and relatively few single vacancies, and even these few monovacancies were reported to be in close proximity to other vacancies.

The distributions of vacancies in cascades were further quantified using radial distribution functions (RDFs), $\langle R(i) \rangle$, which were defined as the

average atom fraction of vacancies at the jth nearest-neighbor distance around any given vacancy. Since the coordination number, $Z(i)$, varies on the different nearest-neighbor shells, Current *et al.* also defined the more relevant quantity,

$$\frac{\langle R(i)\rangle}{Z(i)} = \frac{1}{vZ(i)} \sum_{j=1}^{v} A(i, j), \tag{13.2}$$

where $A(i, j)$ is the number of vacancies on the ith nearest-neighbor shell surrounding vacancy j, and v is the number of vacancies in the FIM specimen.[131] This quantity, therefore, is simply the concentration of vacancies on the ith nearest-neighbor shell. Variations of these concentrations with i indicate correlations in the vacancy locations in the cascade. Figure 43 illustrates RDFs for W specimens irradiated with a series of ions. Perhaps most remarkable is the high concentration of vacancies at the first few shells after self bombardment, ≈ 30 at%, suggesting a spongelike structure. It was also observed that varying the energy of Kr ions between 15 and 70 keV had no effect on the RDFs. This suggests that subcascade structure already develops for Kr bombardment of W above ≈ 15 keV. In contrast to the

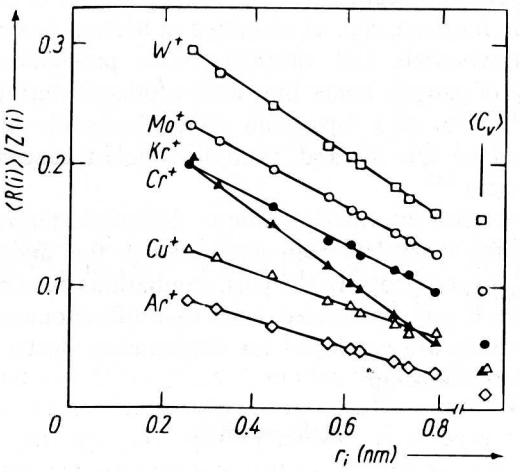

FIG. 43. Radial distribution functions of vacancies plotted versus distance (or neighboring site separation) for a series of ion irradiations; C_v refers to the average concentration of vacancies in the cascade. (After Ref. 131.)

[131] M. I. Current, C.-Y. Wei, and D. N. Seidman, *Phil-Mag. A* **47**, 407 (1983).

energy dependence, a strong effect of ion mass is observed. With the exception of Cr, for which the statistics were reported to be poor, the slopes of the RDFs decrease with decreasing ion mass. This trend is a direct reflection of the decrease of vacancy clustering with decreasing ion mass. At the most distant shells, which extend only 0.8 nm, the RDFs tend toward the average vacancy concentration in the cascade. These studies show, therefore, that the primary state of damage in W consists of a very compact, highly depleted cascade zone, with the interstitials well separated from the vacancies.

b. *Diffuse X-ray Scattering*

Unlike FIM, diffuse x-ray scattering (DXS) probes the average defect structures in displacement cascades. The method is particularly useful for damage studies since it is sensitive to defects ranging in size from a single point defect to defect clusters extending several nanometers. The experimental details of applying DXS to damage studies can be found in a recent review.[73] Most investigations have employed the diffuse scattering close to the Bragg peaks for defect studies, or Huang scattering (HDS). Different kinds of information are available by this method. For example, a measure of the spatial extent of cascades is provided by the Fourier transform of the defect correlation function, $c(q)$, as described in Section 6c for obtaining the separation of interstitials and vacancies. This procedure was used to examine the size of cascade zones that were produced during neutron irradiation at 6 K.[132] For Al a "spectrum average" cascade size of $\langle r \rangle \approx 9.3$ nm was obtained by this method, yielding a defect concentration in the cascades of 360 ppm.[133]

DXS also provides information about defect clustering in cascades. Unfortunately, little work has been performed in this area, owing to the difficulty of these experiments. In the past, irradiations have been performed in a reactor at 4.6 K and transferred, cold, to a diffractometer for measurements. Two methods are employed for determining cluster size. The first makes use of the relationship

$$S_n(\mathbf{k}) = nS(\mathbf{k}), \tag{13.3}$$

where $S_n(\mathbf{k})$ is the scattering arising from a concentration of c/n defect clusters each containing n point defects. $S(\mathbf{k})$ is the scattering intensity for a

[132] B. von Guerard, D. Grasse, and J. Peisl, *Phys. Rev. Lett.* **44**, 262 (1980).
[133] R. Rausch, J. Peisl, A. Schmalzbauer, and G. Wallner, *J. Nucl. Mater.* **168**, 101 (1989).

concentration of c point defects and is given by

$$S(\mathbf{k}) \propto c\,|f|^2\left(\frac{\Omega_{\text{rel}}}{\Omega_0}\frac{\mathbf{k}}{q}\right)^2, \tag{13.4}$$

where f is the atomic form factor, Ω_{rel} the relaxation volume of the defect, Ω_0 the atomic volume, and $\mathbf{q}$, as before, is the difference in the scattering vector $\mathbf{k}$ and the closest reciprocal lattice vector. It is from the dependence on the square of Ω_{rel} that the scattering from clustered defects increases by a factor of n, since it is assumed in Eq. (13.4) that the strain fields of the defects in the cluster superpose linearly. This is a good approximation for small clusters. Once the clusters form loops, other methods must be applied. The results from this neutron study are listed in Table 7. The primary observation is that the average size of interstitial clusters is small, with Cu being the sole exception. Since the relaxation volumes of vacancies are small compared to interstitials in metals, vacancy clustering cannot be studied by this method.

The DXS results are in qualitative agreement with the MD simulations. Direct comparison is not possible due to the different energies employed in the simulations and experiments. For Al the small cluster size is expected from the low energy density in the cascades. Results of a recent MD simulation of a single 5-keV event in Al, in fact, showed two small interstitial clusters of size $n = 4$ and 2 single interstitials. The average based on Eq. (13.3) is ≈ 3.4.[121] Fe too is a light metal, and since it has a high melting

TABLE 7. SIZES OF INTERSTITIAL CLUSTERS FOLLOWING FAST NEUTRON IRRADIATION OF METALS AT 6 K

METAL	Al[a]	Mo[b]	Cu[c]	Fe[d]
Cluster size	2–3	2	14	1.5

[a] Data from B. von Guerard, D. Grasse, and J. Peisl, *Phys. Rev. Lett.* **44**, 262 (1980); R. Rausch, J. Peisl, A. Schmalzbauer, and G. Wallner, *J. Nucl. Mater.* **168**, 101 (1989).

[b] Data from D. Grasse, B. von Guerard, and J. Peisl, *J. Nucl. Mater.* **120**, 304 (1984).

[c] Data from R. Rausch, J. Peisl, A. Schmalzbauer, and G. Wallner, *J. Nucl. Mater.* **168**, 101 (1989).

[d] Data from J. Peisl, H. Franz, A. Schmalzbauer, and G. Wallner, *Mat. Res. Soc. Sym. Proc.* **209**, 271 (1991).

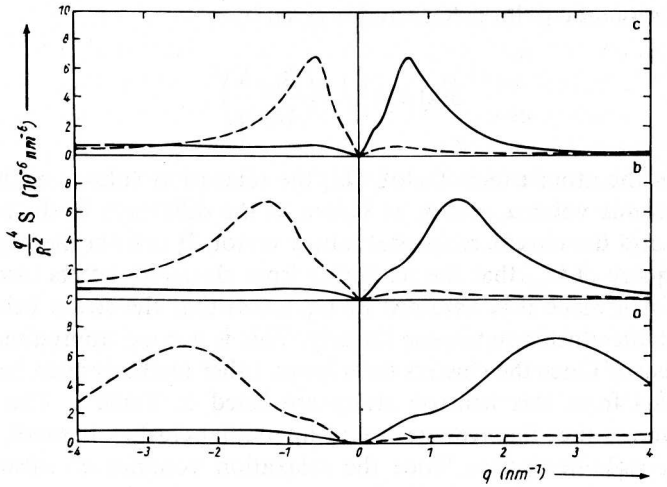

FIG. 44. Diffuse scattering intensities calculated for vacancy (dashed) and interstitial (solid) faulted loops of radius R in Cu plotted as a function of radial distance, q, from a (222) reflection: (a) $R = 1$ nm; (b) $R = 2$ nm; (c) $R = 4$ nm. (After Ref. 73.)

temperature, interstitial clustering is again expected to be small, which is confirmed by the DXS observations. In good agreement with this result Phythian *et al.* found an average interstitial cluster size <2 in MD simulations of 5 and 10 keV cascades in Fe.[134] In addition Bacon *et al.* observed an average of 2.2 interstitials per cluster for 5-keV cascades in Ti, a metal of similar cohesive properties and atomic number as Fe.[127] Only small clusters are found in Mo as well. This agrees with the findings of the FIM study on W, which is a similarly refractory metal of high atomic number.[117] Only Cu shows large clusters, with an average size of 14. This result supports the findings of MD simulations for which large interstitial clusters were also observed. These combined MD and DXS results illustrate that in most metals interstitial clustering is likely to be small, with average cluster sizes of 2 to 3. Only in metals with high atomic number and low melting temperature are large interstitial cluster or loops likely to be produced. A metal with the average "thermal spike" properties of Cu appears to mark the transition from small to large interstitial cluster formation.

Diffuse x-ray scattering can also be employed to quantitatively examine defects that have formed dislocation loops. The method requires first calculating the displacement fields around dislocation loops and then performing

[134] W. J. Phythian, R. E. Stoller, A. J. E. Foreman, A. F. Calder, and D. J. Bacon, *J. Nucl. Mater.* **223**, 245 (1995).

discrete sums for the DXS.[73] Figure 44 illustrates the scattering intensity in the ⟨111⟩ direction near a (222) reflection in face-centered-cubic structure for a faulted (Frank) dislocation loop. The nature of the loop, vacancy or interstitial, is determined by the position of the scattering intensity relative to the Bragg reflection. The value of the scattering vector, $\mathbf{q}$, where the quantity $\mathbf{q}^4 S(\mathbf{q})$ reaches a maximum, determines the radius of the loop, and the absolute intensity determines the concentration of such loops.

This method was employed to examine Cu and Ni samples that were irradiated with fast neutrons at 6 K but partially warmed before they were examined.[135] The Cu sample was warmed to 80 K and the Ni sample was warmed to 300 K. In both cases interstitial atoms became mobile during the warming but the vacancies remained immobile. The results are compiled in Table 8. For both Cu and Ni, the interstitial loops are predominant, which is expected since interstitial atoms were able to undergo clustering reactions during warming. The interesting feature, however, is that some vacancy loops are also observed even though no vacancy migration was possible. For Ni, the fraction of recoils with energies greater than 10 keV that produced vacancy clusters was 0.30, and for Cu it was 0.20. It was further concluded in this study that 20% of the vacancies in Ni and 40% in Cu were contained in loops.

c. *Transmission Electron Microscopy*

The most commonly used method for studying radiation damage in materials has been transmission electron microscopy (TEM). The TEM shares the common advantage with FIM that defects are individually imaged, thus making it possible to obtain quantitative information about single cascade events. Unfortunately, TEM does not offer the same spatial resolution as FIM. Defects are only imaged in the TEM through their strain fields, and these are generally only of sufficient strength for imaging

TABLE 8. INTERSTITIAL AND VACANCY LOOPS IN NEUTRON-IRRADIATED Cu AND Ni[a]

	T (K)	N_i (10^{19} cm^{-3})	$\sqrt{\langle R_i^2 \rangle}$ (Å)	N_i^L (10^{17} cm^3)	N_v^* (10^{19} cm^{-3})	$\sqrt{\langle R_v^2 \rangle}$ (Å)	N_v^L (10^{17} cm^3)	$N_i(\%)/N_v(\%)$
Nickel	300	0.21	11.0	0.29	0.041	7.0	0.17	84/16
Copper	100	0.7	11.0	0.9	0.27	12.5	0.3	72/28

Source: Data from P. Ehrhart and R. S. Averback, *Philos. Mag. A* **60**, 283 (1989).

[a] $N_{i,v}$, interstitial atom, vacancy concentration; $R_{i,v}$, radius of loop; $N_{i,v}^L$, interstitial atom, vacancy loop concentration; $N_{i,v}(\%)$ = percentage of observed defects that are interstitial, vacancy.

[135] P. Ehrhart and R. S. Averback, *Philos. Mag. A* **60**, 283 (1989).

when the defects have condensed into dislocation loops of a size containing more than ≈ 20 defects. Most defects produced in individual cascade events are, in fact, not observed, which has the unfortunate consequence that deductions about defect structures derive from observations on a small fraction of the defects. TEM has the further disadvantage that thin films must be employed for imaging, and hence possible interference of the surfaces plagues many of these studies. A few potential problems are: point defects can migrate to the surface, defect loops can glide to the surface, and the surface can alter the defect production mechanism. The latter is discussed below. A review of TEM methods for imaging defects can be found in the literature.[136]

Information obtained by TEM methods is usually expressed in terms of defect yield, Y, which is the probability for an incident ion to produce a visible defect, and cascade efficiency, ξ_{TEM}. This efficiency is similar to that for defect production, although in the present context, it is the ratio of the average number of defects contained in the visible loops to the number calculated using the modified Kinchin–Pease expression. A selected set of data are tabulated in Table 9. The loops are not categorized according to interstitial or vacancy types, but most are believed to be of vacancy nature.[137] At first glance it may appear contradictory to the DXS study, which showed that interstitial loops are greater in number than vacancy loops below the temperature at which vacancies become mobile, but this is due largely to the interstitials migrating to the surface of the thin TEM specimens. It deserves mention moreover, that some controversy has existed whether the loops formed dynamically in cascades were all of vacancy character. Careful investigations on Cu samples irradiated with 40 or 80 keV Kr have shown that those loops that can be unambiguously identified by contrast analysis, $\approx 50\%$, are indeed vacancy loops, but that many loops could not be identified by this method.[137] A new, unpublished TEM study now indicates that some loops are, in fact, interstitial in character.[138] The identification was made by in situ imaging of loops produced during 600 keV self-bombardment of Cu at ≈ 20 K and noting whether the loops grew or shrank upon annealing to ≈ 100 K. Between 40 and 100 K, interstitials are mobile, but vacancies are not. The fraction of loops produced with intersti-

[136] M. L. Jenkins, *J. Nucl. Mater.* **216**, 124 (1994).
[137] H. Fukushima, M. L. Jenkins, and M. A. Kirk, *Philos. Mag. A*, **75**, 1583 (1997).
[138] M. A. Kirk, M. L. Jenkins and H. Fukushima (private communication).

TABLE 9. SELECTED DATA ON LOOP FORMATION IN METALS

METAL	ION E (keV)	TEMPERATURE (K)	Y	ξ
Ti	Ti < 100	300	0.0	
V	W, 80	300	0.12 ± 0.01	0.20 ± 0.05
	Sb, 100	300	0.07	0.19 ± 0.02
Fe	Fe, 80–240	300	0.0	
	W, 80	300	0.18 ± 0.05	
Ni	Ni, 80	300	0.44 ± 0.05	0.25
	Ni, 50	30	0.05	
	Ni, 50	300	0.14	
	Ni, 100	300	0.07 ± 0.01	
Cu	Cu, 30–50	300	0.50 ± 0.01	0.36 ± 0.02
	W, 30	300	0.6 ± 0.01	0.71 ± 0.02
	Cu, 50	30	0.25	
Cu_3Au	Cu, 50	30	0.53 ± 0.05	
	Cu, 100	30	0.49 ± 0.04	
Mo	Mo, 60	300	0.12 ± 0.02	0.36 ± 0.02
Ru	Ru, 50	300	0.19 ± 0.02	
Ag	Ag, 30	300	0.55	
	Ag, 50	300	0.95	
Au	Au, 70	300	1.0	

Source: Data from M. L. Jenkins, M. A. Kirk, and W. J. Phythian, *J. Nucl. Mater.* **205**, 16 (1993); and C. A. English and M. L. Jenkins, *Mater. Sci. Forum* **15/18**, 1003 (1987); and STP 1125, ed. R. E. Stoller, A. S. Kumar, and D. S. Gelles, ASTM, Philadelphia (1992), p. 375.

tial character has not yet been determined. The TEM studies can be summarized as follows:[139,140]

1. Y tends to increase with increasing energy density in the cascades.
2. Y and ξ_{TEM} tend to increase with decreasing melting temperature.
3. Loops form on close-packed planes. For face-centered-cubic metals, loops can be faulted, perfect, or stacking fault tetrahedra.
4. Loops are observed after irradiation (and observation) at 30 K in Cu_3Au, Cu, Ni, Au, and Ag. The yields, however, are typically a factor of 2 to 3 smaller than corresponding yields for irradiation at 300 K. For Cu_3Au the yields observed at 30 K do not appreciably change upon annealing to room temperature, but for Cu and Ni, new loops do appear on warming.

[139] M. L. Jenkins, M. A. Kirk, and W. J. Phythian, *J. Nucl. Mater.* **205**, 16 (1993).
[140] C. A. English and M. L. Jenkins, *Mater. Sci. Forum*, **15/18**, 1003 (1987).

5. Loops in Cu and Ni undergo agglomeration, dissolution, and reorientation reactions at higher doses due to overlapping damage.

6. Although not shown in the table, alloying additions, even at low concentration, can have large influences on Y and ξ_{TEM}.

Most of these conclusions support the ideas of cascade collapse suggested by MD simulations. Recall that it was proposed that cascade collapse is driven by the kinetics of resolidification, whereby free volume (vacancies) is swept along with the solid–liquid front in the retracting melt. The observation that loops form during bombardment at 30 K clearly demonstrates that cascade collapse is a dynamic process, occurring on the time scale of the cascade lifetime. Since this mechanism is most efficient when thermal spike behavior is pronounced, the defect yield is largest in materials with high energy densities and low melting temperatures. A strong correlation between loop formation and ion beam mixing is thus observed.

The finding that the yields are lower at 30 K than at 300 K indicate that cascade dynamics may be influenced by the ambient temperature. Whether these differences can be attributed to dynamic cascade effects as compared to simply vacancies becoming mobile and clustering at high temperatures is uncertain. Loop formation in Cu_3Au, however, is significant since irradiation at 30 K and subsequent observation at 300 K produced a smaller yield than irradiation at 300 K, indicating that at least in this alloy the dynamic effect is important. On the other hand, the loop yields in Cu and Ni were observed to increase on warming specimens from 30 K to room temperature.

The observation that loops can agglomerate, reorient, or even disappear upon further irradiation has a natural interpretation within the resolidification model of loop formation. When a new cascade overlaps an existing loop, the vacancies in the loop are reabsorbed into the new melt. Upon resolidification, a new loop may form with either the same or a different orientation.[141] Since loop yields are less than unity, it is also possible that no new loop forms. An MD simulation performed by overlapping a 1-keV cascade on a vacancy loop containing 19 defects in Cu supports this mechanism of loop dissolution.[142]

The conclusion concerning the effects of impurities on cascade collapse will not be discussed in detail here, as no clear explanation of these effects

[141] J. S. Vetrano, I. M. Robertson, R. S. Averback, and M. A. Kirk, in Effects of Irradiation in Materials, ASTM STP 1125, ed. R. E. Stoller, A. S. Kumar, and D. S. Gelles, ASTM, Philadelphia (1992), p. 375.

[142] A. J. E. Foreman and W. J. Phythian, unpublished result.

are available. Various mechanisms, such as defocusing of RSVCs, electron–phonon coupling, and lattice stability have been suggested, but none of these possibilities have been established. These results are mentioned here, however, to indicate that much is still unknown about the collapse of loops in irradiated metals.

An important consideration in regard to the quantitative aspects of TEM experiments is the influence of the surface on loop yield. In most experiments using ion irradiation, nearly all the damage is confined to a region within 10 nm of the surface. How this may affect loop yields is discussed in Section VII. It should be stated here, however, that loops are also formed when cascades are produced in the bulk, and therefore they are not just a surface effect. This has been shown by the DXS measurements mentioned above and by TEM observations on specimens that were thinned after irradiation with fast neutrons.

d. *Radiation Annealing*

Radiation annealing experiments have been used to provide a qualitative picture of defect clustering.[143] The SRV, α, included in Eq. (6.1) refers to nonoverlapping defects. In situations where the defects are clustered, such as in cascades, Eq. (6.1) takes the form

$$\frac{dc}{d\phi} = \sigma(1 - 2\alpha_{cl}\, c), \tag{13.5}$$

where α_{cl} is average recombination volume of a defect in the cluster. The average overlap of SRVs in clusters is thus given by $1 - \alpha_{cl}/\alpha$. The experimental procedure in the radiation annealing experiments, therefore, was to irradiate samples with heavy ions to produce cascade structures, using electrical resistivity measurements to monitor the defect concentration. These same samples were subsequently irradiated with projectiles that produce isolated defects (e.g., electrons or protons), to obtain α_{cl} in Eq. (13.5). Figure 45 illustrates the results of such a study on Al, Cu and Ag using proton irradiation as the probe. Here the relative overlap is plotted as a function of defect concentration in the sample. For Ar irradiation of Al, for which the defect concentration in cascades is expected to be dilute, the SRV overlap is negligible at low concentrations of defects and then increases as cascades begin to overlap. For Cu and Ag the overlap is substantially larger. The influence of projectile mass (energy density) on defect clustering in Ag is also shown. For cascades with higher energy densities, the clustering is

[143] R. S. Averback, K. L. Merkle and L. J. Thompson, *Radiat. Eff.* **51**, 90 (1980).

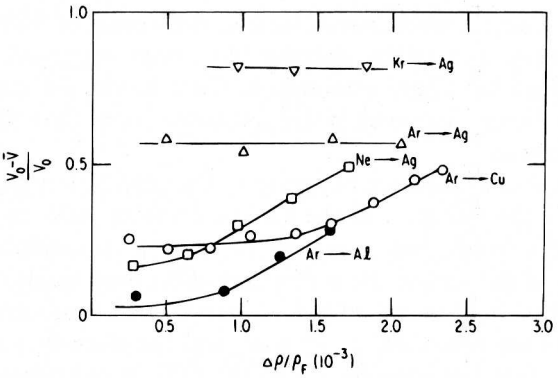

FIG. 45. Average overlap of SRVs in cascades plotted as a function of ion dose. (After Ref. 142.)

greater, as expected. These data reflect the same dependence on ion mass as revealed by the FIM experiments represented in Fig. 41. Of particular note is the relative overlap value of ≈ 0.8 for Kr irradiation of Ag. This value is observed even before the cascades have significantly overlapped. Since the relative overlap volume is greater than 0.5, it means that both vacancies and interstitials atoms are both highly clustered, presumably in the form of dislocation loops.

e. *Silicon*

In Si the structure of the cascade has been studied extensively using TEM and HRTEM after low-energy heavy ion irradiation at low temperature. Howe and Rainville[144] showed that bombardment of Si with As, Sb, or Bi ions to low doses at 50 K produced visible damage zones with an average diameter of 3.0 to 5.0 nm and that these zones were amorphous regions embedded within the crystalline matrix. For irradiation conditions where the cascade energy densities were in excess of 0.4 eV/atom, Howe and Rainville found that the yield for producing amorphous zones was 0.7 to 1.0. These authors also observed that as the cascade energy density decreased toward 0.4 eV/atom, multiple amorphous zones or subcascades had formed. Light ions, such as P or Si, on the other hand, did not produce visible damage zones. Whether the size of the amorphous zones was below the resolution limit in the TEM or amorphization did not occur is unclear from the experiments.

[144] L. M. Howe and M. H. Rainville, *Nucl. Instrum. Methods* **182/183**, 143 (1981).

VIII. Effects of Surfaces and Applied Stresses on Cascades

Atomic displacement processes near surfaces are markedly different from those in the interior of the crystal because the cascade volume is no longer fully embedded in an elastic medium. This difference is not fully appreciated in BCA models. In these models, surfaces are significant only because they lead to sputtering and to altering the damage energy distribution. For this reason, most past studies of irradiated surfaces focused on sputtering. Displacement processes at surfaces, however, deserve closer examination. They are of great practical interest in such areas as sputter depth profiling, ion implantation, and other ion beam surface modifications. Moreover, they are a useful means to investigate displacement processes in cascades since surface damage is amenable to examination by atomic level probes such as scanning tunneling microscopy (STM). Sputtering experiments were previously employed for this purpose[54]; however, they only probe ballistic effects that occur early in the cascade evolution. The present sections on surface damage and the effects of applied stresses will illustrate that in many situations, ballistic events have a negligible effect on displacement processes in comparison to the collective response of the solid.

14. MD Simulations of Ion Impacts on Surfaces

Sigmund has classified sputtering mechanisms according to different regimes of energy density.[145] This same scheme is useful for describing displacement processes at surfaces more generally. The relevant damage processes in each of these regimes are sketched in Fig. 46.

a. *Linear Cascades: Ballistic Ejection of Adatoms*

One means for creating damage during ion bombardment is by the ballistic ejection of atoms onto the surface as illustrated in Fig. 46a. This mechanism is similar to that for sputtering and for defect production as described in the BCA. Displacement energies for producing an adatom–vacancy pair, however, are expected to be considerably smaller than those for Frenkel pair production, since the adatom need not be displaced far from its vacancy. Although no MD simulations have yet focused specifically on this linear regime of surface damage, a study of 4.5-keV Ne bombardment of Pt illustrates the main effects. Shown in Fig. 47(a), are the locations of

[145] P. Sigmund, in Sputtering by Particle Bombardment, ed. R. Behrisch, Springer, Verlag, Berlin (1981).

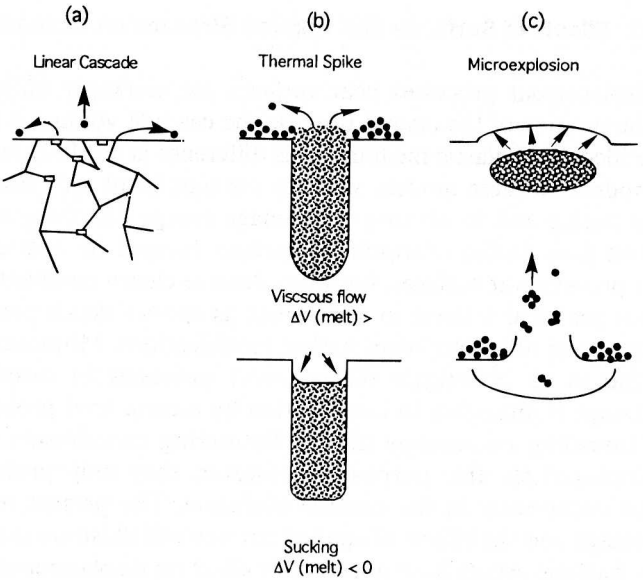

FIG. 46. Schematic diagram illustrating the different types of damage produced near surfaces: (a) linear cascades; (b) viscous flow; (c) microexplosions.

adatoms and surface vacancies on Pt(111) following Ne impact. Adatoms appear either in isolation or in a cluster of two. Detailed analysis of this and similar events showed that the adatoms were produced by RCSs or by direct ejection. Values for the adatom yield, Y_{ad}, and sputtering yield, Y_s, are listed in Table 10. The observation that $Y_{ad} \approx 3Y_s$ indicates that the

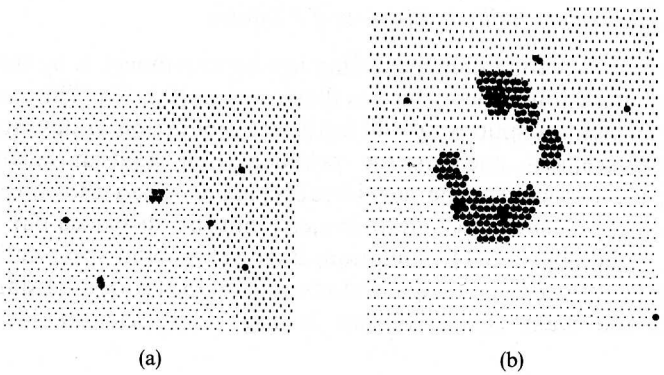

FIG. 47. (a) Locations of adatoms on Pt(111) produced by a 4.5-keV Ne ion impact during MD simulation; (b) 4.5-keV Xe is shown for comparison. (After Ref. 147.)

TABLE 10. SUMMARY OF THE DATA ON ADATOM PRODUCTION IN Pt

ION ENERGY keV	Y_{ad}	σ	Y_{ad}/Y_s	VACANCY	INTERIOR
Ne (4.5 keV), expt.	4 ± 0.2	2.0	1.4		
Ne (4.5 keV), MD	5 ± 1.1	2.5	2.5	9.6	2.4
Ar (4.5 keV), expt.	11	5	2.7		
Kr (4.5 keV), expt.	25	14	3.6		
Xe (4.5 keV), expt.	34 ± 4	26	4.5		
Xe (4.5 keV), MD	58 ± 14	40	7.6		

Source: Experimental data from M. Morgenstern, Ph.D. thesis, Universitat Köln.; M. Morganstern, T. Michely, and G. Comsa, unpublished result; MD simulation data from M. Ghaly and R. S. Averback, unpublished result.

characteristic energy for adatom production is approximately one-third of the surface binding energy, or just a few eV. The threshold energy for Frenkel pair production in Pt, in contrast, is 44 eV.

b. *Thermal Spikes: Viscous Flow*

The local heating in cascades in the bulk was shown to cause local melting and extensive cavitation. Some evidence for plastic deformation was already mentioned, but most plastic flow is prevented by the surrounding elastic matrix. This constraint is removed at the surface, so that hot liquid can flow as sketched in Fig. 46b. A simple calculation based on the thermal spike model described in Section 4 illustrates the magnitude of this effect and how the flow varies with different irradiation parameters.

The calculation[146] assumes that the ion deposits its energy along a straight track normal to the surface according to

$$F_D(r, z) = F_D^0 \, \delta(r), \tag{14.1}$$

where $F_D^0 (= dE_D/dx)$ specifies the damage energy deposition. The energy spreads radially outward and melts the surrounding crystal, creating pressure inside the expanding cylinder. Flow of material is described by Poiseuille's equation for viscous flow. The number of atoms passing through the surface, dq, within a time, $d\tau$, is given by

$$dq = N_0 v A \, d\tau, \tag{14.2}$$

[146] R. S. Averback and M. Ghaly, *Appl. Phys. Lett.* **76**, 3908 (1994).

where v is their velocity and $A = \pi r^2$ is the cross-sectional area of the expanding cylinder of melt. The instantaneous radius of the melt cylinder varies with time as

$$r^2 = 4D\tau, \tag{14.3}$$

where D is the thermal diffusivity. The cylinder reaches its maximum extent when

$$r_m^2 = \frac{F_D^0}{\pi n_0 \varepsilon_m}, \tag{14.4}$$

where ε_m is the energy per atom in the liquid at the melting temperature. The flow velocity is obtained from Poiseuille's equation,

$$v = \frac{r^2 \Delta P}{8\mu l}, \tag{14.5}$$

where ΔP is the pressure difference between the surface and the liquid at depth, l and μ is the viscosity of the liquid metal. The pressure created in the cylinder is approximated by assuming that the liquid has uniformly expanded against the surrounding elastic matrix, for which

$$\Delta P = \frac{-\Delta N_0/\kappa N_0}{1 + [2(1+\nu)/E\kappa]}, \tag{14.6}$$

where $-\Delta N_0/N_0$ is the fractional change in volume owing to thermal expansion and melting, E is the elastic modulus, ν is Poisson's ratio, and κ is the compressibility of the liquid. Integration of Eq. (14.2) leads to the result,

$$Q = \frac{1}{8\pi}\left[\frac{(\Delta N_0/N_0)^2/\kappa}{\mu D(1 + [2(1+\nu)/E\kappa])}\right]^{1/2}\left(\frac{F_D^0}{\varepsilon_m}\right)^2. \tag{14.7}$$

Typical of most thermal spike models, the viscous flow depends on the thermal diffusivity, damage energy density, and energy per atom in the melt. It also varies, however, with the volume expansion on heating. Since the sputtering yield depends linearly on F_D^0/ε_m, Eq. (14.7) indicates that the ratio of flow to sputtering yield should be an increasing function of this ratio. The dependence of flow on the molar volume of melting is also of interest. For most metals this quantity is positive, so that the cascade pressure will force hot liquid onto the surface. Volume changes on heating from

room temperature to above the melting temperature are typically ≈ 10 to 15% (5% is due to melting and 5 to 10% due to thermal expansion). In semiconductors like Si and Ge, the molar volume of melting is negative (-10% for Ge and -5% for Si) and thermal expansion in these solids is smaller than in metals. Consequently, little or no effect is expected in these materials.

The general trends of this model have been verified by computer simulation.[147] Figure 48 illustrates the effect for 10-keV self-bombardment of Au. Here cross-sectional views of atom locations are plotted at various instants of time. The surface event begins very similarly to the bulk event illustrated in Fig. 28. Rapid heating of the cascade region takes place, which is accompanied by cavitation near the center of energy. Temperature and pressure

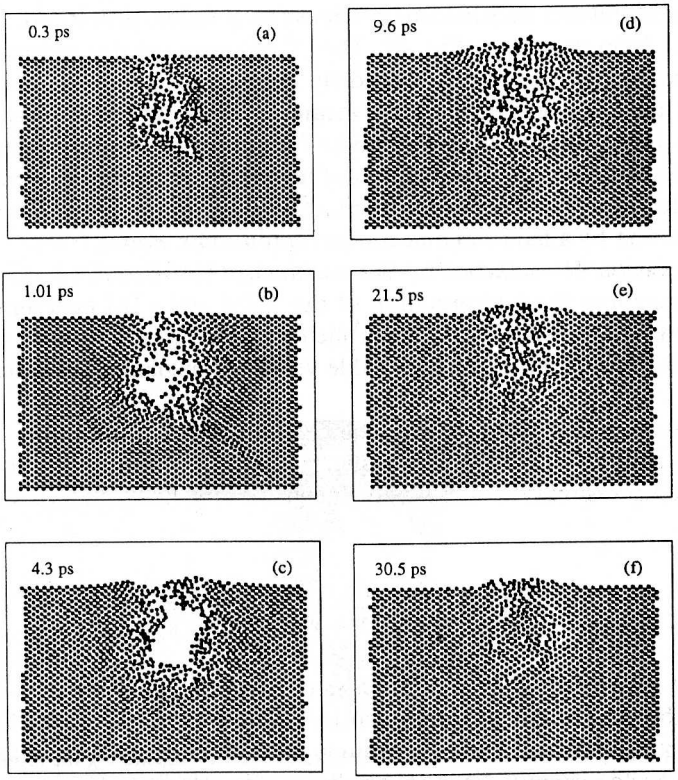

FIG. 48. MD simulation of 10-keV self-atom impact on Au(100). Atoms in a cross-sectional slab of thickness $a_0/2$ are shown at various instants of time. (After Ref. 146.)

[147] M. Ghaly and R. S. Averback, *Phys. Rev. Lett.* **72**, 364 (1994).

profiles for this event are similar to those plotted in Fig. 29 for a bulk event, illustrating the same extreme thermal conditions within the spike. As the energy dissipates into the surrounding crystal, the cavitation collapses and the cascade melt becomes more uniform. It is during this later period of time that most of the mass flows onto the surface. The cooling phase is marked by a similar resolidification process that was observed in the crystal interior. In this case, however, many of the atoms that had flowed onto the surface remain there. As a consequence, many vacant lattice sites are left below the surface, and the stress state switches from compressive to tensile. Similar flow behavior was observed in Pt and Cu, although the effects were smaller, as expected from Eq. (14.7).[148]

A total of 550 adatoms were created in the event just described, leaving an equal number of vacancies below the surface. These vacancies are in high concentrations and tend to condense into dislocation loops. Evidence of such a loop is seen in Fig. 49. The effectiveness of this mechanism for producing vacancies can be realized by noting that a similar 10-keV MD event in the bulk created only 20 vacancies as illustrated in Fig. 28 (The Kinchin–Pease value is 111). Two 15-keV events of self-bombardment of Cu yielded an average of 49 adatoms on the surface. Although this number is far smaller than that for the Au event, it nevertheless increases the vacancy concentration by a factor of 3 in comparison to bulk events.

The creation of vacancies by the mechanism just described raises questions concerning the interpretation of the TEM and FIM experiments discussed previously. Most TEM experiments employ irradiations of very thin films with 10 to 70-keV ions (see Table 9); so the displacement cascades are

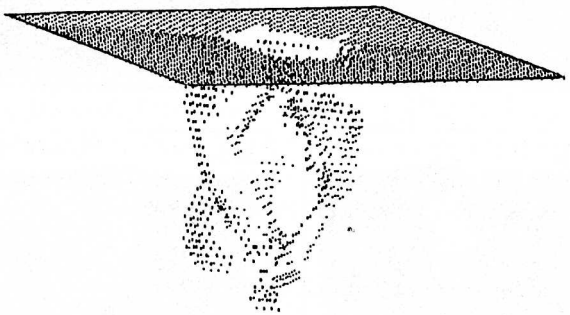

FIG. 49. Locations of atoms with potential energies >0.4 eV illustrating the formation of a complex dislocation during 10-keV self-bombardment of Au. (After Ref. 146.)

[148] M. Ghaly, R. S. Averback, H. Zhu, L. Marques, M. J. Caturla and T. Diaz de la Rubia, *Mater. Res. Soc. Symp. Proc.* **396**, 3 (1996); M. Ghaly, K. Nordlund and R. S. Averback, *Philos. Mag.*, submitted.

initiated in a region between the surface and a depth of 10 to 20 nm. It is almost certain that some of the loops observed in these studies are influenced by the surface effect described here. For example, Merkle and Jäger irradiated Au with 10-keV Bi and reported a high yield for loop production (0.25) and a high efficiency $\xi_{TEM} \approx 1$.[149] The simulations show unambiguously that these results are influenced by surfaces. Most damage studies employing TEM methods, however, have used projectiles with energies higher than 10 keV, and the extent to which the damage structures for these are influenced by the surface phenomenon described here is still unknown. On the one hand, the stopping power is an increasing function of energy in these experiments, which according to Eq. (14.7), enhances the surface effect, while on the other hand, a greater fraction of the damage is deposited deeper in the sample. Effort is currently being focused on this question, but no conclusions are yet available.

The present simulations also have bearing for the high defect production efficiencies observed in Pt and W using FIM methods. For example, in two 10-keV MD simulation events of self-bombardment in Pt, an average of 102 vacancies were produced, while in 10-keV bulk events, an average of only 9 vacancies were obtained. Since W is far more refractory than Pt, the effects of surface flow are expected to be much smaller, Eq. (14.7) indicates by a factor of ≈ 4. Nevertheless, even if only half of the vacancies observed in the FIM experiments on W were produced by surface flow, as the analysis using Eq. (14.7) suggests, the defect production efficiency in this metal would approach those of other metals, and that obtained by the electrical resistivity measurements on irradiated W.

MD simulations of surface events in Si and Ge reveal far different behavior.[150] As illustrated in Fig. 46b, no outward flow is expected. Simulations of 15-keV Pt and 10-keV As in Si, and 5- and 10-keV self-bombardment of Ge, indeed, show no evidence for it. Figure 50, for example, shows the first few atomic planes of Ge in a MD simulation of 10-keV self-bombardment. The bending of these planes inward from the surface illustrates the negative volume change on melting. It also reflects a fundamental difference in behavior of cascades in metals and semiconductors.

c. *High-Energy Densities: Microexplosions*

Microexplosions are the third type of surface damage mechanism sketched in Fig. 46(c). This mechanism was suggested by Merkle and Jäger to explain

[149] W. Jäger and K. L. Merkle, *Philos. Mag. A* **57**, 479 (1988).

[150] M. Ghaly, R. S. Averback, and T. Diaz de la Rubia, unpublished results.

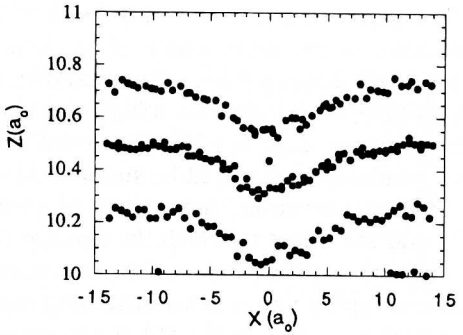

FIG. 50. MD simulation of 10-keV self-bombardment of Ge(100), showing the inward bending of surface planes. (After Ref. 149.)

their TEM observations of large craters in Bi-irradiated Au (see Section 15c).[151] The dynamics of a microexplosion is illustrated in Fig. 51, where snapshots from a 20 keV event in Au is shown at different stages of evolution.[147] Similar events were observed in MD simulations of 10-keV self-bombardment of Pt. It is clear from this figure that the center of energy must be located very close to the surface for the pressure wave to rupture the surface. This event also provides insight about sputtering mechanisms in dense cascades. Previous calculations of thermal spike sputtering simply estimated sputtering yields by integrating the evaporation rate from the surface over the lifetime of the cascade using an equation similar to Eq. (6.4). The current simulations illustrate that such an approach has little physical basis and that thermal spike sputtering involves an explosive ejection of both atoms and clusters from the near-surface region. In the event shown, 75% of the atoms evolved from lattice sites initially located below the surface layer. This mechanism would also appear to explain how clusters of atoms can be emitted from ion-bombarded surfaces.[152]

The event shown in Fig. 51 is certainly not typical of 20-keV self-bombardment of Au since the sputtering yield in this event is nearly 10 times larger than that measured. Unfortunately, no statistics for this type of an event are available, although it was remarked in Ref. 146 that several events were initiated before the one shown in Fig. 51 was found. The variability of damage structures produced at the surface results from the sensitivity of the damage to the penetration depth of the ion. Figure 52

[151] K. L. Merkle and W. Jäger, *Philos. Mag. A* **44**, 741 (1981).

[152] See, e.g., S. R. Coon, W. F. Callaway and M. J. Pellin, *Nucl. Instrum. Methods B* **90**, 518 (1994).

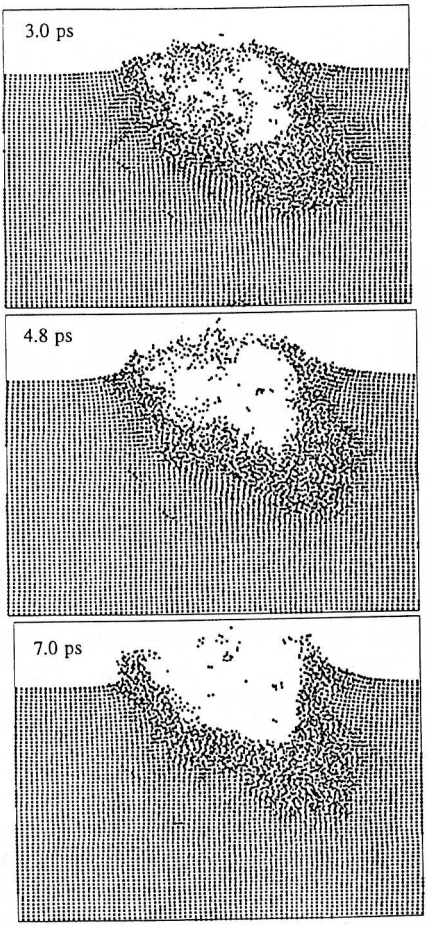

FIG. 51. MD simulation of 20 keV self-atom impact on Au(100). Atoms in a cross-sectional slab of thickness $a_0/2$ are shown at three instants of time. (After Ref. 146.)

illustrates, for example, the various types of behavior produced by 10-keV events in Pt.[148]

15. EXPERIMENTAL INVESTIGATIONS OF ION IMPACTS ON SURFACES

Surface damage structures such as the ones depicted above are readily observable using STM methods. The experiments are difficult, however, since adatoms are mobile on metal surfaces at room temperature. The experiments thus require in situ irradiation at low temperatures to preserve

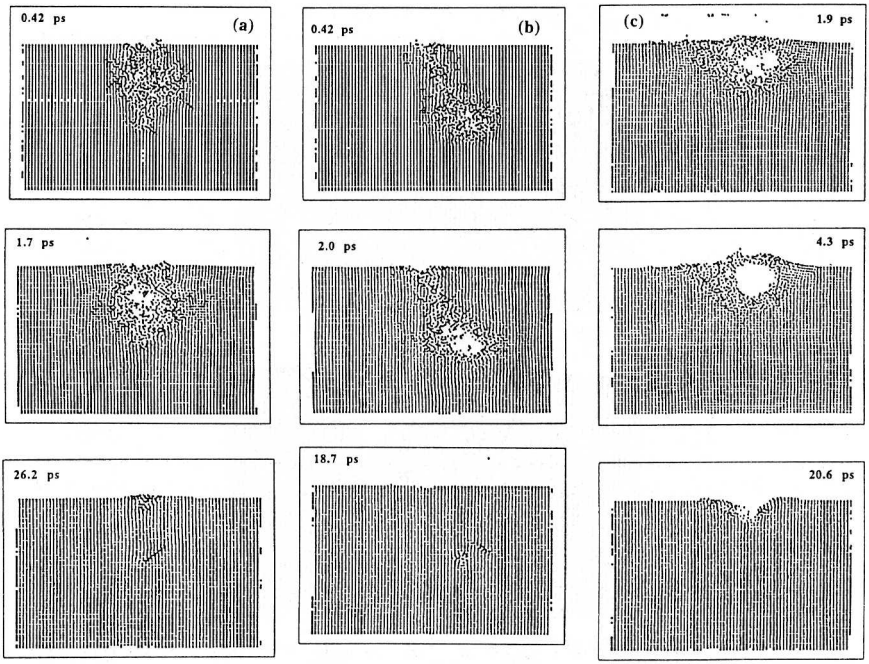

FIG. 52. MD simulation of 10-keV self-bombardment of Pt(100), illustrating the wide range of behaviors produced for nearly identical events. The angle of incidence was slightly varied from one event to the next. (After Ref. 147.)

the primary state of damage. Morgenstern and co-workers have performed such experiments to study ion impacts of Pt(111) and Au(111) surfaces for energies up to 13.5 keV.[153] Their experiments on Pt were performed at temperatures below ≈ 80 K, which is sufficiently low to suppress adatom migration, which occurs at 110 K,[154] but not interstitial atom migration, which occurs at 22 K (see Table 11).

a. *Linear Cascade Regime*

Figure 53a–d show gray-scale images of the Pt(111) surface after bombardment with 4.5-keV Ne, Ar, Kr, and Xe ions, respectively.[153] A comparison of the ion dose with the number of surface features shows that each ion

[153] M. Morgenstern, Ph.D. thesis, Universität Köln.; M. Morganstern, T. Michely, and G. Comsa, *Philos. Mag.*, submitted.

[154] M. Bott, M. Hohage, M. Morgenstern, T. Michely and G. Cosma, *Phys. Rev. Lett.* **76**, 1304 (1995).

TABLE 11. PROPERTIES OF POINT DEFECTS IN METALS

METAL	ΔH_I^m (eV)	T_I (K)	ΔV_I^{rel} (Ω_0)	ΔH_v^m (eV)	T_v (K)	ΔV_v^{rel} (Ω_0)
Ag	0.88	28		0.66	250	
Al	0.115	35	1.9	0.59	220	−0.05
Au		<0.3		0.71	310	−0.15
Co	0.14	55	1.5			
Cu	0.117	38	1.55	0.70	270	−0.25
Fe	0.27	120	1.1	0.55	220	−0.05
Mo	0.083	33	1.1	1.3	500	−0.1
Nb		<8		0.54		
Ni	0.15	56	1.8	1.04	400	−0.2
Pb	0.01	4		0.43		
Pt	0.063	22	1.8	1.43	580	−0.2
W	0.054	27		1.7	650	
Zr	0.26	102	0.6			−0.05

Source: Data from P. Ehrhart, K.-H. Robrock, and H. R. Schober, in Physics of Radiation Effects in Crystals, ed. R. A. Johnson and A. N. Orlov, North-Holland, Amsterdam (1986).

creates one imagable damage zone. For the Ne irradiations, an average of four adatoms per incident ion was obtained. No clustering of the adatoms was observed, which agrees with the conclusion from MD simulation that the adatoms are produced in nearly linear cascades. Morgenstern *et al.* also reported that the number distribution per incident ion was closely represented by a Poisson distribution, which they noted is further indication that the adatoms were produced in isolated recoil events. The results of the experiments[153] and simulations[155] are compared in Table 10. Both the sputtering yields and adatom production are in good agreement.

b. *Thermal Spike Regime*

The surface features produced by 4.5-keV Ar, Kr, and Xe bombardment differ markedly from those produced by Ne bombardment. First, the yield increases monotonically with incident ion mass, the adatoms are no longer isolated but clustered, and small vacancy clusters or craters are identified with each impact. The size of the vacancy clusters also grow with increasing ion mass. These data are compiled in Table 10. These observations find qualitative agreement with the predictions of the MD simulations. It should be noted that the increasing adatom yield is partially explained by the

[155] M. Ghaly and R. S. Averback, unpublished results.

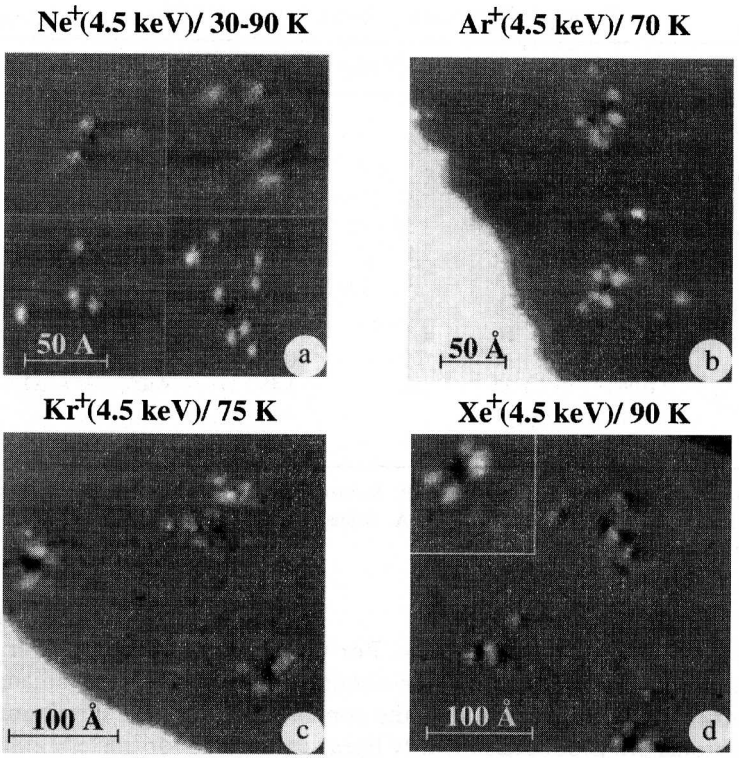

FIG. 53. STM images of Pt(111) following impacts with 4.5-keV ions: (a) Ne; (b) Ar; (c) Kr; (d) Xe. (After Ref. 152.)

shorter ranges of the heavier particles, and consequently, more damage energy deposition near the surface. The sputtering yields shown in the table increase precisely for this reason, as sputtering varies linearly with the nuclear stopping power. It is significant, however, that the ratios of the adatom yields to the sputtering yields also increase with increasing ion mass, illustrating that the adatom yield increases faster than linearly with energy density. This is found in the simulations as well and predicted by the thermal spike model, Eq. (14.7). Quantitative comparison of the STM and MD results listed in Table 10 shows that sputtering yields are again in good agreement, but the adatom yields from the simulations are a factor of $\sim 50\%$ larger. The reasonable agreement illustrates that no large errors are introduced in the MD simulations by deficiencies in the interatomic potentials or by neglect of electron–phonon coupling. This is an important result, since electron–phonon coupling should be important in Pt. In Cu

and Au, for which other comparisons between experiments and simulations were performed, electron-phonon coupling is known to be weak.

c. *Microexplosions*

Although the results for Xe bombardment of Pt were interpreted as thermal spike behavior, the large vacancy clusters observed in the surface layer (Fig. 53d) suggest that some microexplosions may also have occurred. STM images of Au(111) following 13.5-keV Xe bombardment showed more dramatic effects of microexplosions with yields of some impacts as high as 200 adatoms and with large surface craters.[153] Other STM evidence for microexplosions is observed in Fig. 54, where a crater produced during 20-keV Ga bombardment of Ge(100) is shown.[156] The probability of forming these craters, however, was found to be very low, $\approx 5 \times 10^{-4}$. Nevertheless, the observation of crater formation in Ge illustrates that microexplosions must result from the pressure wave emanating from the cascade early in the cascade evolution, since after the pressure wave, the stress state in Ge switches to tensile, as noted above.

Evidence for microexplosions was first reported for energetic Bi_2 irradiation of Au using TEM.[151] In some cases, debris from exfoliation was observed attached to the crater. Merkle and Jäger[151] explained these craters by assuming that the pressures developed in cascades just below the surface were sufficient to cause rupture. This interpretation agrees with the MD simulations. The probability of creating large craters in Au ranged between 0.1% and 1% in these experiments, depending on the irradiation

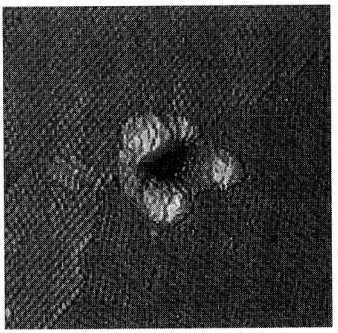

FIG. 54. STM image of Ge(100) following bombardment with 20-keV Ga ions. (After Ref. 156.)

[156] Reprinted from P. Bellon, S. J. Chey, J. E. Van Nostrand, M. Ghaly, D. G. Cahil, and R. S. Averbeck, *Surf. Sci.* **339**, 135 (1995) with kind permission from Elsevier Science–NL, Sara Burgerhartstraat 25, 1055 KV, Amsterdam, The Netherlands.

conditions, hence, they also illustrate that the conditions for micro-explosions and rarely obtained.

16. Effect of Applied Stresses on Cascade Dynamics

In most materials, the high pressures developed in cascades do not cause plastic deformation. This is largely because the stress state in a spherical cascade is nearly hydrostatic. Trinkaus[157] and Wolfer[158] have calculated that under these conditions the pressure would need to exceed $\approx 0.7\ \mu$ (μ = shear modulus) for loop punching to occur. Nevertheless, materials are often subjected to external shear stresses during irradiation. Common examples are the stresses developed in surface layers during irradiation-induced phase transitions and implantation of excess atoms. In some cases it has been found irradiation can also induce stress relaxation. Although viscous flow at the surface is one possible mechanism to explain stress relaxation in very thin films, other mechanisms are required in thicker films and in the bulk.

Volkert has measured the stress that develops in Si during irradiation to high doses with 2-MeV Xe. The average stress, S, which was determined from measurements of wafer curvature, is shown in Fig. 55a plotted as a function of ion dose. Here

$$S = \int_0^{t_d} \sigma(x)\, dx = \int_0^{t_d} Y_d(x)\varepsilon_{in}(x)\, dx = Y_d\, \varepsilon_{in}\, t_d, \tag{16.1}$$

where $\sigma(x)$ is the local stress, $Y_d(x)$ the biaxial modulus, $\varepsilon_{in}(x)$ the in-plane strain, t_d the thickness of the implanted layer, and x the depth below the surface.[159] The data illustrate that the in-plane stress increases with dose at low doses, reaches a maximum, and then decays at still higher doses. As observed in the figure, the maximum average stresses is quite high, ≈ 100 MPa. The initial portion of this curve is understood simply in terms of the positive volume change on creating defects during amorphization of Si. Hence the surface region is placed in a state of compression, $S > 0$. After the sample has fully amorphized, the specimens undergo stress relaxation upon continued irradiation. It is this viscoelastic response that is of interest here. In Fig. 55(b) relaxations of amorphous Si during irradation from a pre-set level of stress is shown. From these data the irradiation-induced

[157] H. Trinkaus, *Radiat. Eff.* **78**, 189 (1983).
[158] W. G. Wolfer, *Philos. Mag. A* **58**, 285 (1988).
[159] C. A. Volkert, *J. Appl. Phys.* **70**, 3522 (1991).

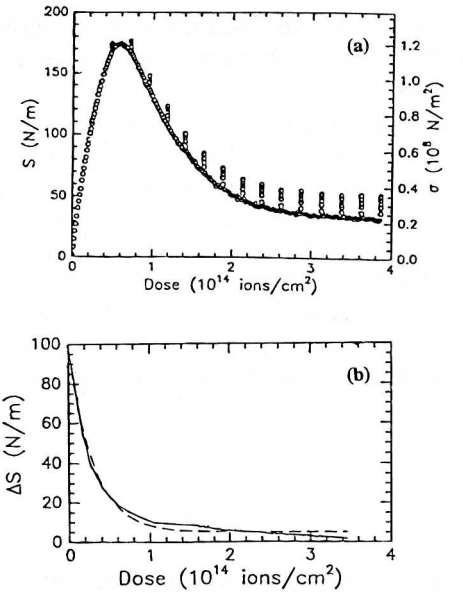

FIG. 55. (a) Integrated in-plane compressive stress in Si during irradiation with 2-MeV Xe. The average compressive stress in the implanted region is indicated on the right-hand axis. (b) Stress relaxation of amorphous Si. Dashed lines is a fitting curve. (After Ref. 158.)

viscosity, η, has been obtaining using the expression[159]

$$\frac{\mathrm{d}\,\Delta S}{\mathrm{d}\Phi} = -\frac{Y_d}{6\dot{\Phi}\eta}\,\Delta S, \tag{16.2}$$

where Φ is the ion dose and $\dot{\Phi}$ is the ion flux. A value of $\eta \approx 10^{13}$ N·s/m^2, was obtained, which is intermediate between that of a liquid and solid. The value of η, of course, will vary with ion flux.

Irradiation-enhanced creep has been well studied in metals under irradiation at high temperatures and is understood in terms of the flow of vacancies and interstitials to favorably oriented dislocations.[160] This model is not appropriate here for amorphous materials, especially since the same behavior was observed during irradiation at $\approx$100 K,[159] where it is nearly certain that thermally activated diffusion processes are suppressed. Similar behavior has now also been observed in metallic glasses as well, and also at $\approx$100 K.[161] The viscoelastic behavior, therefore, seems clearly associated

[160] See, e.g., P. T. Heald and M. V. Speight, *Philos. Mag.* **31**, 885 (1975).
[161] L.-M. Wang and R. S. Averback, unpublished result.

with the displacement process in cascades, as first suggested by Volkert[159] and Barbu *et al.*[162] Trinkaus, however, has provided a more thorough account of this process.[163]

The central idea of the Trinkaus model of stress relaxation is that the volume of the cascade undergoes local melting, allowing the atoms to respond to the applied stress on the time scale of the local excitation. As noted by Trinkaus, the response occurs in the time required for a radial sound wave to travel across the cascade, which is shorter than the lifetime of the melt. After relaxation, the new strain, ε^{rel}, is frozen in. The amount of strain that develops in the cascade was obtained using elasticity theory. For a spherical inclusion of vanishingly small shear modulus, embedded in a matrix with a shear modulus, μ, the strain is proportional to the applied stress:

$$\varepsilon^{\text{rel}} = \frac{B\sigma^A}{2\mu}, \tag{16.3}$$

where ε^{rel} is the strain required for complete stress relaxation, σ^A the applied stress, μ the shear modulus of the matrix, and B is a constant determined from elasticity theory [$B = 15(1 - \nu)/(7 - 5\nu)$ for spherical cascades]. The macroscopic strain rate is then obtained simply by multiplying the microscopic strain in each cascade with the rate of introduction of cascades:

$$\dot{\varepsilon} = \varepsilon^{\text{rel}} \frac{V}{Q} \dot{\Phi} \frac{\mathrm{d}E_D}{\mathrm{d}x}, \tag{16.4}$$

where Q is the heat content in each cascade and $\Phi(dE_D/dx)$ is the introduction rate of damage energy per unit volume. V represents the maximum volume of a cascade containing energy Q that maintains the local temperature above the "flow" temperature in a glass, $\approx T_m$ [see, e.g., Eq. (4.3)]. With the definition $\eta_{\text{eff}} = \sigma/2\dot{\varepsilon}$, the effective viscosity is obtained from

$$\mu\eta_{\text{eff}}^{-1} = \dot{\Phi} B \frac{V}{Q} \frac{\mathrm{d}E_D}{\mathrm{d}x}. \tag{16.5}$$

[162] A. Barbu, M. Bibole, R. le Hazit, S. Bouffard, and J. C. Ramillon, *J. Nucl. Mater.* **165**, 217 (1989).

[163] H. Trinkaus, *J. Nucl. Mater.* **223**, 196 (1995); H. Trinkaus and A. I. Ryazanov, *Phys. Rev. Lett.* **74**, 5072 (1995).

Equation (16.5) illustrates that the rate of stress relaxation depends linearly on dE_D/dx, Φ, and V, where V varies at $\Delta T = T_m - T_0$ (T_0 is the ambient temperature of the specimen). From Eq. (16.5) a normalized fluidity was defined,

$$H = \frac{\mu}{\dot{\Phi}(dE_D/dx)\eta_{\text{eff}}}. \tag{16.6}$$

For materials with $T_m \approx 1300$ K and $\nu \approx 1/3$, $H \approx 2 \times 10^{-10}$ m^3/J. Few experiments have been performed to test this model; however, comparing the fluidity derived in Eq. (16.6) with that deduced from Volkert's experiments yields the correct magnitude.

For crystalline materials, Trinkaus suggested that the same mechanism cannot be applied, owing to the requirement of conserving lattice sites upon crystallization. Nevertheless, stress relaxation has been observed in crystalline materials. Volkert and Polman, for example, have reported stress relaxation in Al films deposited on a Si substrate and irradiated with 700-keV Xe.[164] The stress relaxation observed in crystalline materials could arise by the same type of mass reorganization observed in amorphous materials if dislocation were created in the once-melted zone, with the vacancy and interstitial character of each arranged to relieve stress. This may occur, for example, during the condensation of excess vacancies in the cascade core into prismatic loops, as described in Section 12. Similarly, interstitial clusters could possibly grow into aligned loops during prolonged irradiation.

IX. Freely Migrating Defects

A complete description of the evolution of the defect structures in materials subjected to prolonged irradiation in either a reactor environment or during ion implantation is the primary goal of radiation damage research but one that is far from being accomplished. The first step in this direction has been developing an understanding for the creation of the primary state of damage; that step is now well advanced. The next steps are far more difficult, owing to the many complexities that arise in moving from mesoscopic to macroscopic length scales, and no attempt will be made to treat such problems here. Advances, however have been discussed in a recent article in this series.[89] On the other hand, it would be unsatisfactory to

[164] C. A. Volkert and A. Polman, *Mat. Res. Soc. Symp. Proc.* **235**, 3 (1992).

dismiss this problem without first addressing the fate of the defects as they become mobile and leave their nascent locations. Of interest here, then, are what fractions of these defects recombine close to their creation sites and have no net effect on the subsequent microstructural development, what fraction remains immobile in clusters, and what fraction is free to migrate throughout the lattice as point defects and clusters. Two separate situations arise: the first in which the defects are created at low temperatures but are subsequently annealed at high temperatures, and the second in which the defects are created at high temperatures and begin migration immediately.

17. Metals: Defect Reactions and Annealing Stages

Much of what is known about the mobilities of point defects and their interactions with each other and with other lattice defects have been derived from annealing studies following low-temperature irradiation.[65] The simplest situation arises when electron irradiations are employed since the Frenkel pairs are then created in isolation. Defect reactions are followed as the sample is warmed to successively higher temperatures. A schematic annealing spectrum is illustrated in Fig. 56. Typically, a specimen is held a few minutes at each temperature before raising the temperature. This isochronal annealing program results in well-defined annealing stages which are typical of most pure metals. Five annealing stages are identified in the Figure.

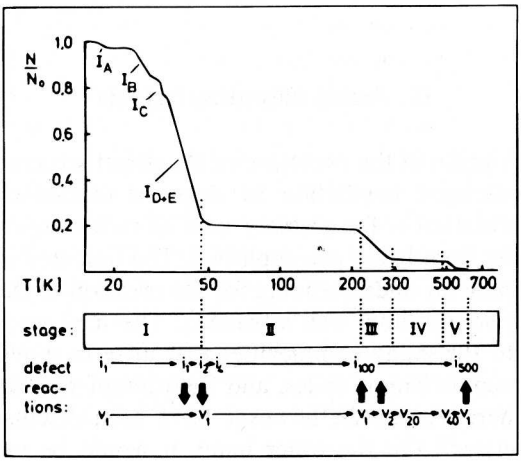

Fig. 56. Schematic isochronal annealing spectrum typical of metals following electron irradiation at 4.6 K. Clusters sizes of vacancies and interstitials are shown as a function of temperature. (Courtesy of P. Ehrhart.)

Stage I: Annealing at low temperatures is due to the migration of interstitial atoms to immobile vacancies. This first annealing stage is comprised of several substages, I_A–I_E. Recovery stages I_A–I_C are due to the collapse of different close-pair configurations of the interstitials and vacancies. The strong elastic interaction between the defects in these pairs assures their recombination. The next substage, I_D, arises from the free migration of interstitials back to their own vacancies; which is referred to as correlated recovery. Finally, I_E is due to the free migration of interstitials to distant vacancies, which were produced in different recoil events. It is observed in Table 11 that stage I_E occurs below ≈ 100 K in pure metals. In a few metals (e.g., Nb and Au) annealing is observed even at the lowest possible measuring temperatures. Recovery is not complete in stage I since freely migrating interstitials can trap at impurities or form immobile interstitial clusters before finding distant vacancies. For the current discussion, it is the fraction of freely migrating interstitials (i.e., those not recombining in stages I_A–I_D) that are of interest; for electron irradiation, this fraction is ≈ 0.35.[65]

Stage II: Recovery in stage II derives from various possible reactions: the detrapping of interstitial atoms from impurities, and interstitial–impurity complexes and small interstitial clusters becoming mobile. Interstitial clusters are observed to grow in stage II, often forming small interstitial loops. Although stage II annealing is usually complex, particularly for cascade damage where defects are produced in clusters, the defect reactions in this stage have important consequences for phase evolution. It is of vital importance, for example, whether interstitials detrap from impurities or whether they form mobile complexes with them. In the latter case, the reaction leads to radiation-induced segregation.[165] Similarly, it is critical for void swelling if the interstitial clusters collapse into prismatic dislocation loops and glide to sinks in one dimension, or whether they migrate in two or three dimensions. The growth of interstitial loops in stage II without significant loss by recombination is strong evidence for loop glide in Cu.[166]

Stage III: Vacancies become mobile in stage III ($\approx 0.25 T_m$) (see Table 11) and undergo reactions similar to those of freely migrating interstitials in stage I_E. Recovery arises from the annihilation of vacancies at interstitial clusters or defect sinks. Vacancies can also trap at impurities or form immobile clusters and loops during their migration in stage III.

Stage IV: Recovery in stage IV, like that in stage II, arises from various defect reactions. Vacancies detrap from impurities, vacancy or interstitial clusters become mobile, or small vacancy or SIA loops may glide to sinks

[165] See, e.g., P. R. Okamoto and L. E. Rehn, *J. Nucl. Mater.* **83**, 2 (1979).

[166] See, e.g., P. Ehrhart, K.-H. Robrock, and H. R. Schober, in Physics of Radiation Effects in Crystals, ed. R. A. Johnson and A. N. Orlov, North-Holland, Amsterdam (1986).

or agglomerate. Vacancies are weakly bound in small clusters and hence they can dissociate upon migration. Interstitials, on the other hand, are less likely to dissociate owing to their much higher binding energies.

Stage V: Recovery becomes complete in stage V as thermally activated self-diffusion begins and equilibrium is restored. This occurs by vacancies first dissociating from loops and annihilating interstitial loops and clusters. It is noteworthy that because the formation energies of interstitials are high, interstitial loops do not dissociate below the melting temperature. Their annihilation relies on a flux of vacancies to them.

Annealing of defects produced in cascades can be understood in terms of the reactions just described; however, the complexity of the primary state of damage in cascades and the large number of possible defect reactions prevents a clear picture to be drawn. Moreover, the large variation between damage states in different metals and alloys, and different possible recoil spectra, further hampers the formulation of a concise description of annealing stages. Nevertheless, a few general observations can be made before considering specific examples.

The efficient separation of vacancies and interstitials during the local melting leads to a strong reduction in stage I annealing. The precise amount, however, depends on the thermal spike conditions. For example, defect retention during annealing through stage I following Bi irradiation of Ag is 0.95,[167] whereas following fast neutron irradiation, it is 0.55 for Al and 0.65 for Ni and Cu.[65] The primary defect reactions in stage II are very similar to those for electron irradiation, consisting mostly of the growth of interstitial clusters and loops and recombination with vacancies. Significant differences, however, are again observed between different metals. For Cu, loops grow without much loss to recombination, whereas in Ni loops also grow but with significantly more recombination. This behavior has tentatively been explained on the basis that interstitial clusters in Cu collapse into loops at smaller sizes than they do it Ni.[168] The loops glide in one dimension and coalesce with little recombination, whereas the uncollapsed Ni clusters migrate in three dimensions, providing more opportunity for recombination with vacancies. This one very specific example illustrates the difficulty in generalizing the discussion of freely migrating defects, as it points out that the evolution of the microstructure depends sensitively on the detailed configuration of the defects, the concentrations and types of impurities, and the properties of the material. Other examples are provided below.

---

[167] R. S. Averback, K. L. Merkle, and L. J. Thompson, *J. Nucl. Mater.* **69/70**, 714 (1978).
[168] O. Bender and P. Ehrhart, *J. Phys. F.* **13**, 911 (1983).

18. Freely Migrating Defects in Metals

a. *Annealing Experiments*

Some efforts have been made to obtain the fraction of defects undergoing free migration. These fractions are usually expressed as an efficiency, ξ_{FM}, which is the ratio of the number of defects escaping recombination in their nascent cascade to the total number produced as calculated by the Kinchin–Pease model. An estimate of this number can be obtained simply by forming the product of the defect production efficiency with the defect retention above stage I. For cascade damage in Cu and Ni, $\xi_{FM} \approx \xi_{FP} \times 0.6 = 0.2$. This estimate, however, ignores the possibilities that some interstitial clusters have not yet become mobile and may still recombine in their cascades at a higher temperature, and that some interstitials have annihilated in stage I_E with vacancies in another cascade. These errors should not be large and they tend to compensate. A lower limit on ξ_{FM} was obtained by prequenching samples prior to neutron irradiation to create a large background concentration of vacancies. The idea was that all migrating defects would recombine with the added vacancies. This procedure yielded a value of $\xi_{FM} = 0.06$,[65] but it excludes all those interstitial clusters that had not yet begun to migrate. In a similar experiment, Zinkle irradiated Cu with 14-MeV neutrons above stage III. The samples were doped with impurities in an attempt to trap all migrating interstitial atoms and vacancies. These experiments yielded a value of ξ_{FM} 0.12.[169] Again this should be considered a lower bound since some recombination was inevitable.

These experiments using electrical resistivity suffer from the problem that as interstitials form loops, the Frenkel pair resistivity does not remain invariant, resulting in an underestimate in the number of defects.[168] A more direct method employs diffuse x-ray scattering where the concentrations of both vacancy and interstitial loops are measured directly. Data for Ni show that the fraction of interstitial atoms present just below stage III is $\xi_{FM} = 0.12$.[135] Moreover, the results showed that the interstitials were in large loops with radii > 1.0 nm, which means nearly all had migrated from their nascent cascades. This efficiency, too, is an underestimate since recombination in stage II is not taken into account. For Cu, this same study obtained $\xi_{FM} = 0.23$.[135] The higher yield in Cu than in Ni again reflects the smaller amount of recombination in stage II in Cu than Ni. Similar to the case for Ni, the interstitial loops in Cu were quite large. A value of $\xi_{FM} \approx$

[169] S. J. Zinkle, *J. Nucl. Mater.* **155/157**, 1201 (1988).

0.15 to 0.25 therefore appears to be a reasonable estimate, at least for Cu and Ni following fast neutron irradiation. Since $\xi_{FM} \approx 0.3$ for these metals, it means that few interstitials are captured in their nascent cascades.

b. *Radiation-Enhanced Diffusion Processes in Metals*

Attempts have been made to determine the fraction of freely migrating defects by their contribution to radiation-enhanced diffusion processes during irradiation at elevated temperatures. The first employed radiation-induced segregation for this purpose.[170] The principle of these experiments is that freely migrating interstitials produced in the sample either recombine with vacancies or flow to sinks. The latter reaction establishes a point defect flux. In Ni–Si alloys, interstitials form mobile complexes with Si solute atoms, so the interstitial flux to sinks creates a solute flux to sinks as well. For ion irradiations, the surface is the predominant sink, and hence measuring the arrival rate of Si at the alloy surface provides a measure of freely migrating interstitials. The point defect reactions, however, are sufficiently complicated that an absolute determination of ζ_{FM} is not possible by this method, but by irradiating with ions of different mass, the effect of recoil spectrum could be examined. These experiments for Ni–Si alloys revealed that ζ_{FM} for proton bombardment was 50 times larger than that for heavy ions such as Kr. Similar results were obtained for dilute Cu–Au alloys.[171] From annealing experiments it is reasonable to assume that $\zeta_{FM} \approx 0.30$ for proton irradiation, so that ζ_{FM} for heavy ions and fast neutrons would be less than 0.01. Although these experiments are important for providing an effective efficiency of freely migrating defects for this specific and important problem of solute segregation to sinks (such as grain boundaries and dislocations), they do not measure the true value of ζ_{FM}. Two problems plague these experimental determinations of ζ_{FM}. First they assume that every interstitial atom has the same effect on segregation, independent of whether it is a single interstitial, clustered interstitial, or an interstitial in a loop. This assumption is obviously not valid. It has been shown, for example, that a cluster of three or more interstitials in dilute NiSi alloys are trapped by Si and rendered immobile. These interstitials do not contribute to segregation, yet in pure Ni, such clusters are freely migrating.[172] Thus the interstitials produced in isolation by proton irradiation are effective for segregation, but the interstitial clusters produced in cascades are not. Efficiencies for freely migrating defects, therefore, depend not only on the type

[170] L. E. Rehn, P. R. Okamoto, and R. S. Averback, *Phys. Rev. B* **30**, 3073 (1984).
[171] T. Hashimoto, L. E. Rehn, and P. R. Okamoto, *Phys. Rev. B* **38**, 12868 (1988).
[172] R. S. Averback and P. Ehrhart, *J. Phys. F.* **14**, 1347 (1984).

of irradiation and the material but also on the property being measured. These experiments are further complicated by the fact that ion doses of a few tenths of dpa are required before segregation can be measured. At these large doses, a high concentration of internal sinks is created in the form of dislocations loops and clusters, and these compete with the surface for segregating solute atoms.[173,174]

Similar measurements of radiation-enhanced diffusion were performed on pure Ni and Ni-based alloys.[175,176] In these experiments, the broadening of a thin tracer layer of atoms is monitored as a function of dose. These experiments have many of the same difficulties as the segregation experiments: High doses are required and various assumptions must be included in a complex kinetic model. Effort was made in these studies, however, to account for the radiation-induced sink structure by performing TEM measurements on the samples. Absolute rather than relative values of ζ_{FM} could be obtained by this method, but with assumptions in the model. The latest result of this work on pure Ni and Ni-based alloys is that $\zeta_{FM} \approx < 0.05$.[177] This efficiency is still a factor of 2–4 less than the annealing experiments, but, considering the complications of these experiments cited above, the agreement is reasonable.

19. Freely Migrating Defects in Si: Transient-Enhanced Diffusion in Si

Implanted dopants in semiconductors are activated into electrically active substitutional lattice sites by high-temperature annealing. Annealing also removes most of the implantation damage. During the anneal, however, the defect supersaturation produced by the implant interacts with the dopants and produces a diffusion transient that results in long-range transport of dopant away from the active region. This phenomenon is similar to the segregation effects in Ni–Si just described. Although this effect, called transient-enhanced diffusion (TED), was recognized over 20 years ago, it has become of concern only recently as features in devices approach the scale of 100 nm.

---

[173] R. S. Averback, L. E. Rehn, W. Wagner, P. R. Okamoto, and H. Wiedersich, *Nucl. Instrum. Method B* **194**, 457 (1982).

[174] A. Iwase, L. E. Rehn, P. M. Baldo, and L. Funk, *Appl. Phys. Lett.* **67**, 229 (1995).

[175] A. Müller, V. Naundorf, and M. P. Macht, *J. Nucl. Mater.* **155–157**, 1128, (1988).

[176] V. Naundorf, *Int. J. Mod. Phys. B* **6**, 2925 (1992).

[177] P. Fielitz, M.-P. Macht, V. Naundorf, and H. Wollenberger, *Appl. Phys. Lett.* **69**, 331 (1996).

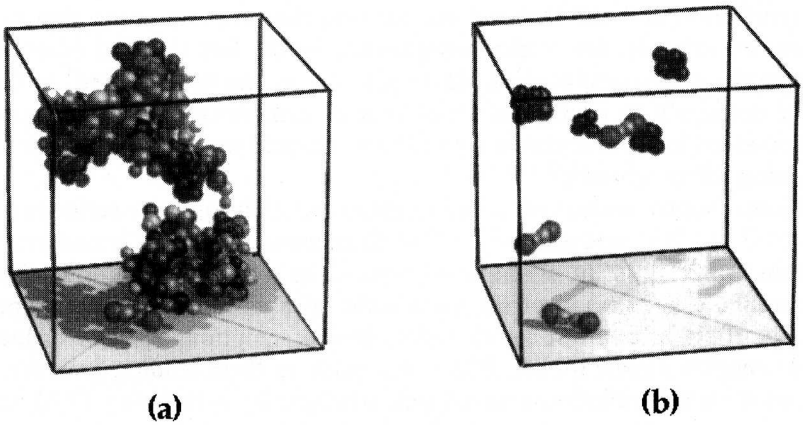

FIG. 57. Annealing of an amorphous pocket induced by a 5-keV cascade in Si. After 1 ns the amorphous material has recrystallized. The gray scale represents atomic-level stress. Two new self-interstitials, a monovacancy, two divacancies, and a trivacancy have resulted from the recrystallization process. (After Ref. 124.)

The magnitude of the TED effect for a given set of implant conditions depends on the fraction of freely migrating defects during the anneal. Under an appropriate set of irradiation conditions, the silicon interstitials responsible for TED of B in Si first form rodlike {311} defects and subsequently are dissociated from these defects to cause TED.[178,179] At low damage levels, $<1 \times 10^{11}$ ions/cm^2, interstitials escape from the displacement cascade without the intermediate step of forming {311} defects.[178] Eaglesham *et al.* showed that the diffusion transient and the dissolution of the {311} defects have comparable time constants and activation energies: moreover, they found that the number of interstitials stored in the {311} defects corresponded approximately to one per implanted ion.[180] This so-called "+1" model implies that all defects produced by the implantation recombine in the bulk or at the surface and only the extra interstitial introduced by the implanted atom survives to cause long-range diffusion. This rather astonishing result can be understood, however, on rather simple terms from the simulations. As shown in Fig. 40, amorphous pockets are produced by ion irradiation of Si, but interstitial atoms and vacancies are

[178] H. G. A. Huizing, C. C. G. Visser, N. E. B. Cowern, P. A. Stolk, and R. C. M. de Kruif, *Appl. Phys. Lett.* **69**, 1211 (1996).
[179] P. A. Stolk, H.-J. Gossman, D. J. Eaglesham, and J. M. Poate, *Nucl. Instrum. Methods B* **96**, 187 (1995).
[180] D. J. Eaglesham, P. A. Stolk, H.-J. Gossman, and J. M. Poate, *Appl. Phys. Lett.* **65**, 2305 (1994).

not well separated. Thus, during the regrowth of the amorphous zones during annealing, nearly complete recovery is obtained. This result is illustrated in Fig. 57, where the annealing of an amorphous pocket produced by a 5-keV cascade in Si is illustrated. After MD annealing for 1 ns at 1300 K, the amorphous material has recrystallized and only a few self-interstitials, a vacancy, and three small vacancy clusters are left behind.

X. Conclusions

Displacement processes in irradiated solids are now understood in rather good detail in most simple metals and some semiconductors. It is recognized that displacements in energetic cascades are part of a complex dynamics which involves both energetic recoils, which are characterized by binary collisions, and intense local heating. Which processes dominates depend on the atomic mass and elastic properties of the materials, the bombardment conditions, and the property of interest, that is, defect production, atomic mixing, stress relaxation, etc. Thus different materials can respond to irradiation in very different ways. It was demonstrated, for example, that because nearly defect-free crystalline metals can grow from a melt at speeds approaching the speed of sound, while covalently bonded materials can only grow much slower, the radiation-induced defect structures in these materials are vastly different.

Much of the detailed information on displacement processes that has been gained recently has derived from molecular dynamics computer simulations. Presently, this method provides the only theoretical means to treat the inhomogeneous, many-body aspects of cascade dynamics. With the enormous improvements in computer capabilities, and the development of realistic yet economical potentials that have occurred over the past years, this rather brute force approach has become a practical solution as well. One of the reasons for the success of MD is that in simple metals many radiation effects are robust and do not depend sensitively to the details of the interatomic potentials. Substantial improvements in the potentials and methods, however, are still needed before these simulations can attempt to examine with reliability more complex materials, such as ionic crystals, compound semiconductors, and intermetallic alloys. In these materials electronic processes become far more important and these have been largely ignored, to date. Extending the simulations to longer times, moreover, from nanoseconds to microseconds, will also require new developments.

The trend toward increasing reliance on computer simulations in the research of radiation effects appears almost certain to continue. Most simulations in the past, however, have not been carefully scrutinized by critical

experimental evaluation. Usually, only qualitative comparisons between simulation and experiments have been possible. The more demanding requirements on future simulations, however, will necessitate closer validation. A new series of experiments, therefore, specifically designed to test predictions of computer simulations, are becoming of great importance. Thus, many experimental and theoretical challenges lie ahead before our understanding of displacement damage can be extended to systems and time scales of technological significance.

Acknowledgements

The authors are grateful to many of their colleagues and students at Argonne National Laboratory and the University of Illinois for their contributions to the work presented here. We are particularly grateful to Drs. Peter Ehrhart, Mark Kirk, Mai Ghaly and Kai Nordlund for many helpful discussions during the preparation of this manuscript and to Mr. P. Partyka for critically reading it. Finally, we wish to acknowledge the U.S. Department of Energy, Basic Energy Sciences, for their continued support of this work.